Modelling the Impacts of Space Weather on UK Railway Signalling Systems

Cameron James Patterson, MSci Hons

Department of Physics

Faculty of Science and Technology

Lancaster University

A thesis submitted for the degree of

Doctor of Philosophy

April, 2024

Modelling the Impacts of Space Weather on UK Railway Signalling Systems

Cameron James Patterson, MSci Hons.

Abstract

This thesis presents an investigation to model geomagnetic effects on DC track circuit signalling for AC-electrified railways in the UK, using the Glasgow to Edinburgh via Falkirk line and the Preston to Lancaster section of the West Coast Main Line as examples. In Chapter 4, the electric field strengths needed to cause "right side" failures, where green signals for blocks that are unoccupied by trains are turned red, are examined. It is suggested that the threshold is equivalent to an electric field generated by a storm that occurs approximately once every 30 years. Chapter 5 expands this work to "wrong side" failures, where the red signals for blocks that contain trains are turned green, a potentially more hazardous misoperation mode. It is shown that the position of the train along the block or, more precisely, the distance between the rearmost axle and the relay, has a large impact on how susceptible the relay is to geomagnetic disturbances. Assuming each train is near the end of the block it is occupying in the modelling, the electric field strength needed to cause "wrong side" failures is lower than that for "right side" failures, equivalent to the electric field generated by a storm occurring approximately once every 10 to 20 years. In Chapter 6, time-varying electric fields from the March 1989 and October 2003 storms are applied to both routes, as well as 1-in-100 year and 1-in-200 year extreme storm proxies, obtained by scaling the March 1989 storm by 2 and 4 times respectively. For the historic storms, it is shown that there was the potential for a small number of "wrong side" failures, but no "right side" failures to occur. For the extreme storm estimates, it is suggested that a large number of misoperations of both types could occur across each route.

Acknowledgements

I thank the Science and Technology Facilities Council and the Lancaster University Faculty of Science and Technology for my studentship, without which I would not have been able to undertake this PhD.

My sincerest gratitude goes to my supervisor, Professor Jim Wild, who has gone above and beyond to provide me with guidance, wisdom (often via the medium of Futurama and Star Wars memes), and opportunities to enhance my PhD experience and prepare me for the future. Thanks to Dr Adrian Grocott and Dr Jonathan Prance for their support during my studies. I had the pleasure of working with Dr David Boteler of Natural Resources Canada, and through his comprehensive feedback, I learned a lot about how to write a good paper. I am thankful for the opportunity to have collaborated with Ciarán Beggan and Gemma Richardson of the British Geological Survey and look forward to working together in the future. Special thanks go to the Lancaster University Global Advancement Fund, the Physics department, and the Royal Astronomical Society, who all provided financial support for my epic train journey across Canada and the USA to attend the 2023 AGU Fall Meeting in San Francisco.

I would also like to make some personal thanks. To Mum and Dad for their never-ending support, regardless of the many life paths I have pursued. To Grandma, 100 years young and still wanting to keep up with everything I do. To Rach and Mike for their advice and encouragement. To my Dungeons and Dragons group, for the welcome distraction at the end of a long week, and especially to Ash for the many road trips to Lancaster to help with one thing or another. And to my friends in the Lancaster University Space and Planetary Physics Group for the many enjoyable quiz and game nights.

Finally, completing my PhD would not have been possible without the support of my fiancé, Evelina. You celebrated with me on the good days and raised my spirits on the bad days. It has been an amazing and, at times, difficult journey, but I can't think of anyone I would rather have had by my side. Jag älskar dig.

Declaration

I declare that the work presented in this thesis is, to the best of my knowledge and belief, original and my own work. The material has not been submitted, either in whole or in part, for a degree at this, or any other university. This thesis does not exceed the maximum permitted word length of 80,000 words including appendices and footnotes, but excluding the bibliography. A rough estimate of the word count is: 33984

Cameron James Patterson

Publications

The following publications have been created directly from the thesis, from which large portions of these published works are used within chapter 3, chapter 4, and chapter 5:

Patterson, C. J., Wild, J. A., & Boteler, D. H. (2023a). Modeling the impact of geomagnetically induced currents on electrified railway signaling systems in the United Kingdom. *Space Weather*, *21*(3), e2022SW003385. https://doi.org/10.1029/2022SW003385

Patterson, C. J., Wild, J. A., & Boteler, D. H. (2023b). Modeling "wrong side" failures caused by geomagnetically induced currents in electrified railway signaling systems in the UK. *Space Weather*, *21*(12), e2023SW003625. https://doi.org/10.1029/2023SW003625

Patterson, C. J., Wild, J. A., Beggan, C. D., Richardson, G. S., & Boteler, D. H. (2024). Modelling electrified railway signalling misoperations during extreme space weather events in the UK. *Scientific Reports*, *14*(1583). https://doi.org/10.1038/s41598-024-51390-3

Contents

List of Tables

List of Figures

Abbreviations

AC Alternating Current

AE Auroral Electrojet

AFTC Audio Frequency Track Circuit

AT Auto Transformer

ATF Auto Transformer Feeder

BT Booster Transformer

CIR Co-rotating Interaction Region

CME Coronal Mass Ejection

DC Direct Current

DNO Distribution Network Operator

Dst Disturbed Storm Time

DSTL Distributed Source Transmission Line

GIC Geomagnetically Induced Current

HF High Frequency

IMF Interplanetary Magnetic Field

IRJ Insulated Rail Joint

KCL Kirchhoff's Current Law

KVL Kirchhoff's Voltage Law

MT Magnetotelluric

OL Ohm's Law

OLE Overhead Line Equipment

RC Return Conductor

SECS Spherical Elementary Current Systems

SID Sudden Ionospheric Disturbances

SIR Stream Interaction Region

SSC Sudden Storm Commencement

UT Universal Time

WCML West Coast Main Line

Chapter 1

Introduction

"The telegraph lines had other messages to carry more urgent than those of men." Maunder (1897a)

1.1 What is Space Weather?

The COVID-19 pandemic that dominated the first two years of my PhD is a prime example of a rare yet heavily disruptive event, one that showed just how complex a situation can become when the systems that we rely upon in our daily lives are so interdependent. Space weather refers to the conditions in the Sun-Earth environment that can interfere with or damage space- and ground-based technology and can endanger human life or health, and in the 2023 UK National Risk Register of Civil Emergencies, 'severe space weather' is in the same category of likelihood and just one category of impact lower than 'pandemic' (Cabinet Office, 2023).

The origin of space weather is the Sun, where occasional surface eruptions propel large clouds of magnetised plasma and/or streams of high energy particles into interplanetary space. When these eruptions occur in an earthward direction, they can impact satellite and spacecraft operations, increase radiation exposure for astronauts and aircraft pilots, crew and passengers, and cause communications blackouts. Their effects can even reach down to the ground, driving currents through

conductive infrastructures such as power grids, oil and gas pipelines, and railways.

Tackling any of these impacts singularly is already a daunting task, but in the event of severe space weather, it is possible that all of these issues could occur simultaneously, leading to widespread disruption.

1.2 Space Weather and Railways

Some of the earliest records of space weather impacts on technology were regarding issues with telegraph systems. In the 1800s, telegraph lines were used on railways to alert signal boxes when trains had vacated sections of signalled track so they could change the semaphore signals - mechanical arms that tilt up and down to notify drivers of upcoming line conditions. On the evening of the 19th March, 1847, "brilliant aurora" were seen over the UK, and at the same time strong alternating deflections were being observed in the needles of the electric telegraph of the Midland Railway, with similar effects on the telegraphs of other railway lines also reported (Barlow, 1849). At the time, these deflection were assumed to be caused by "atmospheric electricity passing by the wire thorough the coil to the earth, or vice versa from the earth to the atmosphere".

It was suggested by Cade III (2013) that an observation recorded in the journal *Nature* documented an even earlier impact of space weather on railway signalling in 1841, with the article in question stating "On the 18th of October, 1841, a very intense magnetic disturbance was recorded, and amongst other curious facts mentioned is that of the detention of the 10.5 P.M. express train at Exeter (for) sixteen minutes, as from the magnetic disturbance it was impossible to ascertain if the line was clear at Starcross. The superintendent at Exeter reported the next morning that someone was playing tricks with the instruments, and would not let them work" (Nature, 1871). However, the railway line to Exeter via Starcross did not open until 1846 (MacDermot and Clinker, 1972), so while this is an interesting occurrence, the date recorded in the *Nature* article is likely a typographical error.

Another documented event of space weather impacting railways was observed in 1882, where it was recorded that "The needles in the telegraph instruments twitched to and fro. The signal bells on many of the railway lines were rung, and some of the operators received shocks from their instruments" (Maunder, 1897b).

Until this point, the impacts discussed have all been related to telegraph systems, which are a secondary impact to railway signalling systems. However, with the move to DC track circuits, space weather was able to impact railway signalling more directly. One such event occurred in Sweden during a geomagnetic storm in July 1982 where geomagnetically induced currents caused signals to switch to red, back to green, and then to red again without any trains occupying the sections (Wik et al., 2009). This was a well-known issue in Sweden, with the Swedish Transportation Board listing geomagnetic interference as a potential source for signalling misoperations (Thelander et al., 1956), and research was undertaken at the time to analyse these effects and suggest mitigation strategies (Alm, 2020; Lejdström and Svensson, 2020).

In the late 2000s, a number of studies in Russia found a high correlation between increases in total daily duration of malfunctions and breakdowns across 2004 and geomagnetic activity in that same time period (Kasinskii et al., 2007; Ptitsyna et al., 2008), with an increase in total daily duration of up to three times during the peak of a geomagnetic storm. Expanding this work to analyse the largest storms of 2000-2005 and the March 1989 storm, it was shown that some of the faults that occurred during periods of heightened geomagnetic activity were false blockages similar to those observed in Sweden in 1982 (Eroshenko et al., 2010).

Severe space weather was added to the UK National Risk Register of Civil Emergencies in 2012 (Cabinet Office, 2012). The UK Government's Department for Transport subsequently commissioned a report on rail resilience to space weather with the aim of further understanding the threat that space weather posed to UK railway infrastructure (Darch et al., 2014). This report highlighted the knowledge gaps when it came to track circuit interference, finding that "Signalling assets such as

signalling and track circuits are potentially vulnerable to CMEs, and many assets are potentially vulnerable to Single Event Effects" (p. 20). It also identified signalling systems as a potential area of vulnerability, stating "The relative vulnerability of different types of systems (e.g. track-based train detection) is not clear at this stage" (p. 20). In 2015, the "Space Weather and Rail" workshop jointly organised by the European Commission's Joint Research Centre, the Swedish Civil Contingencies Agency, the UK Department for Transport and the US National Oceanic and Atmospheric Administration worked towards furthering understanding of space weather's impacts on railways and raising awareness among operators (Krausmann et al., 2015).

In 2016, geomagnetically induced currents were observed flowing through track circuits at the site of the Hebi East traction power supply station along the Beijing to Hong Kong high-speed passenger line, with a maximum current level of 1.74A (Liu et al., 2016).

Using the well-established method of distributed source transmission line theory (Schelkunoff, 1938), previously used for modelling geomagnetic interference on oil and gas pipelines (Boteler, 2013; Boteler, 1997) and rails (Alm, 2020; Lejdström and Svensson, 2020), a new method for modelling geomagnetic interference on DC track circuits was published in 2021 (Boteler, 2021). This new method used the transmission line model to build equivalent pi-circuits for individual sections of rail, which could then be combined with the track circuit components to form a nodal admittance network of track circuits in their entirety and includes the equivalent current sources from the geomagnetically induced electric field. Provided values for the electrical characteristics of the rails and parameters of the track circuit equipment are available, models of railway lines can be constructed using this method and used to analyse the impacts on track circuits from geomagnetic interference.

1.3 Thesis Motivation and Aims

Given that signalling misoperations have been observed in a number of countries, the motivation behind this thesis is to determine whether lines of the UK railway network could be susceptible to similar impacts. Using the methodology set out by Boteler (2021), and by using UK-specific parameters gathered from Network Rail standards documents, a model is developed to analyse the impacts of space weather on DC track circuits along a number of AC electrified railway lines in the UK.

The main aims are as follows. First, to find the magnitude of electric field needed to cause different types of misoperations to occur, which can then be used to estimate the return period of geomagnetic storms that could potentially have an impact on the signalling systems of these lines. Second, to model how these threshold electric field values change when different parameters are used in the model, e.g., to simulate changes due to different weather conditions. And third, to run the model with geoelectric field estimates for the largest storms of the past few decades, to analyse whether the model suggests any misoperations would have occurred.

Chapter 2

The Drivers of Space Weather

2.1 The Sun

The Sun is driven by nuclear fusion within its core, emitting approximately 4×10^{26} J of energy every second. This energy is transported to the surface through the radiative zone primarily by electromagnetic photons and then through the convection zone by the bulk fluid motion of solar material, where it can radiate out into space. The matter in the convection zone is hot (around 2×10^6 K at the base and cooling to 5800 K at the surface) and ionised, so the convection motion of this electrically conducting matter gives rise to magnetic fields as per dynamo theory. The Sun is not a rigid body, and exhibits differential rotational velocities at different latitudes. This means that as these magnetic fields rise to the surface, they become twisted into complex configurations, often leading to rapid energy release. To understand this energy release, we must consider some generic aspects of plasma physics.

Ohm's law for a conductive fluid, such as a plasma, is given as

$$\sigma(\mathbf{E} + \mathbf{v} \times \mathbf{B}) = \mathbf{J} \tag{2.1}$$

where the plasma with electrical conductivity σ is moving with velocity $\mathbf{v}$ in a magnetic field $\mathbf{B}$ which induces an electric field $\mathbf{E}$ that exerts an electric force on

the ions and electrons giving rise to an electric current with current density $\mathbf{J}$.

In a steady state, $\mathbf{E}$ is equal to $-\mathbf{v} \times \mathbf{B}$, meaning the net value of $\mathbf{J}$ is zero. However, in unstable states, such as discontinuities between magnetic field structures, $\mathbf{J}$ is non-zero, and these are the regions where magnetic reconnection can occur. This is detailed below.

Combining equation 2.1 with the Maxwell-Faraday equation

$$\nabla \times \mathbf{E} = -\frac{\partial \mathbf{B}}{\partial t} \tag{2.2}$$

where $\nabla\times$ is the curl operator, and the Ampère-Maxwell equation

$$\nabla \times \mathbf{B} = \mu_0 \mathbf{J} \tag{2.3}$$

where μ_0 is the vacuum magnetic permeability and the term for the displacement current is not included as the current carried by the free charges is so much greater, then substituting in the expression for Gauss's law for magnetism $\nabla \cdot \mathbf{B} = 0$, we get the induction equation for an electrically resistive fluid

$$\frac{\partial B}{\partial t} = \eta \nabla^2 \mathbf{B} + \nabla \times (\mathbf{v} \times \mathbf{B}) \tag{2.4}$$

where $\eta = \frac{1}{\mu_0 \sigma}$ is the magnetic diffusivity.

Therefore, for a plasma of scale length L such that $\nabla \sim \frac{1}{L}$ and scale speed V such that $\mathbf{v} \sim V$ would have relationships

$$\nabla \times (\mathbf{v} \times \mathbf{B}) \sim \frac{VB}{L} \tag{2.5}$$

for the magnetic induction, and

$$\eta \nabla^2 \mathbf{B} \sim \frac{\eta B}{L^2} \tag{2.6}$$

for the magnetic diffusion.

The ratio of these quantities is known as the magnetic Reynolds number R_m, where

$$R_m = \frac{LV}{\eta} \tag{2.7}$$

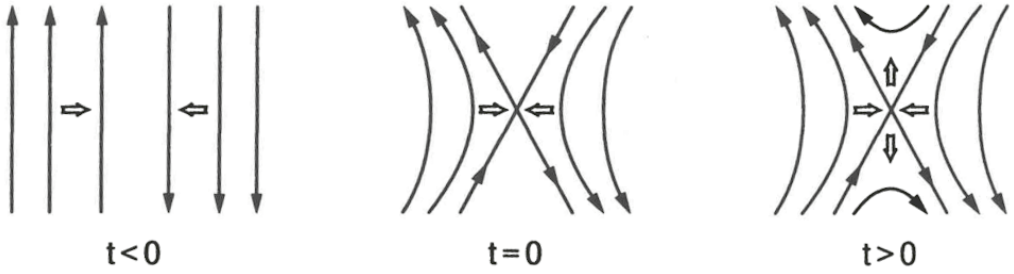

Figure 2.1: Schematic of field line reconfiguration during magnetic reconnection in 2D. (Credit: Baumjohann and Treumann, 1996)

which describes the relative effects of magnetic induction by the motion of the plasma to the magnetic diffusion.

Beyond the surface of the Sun, the plasma is largely collisionless and thus highly conducting. In this case, $\eta \to 0$ (a very large magnetic Reynolds number), meaning equation 2.4 can be simplified by removing the term relating to magnetic diffusion, giving

$$\frac{\partial B}{\partial t} = \nabla \times (\mathbf{v} \times \mathbf{B}) \tag{2.8}$$

Equation 2.8 implies that the plasma and the embedded magnetic fields are constrained to move together, this is referred to as Alfvén's theorem (Alfvén, 1942) or frozen-in flux theorem.

Where two volumes of magnetised plasma with opposing magnetic fields come into contact, due to Ampère's circuital law, a current sheet is formed between both fields and the $\mathbf{J} \times \mathbf{B}$ force pushes plasma from both sides together. As $\mathbf{B}$ is frozen-in, the field lines are also pushed together, which leads to regions of small width that experience large magnetic field gradient where the magnetic Reynolds number can become small enough such that the diffusion term in equation 2.4 dominates. The frozen-in flux theorem breaks down, and the topology and connectedness of the field lines are reconfigured in a process known as magnetic reconnection, shown in Figure 2.1.

We can now apply these ideas to the aforementioned twisted magnetic fields.

They confine pockets of hot dense plasma, and when magnetic reconnection occurs, they can eject clouds of plasma into interplanetary space in what is known as a coronal mass ejection (CME). The energy released by magnetic reconnection can also give rise to high-energy electrons that can collide with other matter and create pulses of electromagnetic radiation called solar flares. While the mechanisms that generate these phenomena are similar, they can occur simultaneously or independently.

When observing the visible surface of the Sun, known as the photosphere, dark spots can be seen. These are sunspots, regions of intensified magnetic field directed into or out of the surface the solar surface that disrupt convection, making them cooler and darker than their surroundings. The spots have a singular polarity and are connected to a spot of opposite polarity elsewhere on the surface. These sunspot pairs and their associated magnetic fields are a source for the previously discussed phenomena, with the regions of activity termed "active regions". The number of sunspots varies over an 11-year cycle, and the activity of the sun also waxes and wanes correspondingly. Since the magnetic field of the Sun also reverses every solar cycle around the period of maximum activity, the polarity of the sunspots also reverses, meaning that the magnetic cycle of sunspots is about 22 years, known as a Hale cycle (Hale and Nicholson, 1925). Sunspots and active regions are especially important when considering the impacts of space weather, as statistically more CMEs and solar flares can occur during solar cycle maxima, though not necessarily in an earthward direction.

2.2 The Solar Wind and Earth's Magnetosphere

2.2.1 The Solar Wind

The corona is the outermost region of the Sun's atmosphere. This region is heated by the release of magnetic energy to approximately 10^6 K, compared to around 5800 K at the solar surface. At such high temperatures, coronal material is able to escape the Sun's gravitational pull and blast out into interplanetary space, forming the

solar wind, which expands and defines a region surrounding the Sun known as the heliosphere.

Going back to the frozen-in flux theorem, we know that the Sun's magnetic field must also be carried into interplanetary space with the solar wind, and this magnetic field is known as the interplanetary magnetic field (IMF). The IMF has a characteristic spiral pattern when viewed from above the solar poles, formed as the solar wind travels radially away from the surface of the Sun, but as the origin point continues to rotate along with the surface of the sun, shown in Figure 2.2. This pattern is widely termed the Parker spiral (Parker, 1958). However, as different latitudes of the solar surface rotate with different speeds, in reality the shape of the IMF is not this simple, and in fact produces a wave like pattern which from Earth looks like the solar wind is alternating between the sides of the Sun's magnetic equator.

It is also important to note that at the equatorial regions of the Sun, the magnetic field structures inhibit the speed of the solar wind. This is not the case at the solar poles, or at outflowing coronal holes, where solar wind speeds are higher. If the solar wind speeds differ, so does the angle of the spiralling. When regions of different speeds interact, the solar wind can become compressed (Belcher and Davis Jr., 1971), forming a stream interaction region (SIR). As coronal holes tend to persist for long periods of time, SIRs are often observed over multiple solar rotation periods ($\sim$27 days at Earth). A persisting SIR is termed a co-rotating interaction region (CIR). Due to their increased plasma density and magnetic field strength, CIRs can influence the solar wind that reaches Earth and affect the propagation of CMEs. CIRs can also be geoeffective, causing geomagnetic storms.

2.2.2 The Magnetosphere

The Earth's magnetic field has an approximately dipolar configuration, which can be thought of as similar in shape to that of a bar magnet. Its current configuration means that the magnetic north pole is in the geographic southern hemisphere and

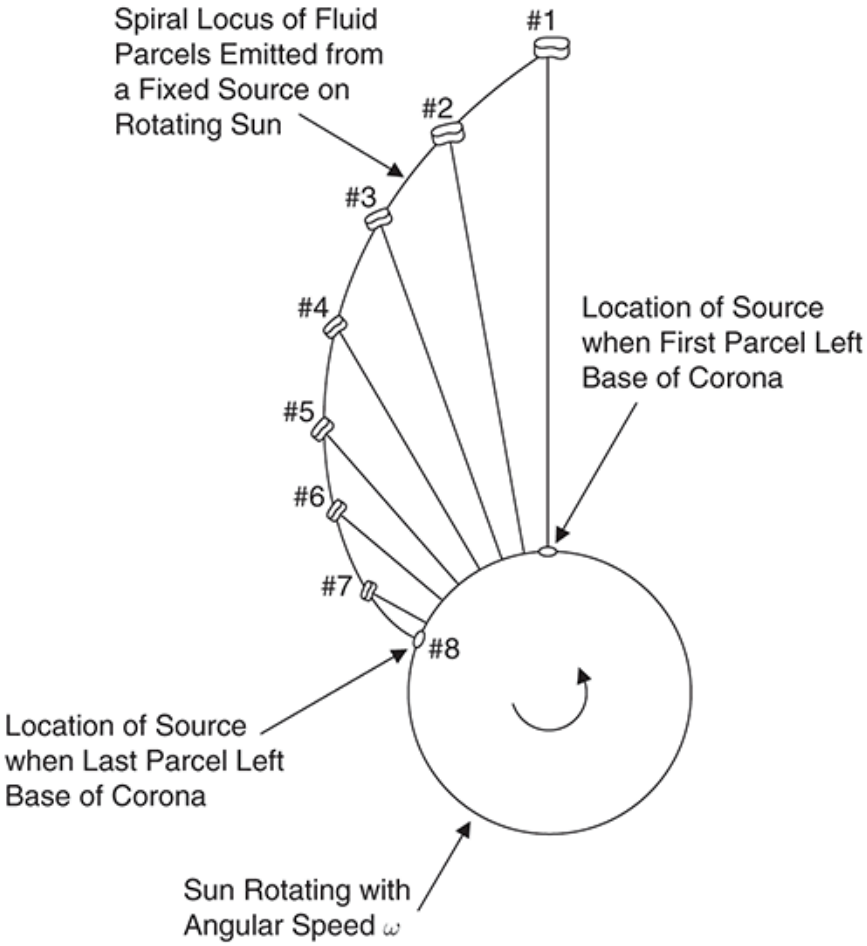

Figure 2.2: Schematic showing how the interplanetary magnetic field forms a spiral pattern when viewed from above or below the equatorial plane due to the radial emission of the solar wind and the rotation of the Sun. (Credit: Kivelson and Russell, 1995)

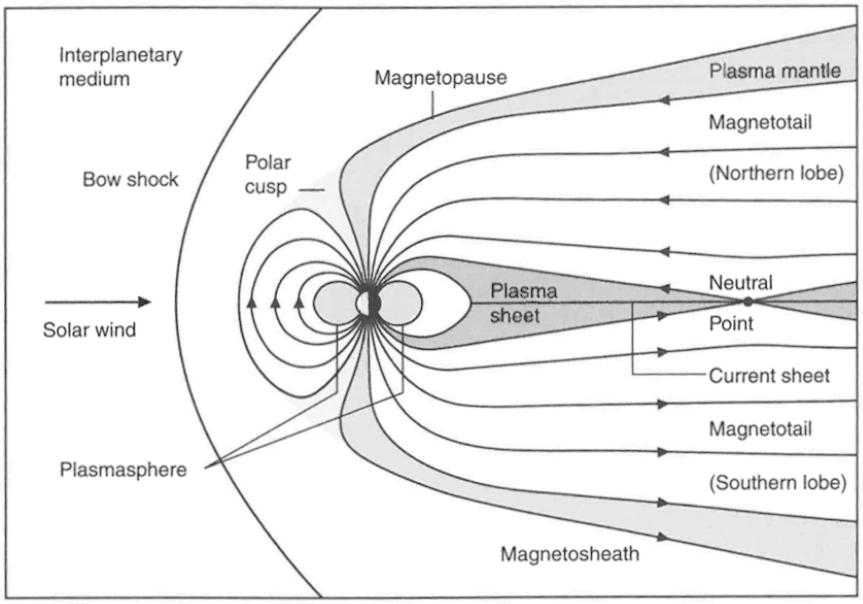

Figure 2.3: 2D representation of the magnetosphere noon-midnight cross-section. The dipole shape of the Earth's magnetic field can be clearly seen on the dayside, with the nightside being dragged into a tail-like structure. (Credit: Russell et al., 2016)

the magnetic south pole is in the geographic northern hemisphere. The magnetic field is also not aligned with the Earth's rotational axis, exhibiting an approximately 11 degrees tilt at present. When the solar wind reaches the Earth, it is deflected by this magnetic field, compressing it on the dayside (the side facing towards the Sun) and dragging it out into a long tail-like structure on the nightside (the side facing away from the Sun), forming a cavity known as the magnetosphere, as shown in Figure 2.3. As the solar wind is supersonic, a shock wave is formed on/upstream from the dayside of the magnetosphere called the bow shock. The bow shock slows the solar wind and redirects it around the magnetosphere, with the area between the bow shock and the magnetosphere called the magnetosheath. The boundary of the magnetosphere is called the magnetopause, and its position depends on the pressure of the solar wind, which is related to the solar wind velocity and density. When the solar wind pressure increases, the magnetopause moves earthwards, when the solar wins pressure decreases, the magnetosphere expands.

In the inner magnetosphere, plasma predominantly originating from the Earth is trapped on closed magnetic field lines, forming a region of cold, dense plasma, mostly consisting of hydrogen, helium and some oxygen, that co-rotates with the planet. This region is called the plasmasphere, which has a well-defined boundary beyond which plasma density rapidly drops known as the plasmapause. There are also high-energy particles magnetically trapped within the magnetosphere, which form the two Van Allen radiation belts (with particle energies extending into the relativistic region) and the ring current (with peak particle energies around 200 keV). Henceforth, "ring current" refers to the westward ring current, in contrast to the eastward inner ring current formed at the earthward edge of the plasma sheet as a result of the negative plasma pressure gradient in the region inside the pressure maximum (Ganushkina et al., 2018; Le et al., 2004). The ring current is formed when the Earth's dipole field causes the positively charged ions to drift westward and the negatively charged electrons to drift in the opposite direction. This sets up an westward directed electric current that encircles the Earth, which in turn generates a magnetic field surrounding it, as per Ampére's circuital law. The direction of the magnetic field can be determined using the right-hand rule: on the right hand, if the thumb is pointing in the direction of the flow of current, the fingers will curl in the direction of the magnetic field around the wire. So for the case of the ring current, the magnetic field generated at the Earth's surface by the ring current opposes the magnetic field of the Earth. The Disturbed Storm Time (Dst) index (Sugiura, 1964) is a magnetic index that measures the deviation of the Earth's magnetic field from the quiet time level, so a negative Dst indicates an enhancement of the ring current. This effect is observes at low latitudes, away from the magnetic equator, and is observed in the horizontal component of the magnetic field. Connecting the ring current and the magnetopause to the ionosphere at higher latitudes are the field-aligned currents, also known as Birkeland currents, which play a major role in space weather by coupling the magnetosphere to Earth's upper atmosphere. These currents are illustrated in Figure 2.4, and discussed in more detail in Section 2.3.3.

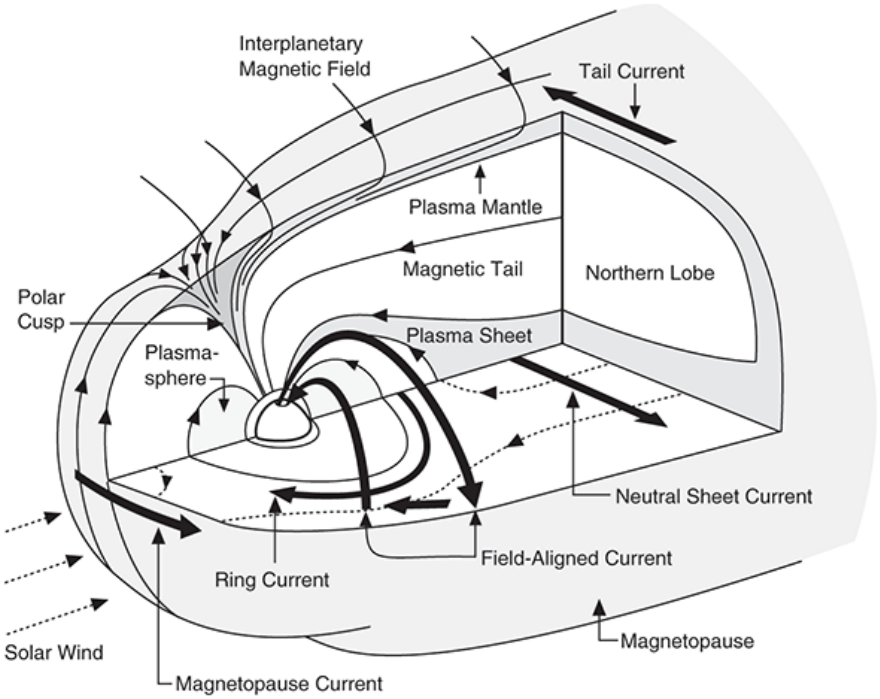

Figure 2.4: 3D representation of the magnetosphere showing the various current systems flowing in the magnetosphere. (Credit: Moldwin, 2022)

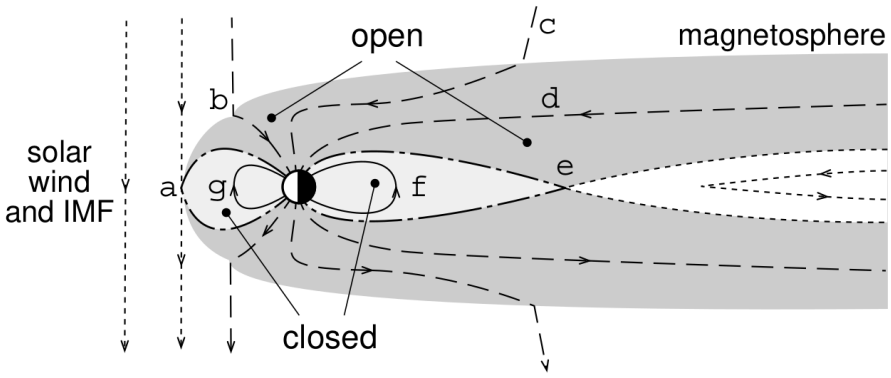

Figure 2.5: Illustration of the Dungey cycle. Magnetic reconnection occurs at point (a), where the previously closed field lines of the Earth become open, with one end connected to the solar wind. The solar wind end moves downwind, dragging the field line to (b), (c), (d), and eventually (e) where magnetic reconnection occurs once again, closing the field lines (f). (Credit: Milan et al., 2003)

When the solar wind interacts with the magnetosphere, if the magnetic field orientations are opposed, magnetic reconnection can occur. In the case of the Earth, this occurs when there is a southwards component of the IMF to interact with the northwards component of the Earth's magnetic field. Applying what was shown in Figure 2.1 to the Earth, field lines where both ends connected to the Earth (closed) are now connected on one end to the solar wind (open), allowing solar wind plasma and its associated momentum and energy to enter the magnetosphere. Since the solar wind ends of these field lines are travelling away from the Earth, they effectively get dragged into a long, cylindrical structure known as the magnetotail. This process builds up magnetic energy in the tail, where it can also undergo magnetic reconnection, where the field lines become closed once again. The closed field lines are then carried back to Earth by a process known as convection, which is due to a dawn to dusk electric field in the tail plasma sheet imparted by the solar wind. This cycle is known as the Dungey cycle (Dungey, 1961), illustrated in Figure 2.5.

2.3 Earth's Upper Atmosphere

2.3.1 The Thermosphere

The thermosphere is a region of the upper atmosphere extending from an altitude of approximately 100 km above the surface up to 1000 km that contains mostly neutral atoms and molecules. The temperature of the thermosphere is highly variable, with the foremost source of heating being the absorption of solar electromagnetic radiation (mostly UV and X-rays) by neutral atoms and auroral electron precipitation. Since the major sources of UV and X-rays from the Sun are solar flares and active regions, there is a distinct variation in thermospheric temperature over the 11-year solar cycle. Other sources of ionisation/heating are collisions with energetic particles, such as cosmic rays and solar wind particles; Joule heating, where the current carrying particles in ionospheric current systems collide with neutral particles; and gravity waves, where waves generatated in the lower atmosphere (potentially from convective thunderstorms) can break in the thermosphere, transferring large amounts of energy (Moldwin, 2022).

2.3.2 The Ionosphere

The ionisation of the upper atmosphere is primarily a result of high-energy photons from the Sun (UV and X-rays) colliding with neutral atoms and causing an electron to become freed, increasing the surrounding electron density. This process is termed photoionisation, and leads to the formation of the ionosphere.

The ionosphere and the thermosphere overlap, but since one body is ionised and the other neutral, it may seem logical to consider them independently. However, they are coupled due to neutral particle-ion interactions (collisions), effects which should not be ignored. Since the Sun is the primary source of ionisation, the peak ionosphere densities occur on the dayside, however, since the recombination time of ions and electrons is similar to the Earth's rotational period, the density of the nightside ionosphere is usually reduced but not zero. Recombination rate is also

dependent on density, with slower recombination at higher altitudes and vice versa. Long recombination times of hours are applicable only in the F region ionosphere, with recombination times in the lower altitude D and E regions much shorter. It is this complex balance of ionisation and recombination that dictates ionospheric density. The combination of photons with differing energies being able to penetrate different distances into the Earth's atmosphere and the varying densities of neutral particles leads to the formation of multiple ionospheric layers.

The layer at the lowest altitude is the D region, extending from around 50 to 90 km (down into the mesosphere, the region below the thermosphere). D region ionisation is primarily due to solar UV photons ionising nitric oxide (NO) molecules, however there is also ionisation of molecular nitrogen (N_2) and oxygen (O_2) by solar X-rays and cosmic rays. As the density of neutrals in the D region is high, the recombination rate is also high, meaning this region mostly disappears during the night and it is has the lowest ionisation out of all ionospheric regions. The D region has a large impact on high frequency (HF) radio communications due to its ability to absorb radio waves, leading to HF radio communication disruptions. Sudden ionospheric disturbances (SID) brought on by increased X-rays from solar storms and solar energetic particle (SEP) precipitation can cause such large increases to D region ionisation, that HF radio communications can become completely blacked out.

Between 90 to 120 km altitude is the E region, formed by UV and low-energy X-ray ionisation of O_2. At this altitude, the recombination rate is lower than for the D region, allowing the peak density of the E region to reach over 100 times that of the D region. However, similar to the D region, the E region also largely dissipates at night. Due to its altitude, E region ionisation can also occur due to energetic particle precipitation. This form of ionisation can contribute significantly to E region ionisation, especially at night when there is no ionisation from solar photons.

Within the E region also exist narrow regions of short-lived high level ionisation

called Sporadic E. These can occur due to many different sources, including neutral atmosphere dynamics and the oblation of meteors entering the Earth's atmosphere. Sporadic E can also cause HF radio communication disruptions, and can be difficult to predict owing to the varied and complex origins.

Finally, we have the F region, which extends from approximately 120 km upwards, peaking at around 300 km. The region above the peak is termed the topside ionosphere and its density drops off almost exponentially with height, merging with the plasmasphere. The boundary between the topside ionosphere and the plasmasphere (at around 1000 km) is defined as the point at which the dominant ion changes from oxygen (in the ionosphere) to hydrogen (in the plasmasphere). The F region is largely formed due to the ionisation of atomic oxygen (O) by extreme UV solar radiation. Since photoionisation is greater at higher altitudes, during the day, the F layer is separated into two distinct layers, F1 and F2, with the higher altitude F2 layer having a larger density. Due to the higher altitude and hence lower recombination rate, as well as the population of atomic ions, which have a much lower recombination rate than molecular ions, the F region decreases at night, but reduces at a much slower rate than the D and E regions.

2.3.3 Ionospheric Convection

During the Dungey cycle, as the solar wind ends of the field lines are dragged downstream, the ionospheric footprint of the field lines and the frozen-in plasma is also moved across the polar cap to the nightside. After magnetic reconnection occurs in the tail, the movement of the field lines back towards the sun also moves the footprint of the field lines and plasma sunward in the dawn- and dusk side of the ionosphere, within the auroral oval. This forms a two-cell convection pattern in the polar regions of the ionosphere, shown in Figure 2.6.

The convection pattern is equivalent to an electric potential pattern, since plasma flow in the presence of a magnetic field produces an electric field perpendicular to the flow. The $\mathbf{E} \times \mathbf{B}$ trajectories of the plasma define equipotential boundaries, hence

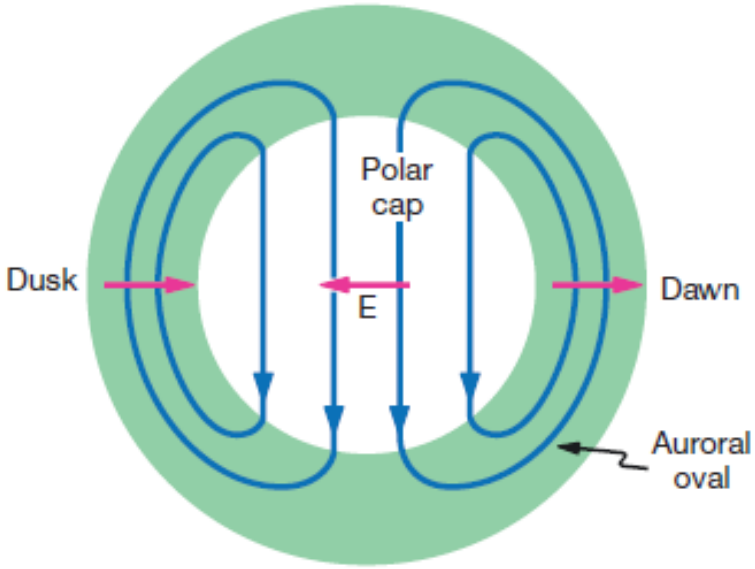

Figure 2.6: Two-cell convection pattern in the high-latitude ionosphere (blue) and associated ionospheric electric fields (pink). (Credit: Baumjohann and Nakamura, 2007)

the two-cell convection pattern can be taken as a two-cell pattern of equipotential contours. This means that the ionospheric electric fields are direction towards dusk in the northern hemisphere polar cap, poleward at the dusk side of the auroral oval, and equatorward at the dawn side of the auroral oval.

Ionospheric conductivity is anisotropic due to the effect of collisions between charge-carriers and neutral atmospheric particles, leading to three distinct conductivities: the field-aligned, Pedersen and Hall conductivities. Thus, the ionospheric electric field will give rise to three types of currents, shown in Figure 2.7. The field-aligned currents flow into and out of the ionosphere, parallel to the magnetic field lines. These include the poleward Region 1 currents, which connect out to and close across the magnetopause, and the equatorward Region 2 currents, which are directed outward from the ionosphere near dawn and into the ionosphere around dusk, and are connected to the partial ring current (part of the ring current). The Pedersen currents flow perpendicular to the magnetic field lines and parallel to the ionospheric electric field, connecting the Region 1 and 2 currents. The Hall currents, as per the

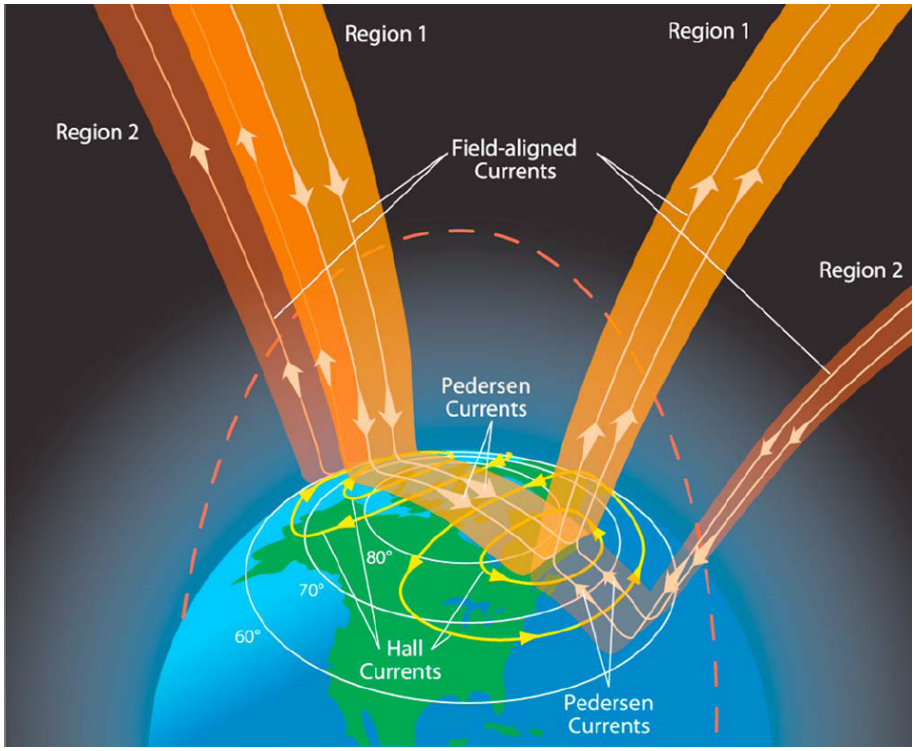

Figure 2.7: Schematic of the current systems flowing through the ionosphere. (Credit: Le et al., 2010)

Hall effect, are perpendicular to both the magnetic field and the ionospheric electric field (Ganushkina et al., 2018).

2.3.4 Auroral Convection Electrojets

The conductivity of the auroral oval is far greater than the polar cap due to enhanced ionisation from precipitating particles. As such, current flow within the high-latitude regions is stronger within the auroral oval, which gives rise to the auroral convection electrojets. The eastward electrojet flows from just eastward of noon and terminates short of midnight where it flows up the magnetic field lines and moves northwards, merging with the westward electrojet. The westward electrojet flows from just westward of noon and terminates just westward of midnight where it also flows up along the magnetic field lines. Both are shown in Figure 2.8. The auroral electrojets are Hall currents, and carry a total current of the same order of magnitude as the

ring current (millions of Ampères) (Baumjohann and Nakamura, 2007). They flow at an altitude of around 100 km.

The Auroral Electrojet (AE) index (Davis and Sugiura, 1966) is a measure of global electrojet activity in the auroral zone. It is derived from the variations in the horizontal component of the magnetic field at around a dozen observatories the northern hemisphere auroral zone. The monthly data for each station are normalised by subtracting the average value of five quiet days at said station from the data obtained there during the month. The data from all stations are then superposed for each given time in Universal Time (UT), and the largest and smallest values are extracted to be the AU and AL indices respectively. The AU index expresses the strongest current intensity of the eastward auroral electrojet, and the AL index expresses the strongest current intensity of the westward auroral electrojet. The difference between these two values (AU−AL), defines the AE index, which, as stated above, represents the overall electrojet activity. The mean of the two values ($\frac{\mathrm{AU+AL}}{2}$) defines the AO index, which is meant to provide a measure of the equivalent zonal current. However, since the magnitude of the eastward and westwards electrojets are often asymmetric, AO is perhaps more accurately described as a measure of the combined effects of this asymmetry and of the ring current Mayaud, 1980.

2.4 Geomagnetic Storms and Substorms

2.4.1 Geomagnetic Storms

As discussed previously, CMEs occur when magnetic reconnection at the Sun sends a cloud of plasma into interplanetary space. These large-scale magnetic structures can contain over 10^{12} kg of coronal material, and are propelled at speeds faster than the background solar wind (over 1000 km s^{-1}). These fast moving CMEs create shock waves ahead of them, able to generate large amounts of SEPs that can damage equipment in space, discussed in more detail below. Due to how they are formed, CMEs often contain loop-like magnetic field structures called flux

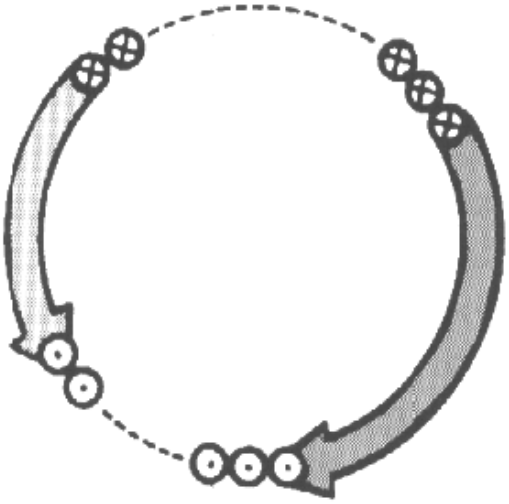

Figure 2.8: Eastward and westward auroral convection electrojets. (Credit: Cravens, 1997)

ropes (or magnetic clouds when referring specifically to CMEs). The magnetic field within a magnetic cloud can have almost any orientation, but when it is southward, it is more geoeffective as it undergoes magnetic reconnection with the northward magnetic field of the Earth. This increases the flow of energy and momentum into the magnetosphere, boosting the rate of convection, enhancing magnetospheric currents and triggering geomagnetic storms.

There are some notable features than can be seen in most geomagnetic storms: a sudden storm commencement (SSC), the main phase, and the recovery phase. The SSC is characterised by an abrupt increase in the horizontal component of the surface geomagnetic field at low and mid latitudes, due to the compression of the magnetosphere by increased solar wind pressure. While this does appear in the Dst index as an increase, the characterisation of SSCs uses a much wider magnetometer network than Dst and are performed separately. Note that not all geomagnetic storms will have a sudden storm commencement, as geomagnetic storms can also arise from prolonged non-CME related southward IMF, or from a SIR. The SSC is followed by a large drop in Dst as the ring current is enhanced, signalling the main phase of the storm. Eventually, the Dst begins to slowly return to a pre-storm level

in what is known as the recovery phase.

2.4.2 Substorms

During periods of prolonged southward-orientated IMF, the reconnection occurring on the dayside of Earth is strongly enhanced. As per the Dungey cycle, the open field lines are pulled downstream by the solar wind to the tail where they undergo reconnection again and the closed field lines return earthwards. This enhanced convection leads to an increase in strength of the eastwards and westwards electrojets. However, the dayside merging rate exceeds that of the magnetotail, so only a portion of flux transported to the tail is reconnected at the magnetic neutral line ($\sim$ 100 Earth radii downstream from Earth). Over time, magnetic field lines begin to build-up, increasing the magnetic flux density and enhancing the cross-tail current in the neutral sheet. This accumulation eventually leads to the formation of a new magnetic neutral line closer to Earth ($\sim$ 20 to 25 Earth radii downstream) (Baker et al., 1996), the field lines undergo rapid magnetic reconnection and the energy is explosively released. This is the substorm onset, and the start of the substorm expansion phase. The plasma between the near-Earth neutral line and the neutral line in the magnetotail is launched down the tail into interplanetary space as a plasmoid. The rapid unloading of magnetic flux stored in the magnetotail leads to formation of the substorm electrojet, which greatly increases the strength of current flow at the high-latitude midnight region. The substorm electrojet experiences a westward and poleward surge during the expansion phase, driven by heavily increased particle precipitation and leading to stunning auroral displays. Unlike the convection electrojets, the substorm electrojet only flows in the midnight sector due to it being the ionospheric closure of the substorm current wedge diverted from the cross tail current via field-aligned currents, shown in Figure 2.9.

There are several differences between substorms and storms. First, substorms occur more frequently than storms (4 times a day on average) and their timescales are shorter than storms, lasting 1-3 hours. Second, substorms are more localised

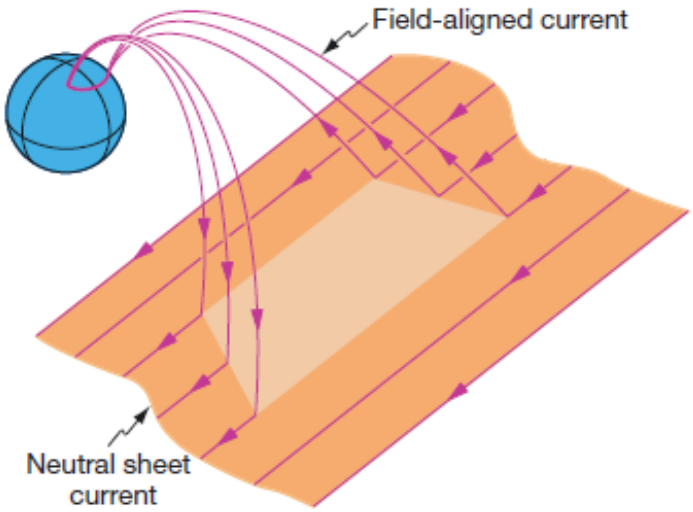

Figure 2.9: Cross tail currents are diverted via-field aligned current, closing across the ionosphere as the substorm electrojet, forming the substorm current wedge. (Credit: Baumjohann and Nakamura, 2007

than storms, largely impacting the nightside of Earth. Third, substorms are not associated an enhancement of the ring current. Substorms can occur in isolation, but multiple substorms will occur during a storm.

2.4.3 Time-Varying Magnetic Fields

Variations in the local magnetic field at the ground are known as dB/dt, and they can be characterised into three types by their origins and timescales (Kataoka and Ngwira, 2016).

The first type arises when the rapid compression of the magnetosphere during a SSC causes global enhancement of dB/dt with a timescale of tens of seconds. The magnitude of these dB/dt are dependent on the solar wind dynamic pressure, this makes them distinct from the two following types, which mainly depend on solar wind speed and the geoeffectiveness of the IMF. This type of dB/dt can be as large as $110\,\mathrm{nT\,s^{-1}}$ at high latitudes and $39\,\mathrm{nT\,s^{-1}}$ at low latitudes.

The second type of dB/dt is associated with ring current evolution, and as such

are well defined by geomagnetic storm phases. These are characterised globally by slow dB/dt values with the timescale of hours, with values in the hundreds of $\mathrm{nT\,h^{-1}}$.

The third and largest type of dB/dt are associated with the electrojets during substorm activity, in which electrojet currents cause fast dB/dt. While they mostly occur in high latitude regions, these effects can extend to middle and low latitudes during extreme events, as described above in section 2.4.2. Values of dB/dt of almost $1200\,\mathrm{nT\,min^{-1}}$ have been observed at middle latitude regions during extreme storms (Viljanen, Ari et al., 2014). Since the electrojets flow in an east-west orientation, their associated dB/dt are orientated in the north-south direction.

Since the largest dB/dt are related to substorm activity, and considering these effects can also impact middle and low latitude regions during extreme events, this means that substorms are a major driver of geomagnetic disturbances in the UK specifically.

2.5 Geomagnetic Induction in the Earth

Time-varying magnetic fields at Earth interact with the electrically conductive rocks below the surface, giving rise to geoelectric fields. The basics of geomagnetic induction in the Earth are covered here, for a more comprehensive analysis, see Mckay (2003).

Since displacement currents can be ignored in geomagnetic induction studies (Weaver, 1994), in a region of uniform conductivity (σ) and permeability (μ), the magnetic field ($\mathbf{B}$) and electric field $\mathbf{E}$ can be represented by the following equations

$$\nabla^2\mathbf{B} + i\omega\mu\sigma\mathbf{B} = 0 \tag{2.9}$$

$$\nabla^2\mathbf{E} + i\omega\mu\sigma\mathbf{E} = 0 \tag{2.10}$$

where ω is the angular frequency, and assuming a harmonic time dependence of $\exp(-i\omega t)$. These equations illustrate the diffusive process of geomagnetic induction in the Earth (Weaver, 1973).

2.5.1 Skin Depth and the Apparent Resistivity

As electromagnetic fields travel though a material, the amplitude of the fields attenuate. The skin depth refers to the distance at which the field amplitudes are reduced to $1/e$ ($\sim 37\%$) of its value on the surface. Skin depth (δ) is given by the equation

$$\delta = \sqrt{\frac{1}{\sigma \mu_0 \mu_r \pi f}} \tag{2.11}$$

where σ is the conductivity, μ_0 is the vacuum magnetic permeability, μ_r is the relative permeability of the material, and f is the circular frequency. This indicates that inside strong magnetic materials (high μ_r) such as iron, the skin depth will be significantly lower, meaning stronger attenuation of the fields.

The measurements of the magnetic and electric fields can be used to map the conductivity structure of the Earth, a method termed magnetotelluric (MT) sounding. Conversely, in regions where conductivity is known, measurements of the dB/dt can be used to estimate geoelectric fields.

Assuming the Earth is a half-space of homogeneous material, we can obtain an expression for apparent resistivity, which while unrealistic, can be helpful in interpreting MT data. Modifying the equation given by Cagniard (1953) for magnetic flux density **B** rather than magnetic field intensity **H** gives the following relationship for apparent resistivity (ρ_A)

$$\rho_A = \frac{\mu_0 \mu_r}{2\pi f} \left| \frac{E_x}{B_y} \right|^2 \tag{2.12}$$

where E_x and B_y are orthogonal components of the electric and magnetic fields respectively.

2.5.2 Magnetotelluric Methodology

When performing an MT measurement, the magnetic and electric fields are assumed to be perpendicular to each other, and thus measured as such. A quantitative example for a MT measurement in 1D is shown in Figure 2.10. Figure 2.10(a) shows

the set up of the magnetic field and electric field sensors to measure **B** (blue) and **E** (red) and the conductivity of the layers below the ground, with a conductive layer shown in pink near the bottom. Figure 2.10(b) shows the amplitudes of the magnetic field (solid red line), electric field (solid blue line), and current density (solid green line) of a 0.5 Hz electromagnetic wave with respect to depth, which increases down the vertical axis from the top. For comparison, the magnetic field for a 5 Hz signal is also shown (dashed red line). The electric field that would be measured if the conductive layer was not present is also given (dotted blue line), representative of the case of the apparent resistivity above. It can be clearly seen that the conductive layer results in a sharp increase in the attenuation of the magnetic field and an enhancement of the electric field due to the increased conductivity.

In MT theory, the horizontal components of **B** and **E** are related by the following relationship

$$\begin{bmatrix} E_x(\omega) \\ E_y(\omega) \end{bmatrix} = \frac{1}{\mu} \begin{bmatrix} Z_{xx}(\omega) & Z_{xy}(\omega) \\ Z_{yx}(\omega) & Z_{yy}(\omega) \end{bmatrix} \begin{bmatrix} B_x(\omega) \\ B_y(\omega) \end{bmatrix} \tag{2.13}$$

or

$$\mathbf{E} = \frac{1}{\mu}\mathbf{Z} \cdot \mathbf{B} + \varepsilon \tag{2.14}$$

where **Z** is referred to as the MT impedance tensor and ε is the noise associated with the data output.

The apparent dimensionality of the geology will determine how the parameters of **Z** differ, as follows

$$\text{1D: } Z_{xx} = Z_{yy} = 0 \text{ and } Z_{xy} = -Z_{yx} \tag{2.15}$$

$$\text{2D: } Z_{xx} = -Z_{yy} \text{ and } Z_{xy} \neq -Z_{yx} \tag{2.16}$$

$$\text{3D: } Z_{xx} \neq Z_{yy} \neq Z_{xy} \neq Z_{yx} \tag{2.17}$$

In 2D, $Z_{xx} = Z_{yy} = 0$ when the coordinate system of the measurements and the geology are aligned. This dimensionality suggests that, since the largest dB/dt caused by the electrojets occur in the north-south orientation, the largest induced electric fields would be expected to be orientated in the east-west direction.

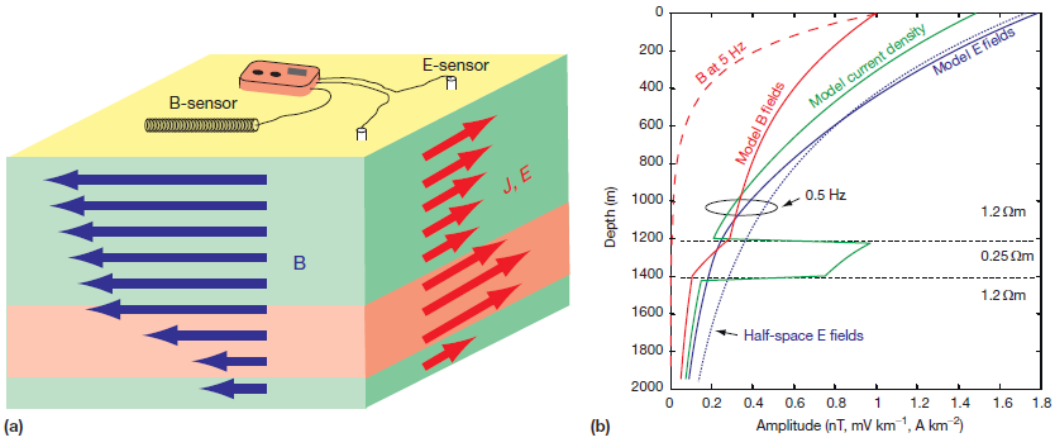

Figure 2.10: (a) Diagram of an MT measurement setup, showing the layers of the ground below the surface, including a conductive layer (pink). (b) The amplitudes of the magnetic field (solid red line), electric field (solid blue line), and current density (solid green line) of a 0.5 Hz electromagnetic wave with respect to depth, which increases down the vertical axis from the top. For comparison, the magnetic field for a 5 Hz signal is also shown (dashed red line). The electric field that would be measured if the conductive layer was not present is also given (dotted blue line). (Credit: Constable, 2015)

2.5.3 Measuring Magnetic Fields

Magnetic observatories use fluxgate magnetometers to measure total magnetic field. A fluxgate magnetometer consists of two circuits. The primary circuit is formed of two coil windings connected in series and wrapped around a common (ring) core of highly magnetically permeable material. The secondary circuit is a coil winding (the sense winding) that encloses the entire primary circuit. They are designed in such a way that when an AC current flows though the primary circuit, the magnetic fields of the two coil winding oppose each other. The current is set at a frequency that will saturate the core. With no external magnetic field applied, the magnetisation of the cores are equal and opposite, meaning there is no net magnetic field to drive a current through the secondary circuit. However, once an external magnetic field is applied, the saturation of the windings de-synchronise, leading to a time-varying net magnetisation that induces a voltage in the sense winding proportional to the external magnetic field strength. Placing three of these devices perpendicular to each other allows for the magnetic field to be measured in three dimensions.

2.5.4 Measuring Electric Fields

The noise generated by metal electrodes excludes them from use in MT measurements for frequencies lower than radio waves. Instead, a non-polarising electrode, or porous pot, is used, which utilises a single chemistry reversible reaction. The contact point is a metal rod suspended in a saturated aqueous solution of that metal's salt (e.g., copper and copper sulfate), and the base of the electrode is made of a porous material such as ceramic or wood, allowing for contact with the ground. The electrodes are buried tens of centimeters deep to minimise temperature changes from impacting the measurements. The electrodes are spaced a few hundred meters apart, but since the electric field signals are so small (of order $\mathrm{mV\,km^{-1}}$), a gain must be applied. When taking MT measurements, it is also important to ensure no ground path exists between the data collection equipment and the electrodes, this is often achieved by an opto-isolator, which transfers electrical signals between two

isolated circuits using light.

2.6 Geomagnetically Induced Currents

Through the various mechanisms detailed in section 2.4.3, the local magnetic field at the ground can vary over different timescales. These dB/dt induce electric fields in conductive infrastructures and the Earth's surface, which drive geomagnetically induced currents (GICs) that have the potential to impact ground-based infrastructure in various ways. GICs are low frequency currents, ranging between 1 mHz to 1 Hz (Oyedokun et al., 2020), hence they are often assumed to be quasi-DC in nature.

Faraday's law provides a relation between the electric field integrated around the loop formed by the conductive structure (e.g., power line, rail), ground connections, and return path through the earth to the rate of change of magnetic flux through the loop. At GIC frequencies, the integral around the loop is very small, which is sometimes mistakenly interpreted to suggest there is no induction. However, it actually shows that the electric field in the structure is equal in magnitude and direction as the electric field across the Earth's surface (Boteler and Pirjola, 2017).

It has been suggested that a 1 minute ($\approx$16 mHz) sampling rate is appropriate for GIC modelling (Pulkkinen et al., 2006), however recent research indicates that this may result in an underestimation of the peak geoelectric field and shifts in the timing of that peak values occur (Trichtchenko, 2021). This work concludes that a 1 second (1 Hz) rate is the most suitable for investigations where the peak values of the geoelectric field and GIC are of concern, such as impacts to railway signalling systems which have reaction times much faster than 1 second.

Magnetic field variations with frequencies similar to that of GICs can penetrate deep into the ground. This means that larger electric fields can occur not only in areas where there are regions of a low conductivity geology such as igneous rock but also in areas where these features are present just below the surface. Near-

surface geological layers need to have a thickness that is a significant fraction of the penetration depth for their conductivity to impact the magnitude of the electric fields (Boteler, 1994).

Over the past few decades, there have been notable instances where GICs have impacted technology. One of the most significant occurred in March 1989, where a geomagnetic storm caused large GICs to be generated within the Hydro-Québec power system in Canada, which led to a blackout that left affected areas without power for several hours and caused widespread effects on power systems in North America and northern Europe (Bolduc, 2002; Boteler, 2019). In the case of the Hydro-Québec power system, the quasi-DC nature of GICs caused transformer saturation, harmonic generation, and increased reactive power consumption. Power grids utilise devices known as static VAR compensators, which regulate transmission voltage to provide fast-acting reactive power to the network, these were tripped out by the harmonics arising from the GICs leading to a network destabilisation, and protection relays shut down the system. GICs can also cause heat generation within transformers, and during the 1989 storm, a transformer at the Salem nuclear power plant in New Jersey, USA, was destroyed due to overheating (Kappenman et al., 1990).

The next chapter will detail how GICs in conducting infrastructure and specifically railway signalling systems can be modelled.

Chapter 3

Modelling Geomagnetic Induction in Railways

3.1 Railway Infrastructures

This section concerns railway infrastructures, including electrification, electrical characteristics of the rails, and signalling systems. While a variety of systems are described here, there will be a focus on 25kV, 50Hz alternating current (AC) electrified configuration fitted with direct current (DC) track circuits for signalling, since these will pertain to the work in this thesis. The parameters provided are mostly specific to the UK, having been sourced from Network Rail standards documents.

3.1.1 Railway Electrification

By the end of the nineteenth century, traditionally horse-drawn trams and trolleys had started to utilise electric traction. Railways, on the other hand, which predominantly utilised steam, were slow to adopt this new method of motive power, especially considering the satisfactory performance of steam, pre-existing support infrastructure, and plentiful coal supplies. However, the increasing use of tunnels, such as those far below the streets of London, meant that lines could not be

sufficiently ventilated to allow for the running of steam engines. Thus, in 1890, the City and South London Railway would become the world's first electric underground railway, utilising a third rail alongside the running rails to provide DC current to power the trains (*The System of Electrification for British Railways*, 1955). This demonstrated the benefits of electric traction as a cleaner and more powerful alternative, and was a major stepping stone towards the London Underground that we know today.

Just prior to the first World War, overhead electrification began to be implemented in small sections. The Lancaster-Morecambe-Heysham line, and then the London, Brighton and South Coast Railway had been fitted with the first AC (6.6kV, 25Hz AC) powered overhead equipment. North Eastern Railway also implemented 1500V DC overhead electrification on the Newport-Shildon line, however the ongoing war meant that focus had drifted from improving the current system to maintaining it.

In the aftermath of the war, electrification continued to grow. One of the first large scale networks was the DC third rail system built by Southern Railway starting in the 1920s, which is still in operation throughout South East England to this day. However, looking towards the future, the amount of variation in systems being developed by different railway companies was a cause for concern. This led to the Standardisation of Electrification Order of 1932, which set 1500V DC overhead systems and 750V DC conductor rails to be the standard for all main line operations.

The late 1950s saw the introduction of the 25kV, 50Hz AC overhead electrification system, taking advantage of improvements to power generation and transmission, with the first large scale upgrade project taking place on the West Coast Main Line (Keenor, 2021). Over the next few decades, with new, cheaper designs for line-side equipment to combat large costs, more and more lines would be converted. Finally, one of the latest improvements to the overhead electrification system was the introduction of auto transformers, which are described in more detail in the next section.

3.1.1.1 Overhead Line Equipment

Overhead line equipment (OLE) refers to the infrastructures (masts, wires, etc) that are used to provide continuous electrical energy to a train, transmitted between a sliding contact connected to the roof of the locomotive and a fixed overhead supply conductor. According to *Network Rail A Guide to Overhead Electrification*: "OLE is also undeniably complex and frankly baffling to the lay person"(Baxter, 2015), so the aim of this section is to introduce the key concepts of overhead electrification and provide context for the configuration of the systems that this thesis focuses on.

Classic System

In the classic system, the power supplied to the OLE is obtained from a Distribution Network Operator (DNO), a local operator responsible for taking power from the National Grid and delivering to end-users. The (up to) 400kV from the National Grid is stepped down to 132kV and transmitted by the DNO to sites close to railway feeder stations, there it is stepped down again to the 25kV required by the OLE. For the classic 25kV system, feeder stations are typically spaced 40 to 60km apart.

The OLE transmits power to the train, and the current was traditionally returned to the supply point via one or more of the rails. However, as described in the previous section, current flowing through a conductor will generate a magnetic field around it with strength proportional to the magnitude of the current. As this is AC current at 50Hz, the direction of the current and hence the direction of the surrounding magnetic field is changing direction 50 times per second. In a perfect system, the current in the OLE and the return current would be equal and opposite, meaning both magnetic fields would cancel each other out. However, since the rails and cross-ties (sleepers) form a conductive path to the ground, some of the return current will flow into the surrounding Earth. Taking this into account, and considering that the return current is also potentially split between the running rails via cross bonding (see section 3.1.2.2), the magnetic field generated by the OLE is not completely cancelled out and dominates the surroundings. This is a problem, since Faraday's

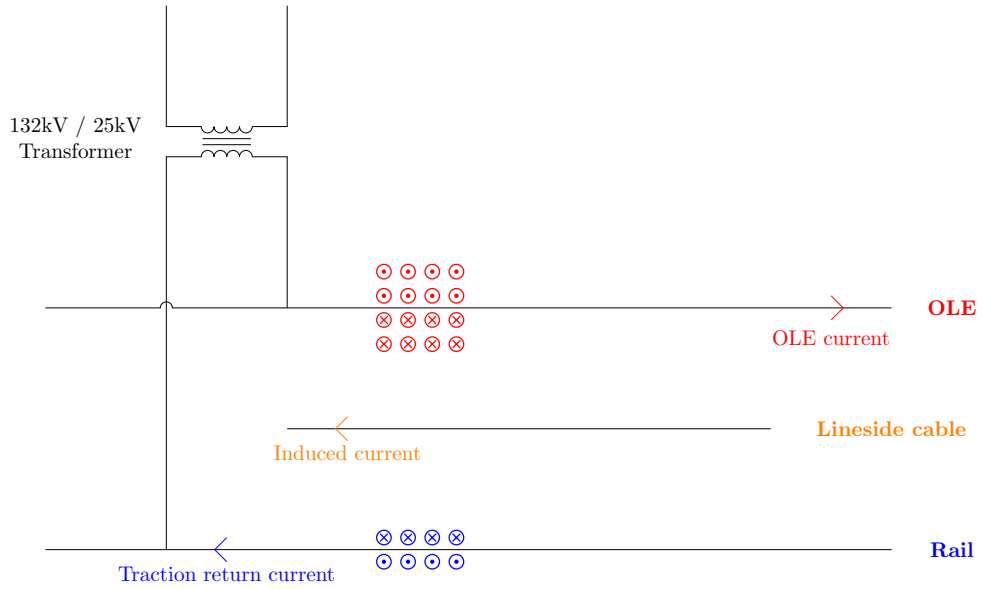

Figure 3.1: Schematic of the classic feeding system. Current in the OLE creates a surrounding magnetic field (shown in red). The traction return current in the rail can leak into the ground, meaning it creates a weaker magnetic field (shown in blue) than the OLE. The time-varying magnetic field surrounding the OLE induces voltages in lineside cables, leading to interference.

law of induction means that this rapidly changing magnetic field will induce voltages in nearby conductors such as signalling and telecommunication cables leading to disruption, as shown in Figure 3.1.

One solution to this problem was implemented in the form of the return conductor (RC) system. The RC is a conductor that runs over the lineside, parallel and at approximately the same height as the OLE. It is insulated from the OLE masts and periodically bonded to the running rails, so a portion of the traction return current will flow through it. Since the RC is around the same height as the OLE, and the current is flowing in the opposite direction to that in the OLE, the magnetic fields surrounding both are opposite in direction, and can cancel each other out. However, the current in the OLE is still larger that that of the RC, and the resultant magnetic field, while smaller, could still be large enough to cause

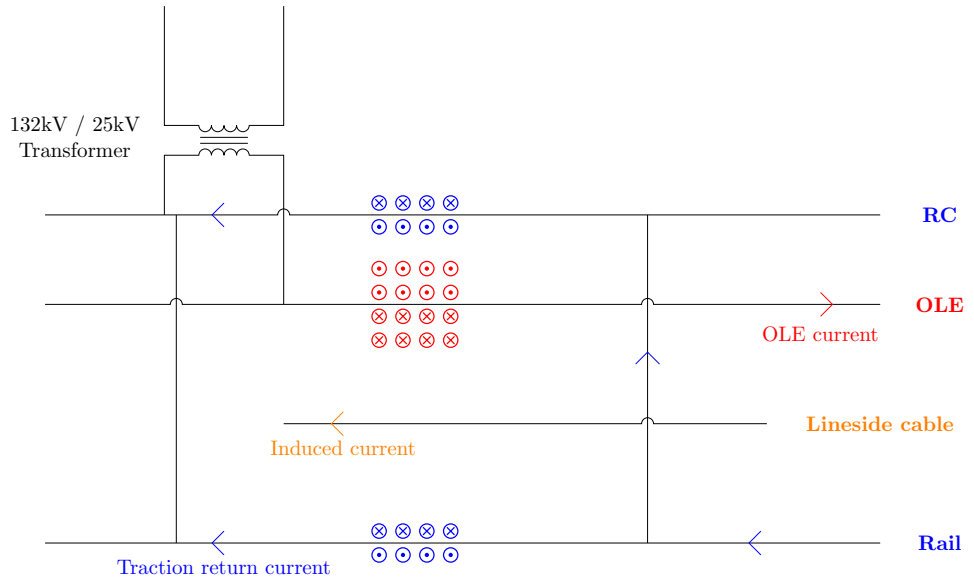

Figure 3.2: Schematic of the classic feeding system with a return conductor. Current in the OLE creates a surrounding magnetic field (shown in red). The traction return current in the rail can leak into the ground, meaning it creates a weaker magnetic field (shown in blue) than the OLE. However, some of the traction return current is split to the RC, which due to its proximity to the OLE, cancels a portion of the OLE magnetic field, having a small immunisation effect. The time-varying magnetic field surrounding the OLE may still be strong enough to induces voltages in lineside cables, leading to interference.

interference, as shown in Figure 3.2.

The RC system can be improved with the inclusion of a booster transformer (BT), which is used to pull all of the traction return current through the RC. The BT is a 1:1 ratio current transformer, with its primary winding connected to the OLE, and the secondary winding connected to the RC. Since the current in the primary winding of the BT (from the OLE) induces an equal and opposite current in the secondary winding (to the RC), considering the circuit, this current can only come from the running rails. Thus, all of the traction return current is diverted through the RC, where the magnetic fields setup around the OLE and the RC are now almost equal and opposite, and will largely cancel each other out and provide an immunising effect on lineside cables, as shown in Figure 3.3.

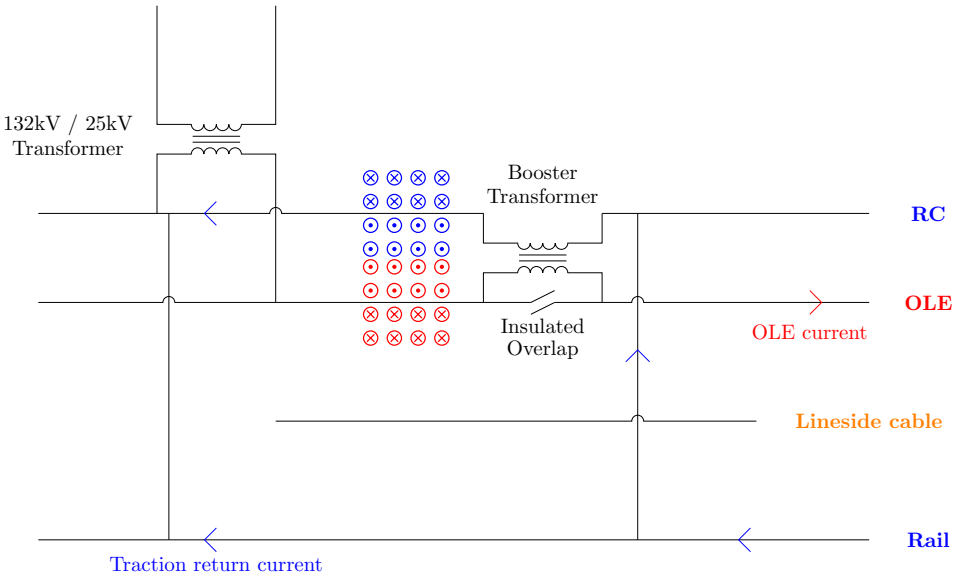

Figure 3.3: Schematic of the classic feeding system with a return conductor and booster transformer. Current in the OLE creates a surrounding magnetic field (shown in red). The traction return current is entirely pulled through the RC by the booster transformer, creating a similar but opposite magnetic field to the OLE, cancelling each other out. This immunisation effect stops voltages from being induced in lineside cables.

Booster transformers are spaced around 5km apart, and their positioning take advantage of the periodic breaks needed in the OLE between lengths of tensioned cables. While their immunising effect are useful, BTs require regular maintenance and increase the impedance of the system, limiting power capacity, As such, there are many routes across the UK that use the RC system without BTs (Keenor, 2021).

Auto Transformer System

A significant improvement over the classic system came in the form of the auto transformer (AT), which provides the system with the greater power availability needed for modern high speed trains. The standard configuration in the UK is 50kV transmission and 25kV supply. Since power is proportional to V^2, by doubling the voltage, we increase the power to four times the classic system. This system also has the advantage of obtaining its transmission voltage directly from the National Grid, reducing the reliance on DNOs, with AT sites typically spaced every 5 to 10km. The extra voltage also means that the number of feeder stations required are greatly reduced compared with the classic system, e.g., along the Great Western Main Line from London to Swansea, there will be only four feeder stations in total along the entire line (Baxter, 2015).

Auto transformers differ in that they only have a single winding as opposed to two. The primary winding is split in two at the midpoint to form the secondary loop, which means a portion of the winding is common to both the primary and secondary sides. For railways, ATs are arranged in parallel along a line, with the OLE connected to one end of the primary winding at +25kV, an auto transformer feeder (ATF) connected to the other end at -25kV, and the traction rail connected to the centre of the winding, as shown in Figure 3.4 for a train drawing current I. The primary current (red), is supplied to the ATs through the OLE and returns through the ATF, so the parallel ATs are all subject to the 50kV primary voltage. Due to the setup of the AT, the portion of the winding that is connected to the secondary loop has half the number of windings as the primary, so the supply voltage across

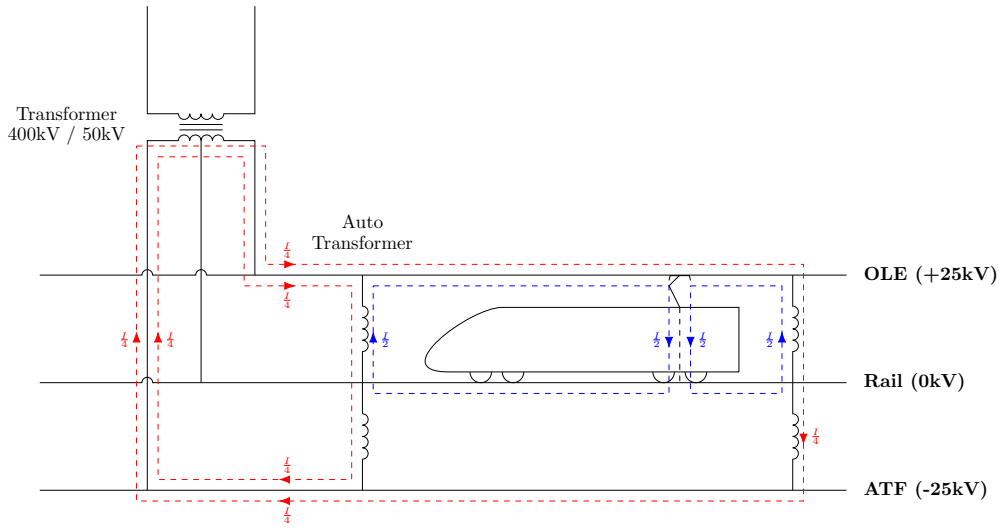

Figure 3.4: Auto transformer system for a railway line showing the flow of currents, with a train drawing current I. The primary currents from the AT feeder station are shown in red, and the secondary currents from the ATs are shown in blue.

the secondary loop will be 25kV, but the current will be doubled. This ensures that the AT system can interface with the classic system, but operate at increased power levels.

The current in the OLE is the sum of the primary currents of all ATs in parallel and the secondary current drawn by the train, and the current in the ATF is the sum of the primary currents of all ATs in parallel only, but in the opposite direction. This allows the ATF to have a similar immunisation effect as the RC in the classic system.

3.1.2 Electrical Characteristics of the Rails

To accurately model the UK railway network, it is important to obtain realistic parameters for the electrical characteristics of the rails, as well as to understand the earthing and bonding arrangements that may influence these values.

3.1.2.1 Rail Resistance

The railway lines being modelled use UIC 60 ($60\,\mathrm{kg\,m^{-1}}$) rail (NR/GN/ELP/27312, 2006), the dimensions are provided by *British Steel: Rail Product Range* (2020) from which a cross-section area of $7600\,\mathrm{mm^2}$ was calculated. We have used a value of $220\,\mathrm{n\Omega\,m}$ for the resistivity of British Steel Grade 700 steel giving a resistance per unit length of the rail as $0.0289\,\Omega\,\mathrm{km^{-1}}$. Mariscotti (2020) and sources therein provide the same value for the per unit length resistance of UIC 60 rail.

3.1.2.2 Earthing and Bonding

The traction rail itself is not entirely continuous since track geometry or safety design features will call for occasional gaps or side switching. In such cases, both sides of each break in the rail are bonded together to ensure a continuous path for traction return current to flow. Figure 3.5 illustrates some of the cases where bonding is needed. These include, but are not limited to, continuity bonds used to bridge expansion joints (designed to account for the thermal expansion that rails experience with seasonal temperature changes), cross bonds (used to connect all traction rails on a line together with a path to ground to ensure low impedance is maintained throughout the line) (NR/SP/ELP/21085, 2007) and transposition bonds (used when the traction rail switches sides). The latter requirement can arise in numerous circumstances, including at turnouts (junctions) where they are needed to avoid the short-circuiting of adjacent track circuits. The traction rail is also bonded to all of the OLE structures, in particular the masts located approximately every 60 m along the rail. The mast foundations connect the whole system to Earth, contributing significantly to the leakage to ground from the traction rail (Keenor, 2021). In this thesis, cross bonds are modelled as wires with a total admittance of $1000\,\mathrm{S}$ ($1\,\mathrm{m\Omega}$) (NR/SP/SIG/50004, 2006).

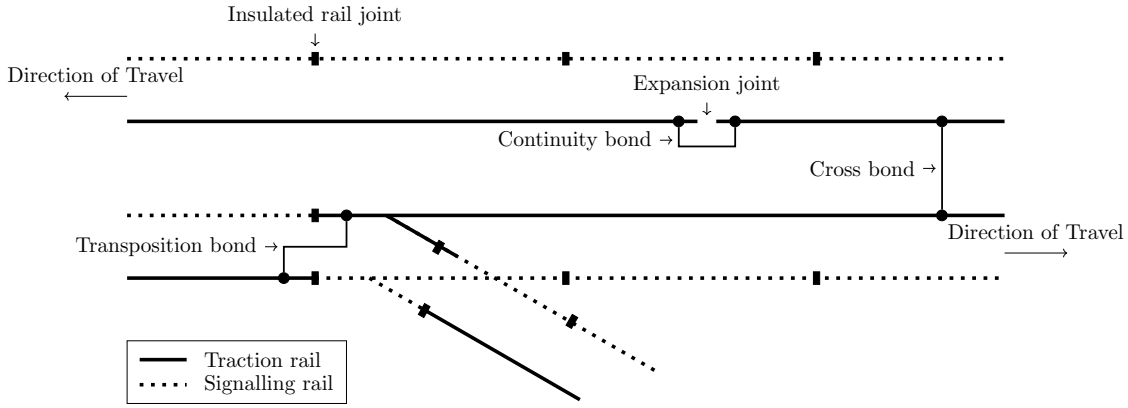

Figure 3.5: A schematic diagram showing the usage of the various bonds required to ensure a continuous path for the current is provided in the traction rail. Along the top traction rail, a continuity bond is used to bridge the gap over an expansion joint designed to protect rails from the effects of thermal expansion during seasonal temperature changes; along the bottom traction rail, transposition bonds are used to temporarily switch the sides of the traction rail due to a turnout (junction) to avoid short-circuiting the track circuit in the branch; connecting both traction rails is a cross bond, designed to ensure voltages are evenly spread across all rails in a line to decrease the hazard of unsafe voltages building up along a rail and provide an alternative path in the case of a broken rail.

3.1.2.3 Leakage

The leakage admittance per unit length of a rail is determined by the rail fastenings, sleepers (crossties) and the ballast, and varies over a wide range due to environmental conditions and underlying ground. NR/GN/ELP/27312 (2006) gives the conventional figure for leakage admittance used by Network Rail to be $0.125\,\mathrm{S\,km^{-1}}$, however, the configuration of the rails means that the signalling and traction rails have different leakage admittance. The signalling rails have insulating pads that reduce leakage, giving a leakage admittance of $0.1\,\mathrm{S\,km^{-1}}$; the traction rails are bonded to OLE structures, this results in a much larger leakage admittance of $1.6\,\mathrm{S\,km^{-1}}$. Another factor that must be considered is the additional leakage from earth mats bonded to the traction return circuit at feeder stations, these structures increase the total leakage by 10 S for each feeder station (NR/SP/SIG/50004, 2006). The leakage admittance of the rails can also vary depending on environmental conditions. The leakage admittance of the signalling rail can range between $0.025\,\mathrm{S\,km^{-1}}$ when dry to $0.4\,\mathrm{S\,km^{-1}}$ when wet. For the traction rail, the leakage admittance ranges from $1.53\,\mathrm{S\,km^{-1}}$ when dry to $2.0\,\mathrm{S\,km^{-1}}$ when wet.

3.1.3 Signalling Systems

The evolution of the UK railway network over time has led to a wide variety of signalling systems being implemented, often depending on the electrification system (or lack thereof) used on the line in question. As technology has evolved, not all lines have been upgraded to the latest system, leading to a diverse and complex collection of signalling infrastructures across the network.

3.1.3.1 Track Circuits

Track circuits are one of the main signalling systems used to detect trains along a railway line, with an estimate of over 50,000 in use across the UK railway network

(Knight-Percival et al., 2020).

DC Track Circuits

In a DC track circuit, insulated rail joints (IRJ) are spaced along one of the rails (the signalling rail) which separates it into blocks; the traction rail is not broken into sections as it provides the return path for the traction current used to power the train. A relay is positioned at the start of the block (relative to the direction of travel) which forms a circuit via the signalling and traction rails to a power supply at the end of the block. The power supply energises the relay which causes a green signal to be displayed, indicating there is no train present, as shown in Figure 3.6(a). However, if a train is occupying the block, the wheels and axle redirect the current before it can reach the relay and it is not energised, leading to a red signal that indicates a train is present, as shown in Figure 3.6(b). The lengths of track circuit blocks can vary depending on if the section is located in a rural or an urban area.

AC Track Circuits

AC track circuits operate very similarly to DC track circuits, but in place of the DC power supply, the source provides an AC current with frequency higher than 50Hz to avoid interference from the traction return current. At the relay end, a band-pass filter and a rectifier are used to convert the AC signal into DC to operate the relay. As with DC track circuits, the relay is energised when the block is unoccupied, and de-energises when the axles of the train in entering the block causes the current to bypass the relay.

Audio Frequency Track Circuits

Similar to an AC track circuit, but operating at frequencies much higher than 50Hz (in the range of hundreds to thousands of Hz), an audio frequency track circuit (AFTC) eliminates the need for IRJs. Adjacent sections can be programmed to transmit at a range of frequencies, and the relays can be programmed to only respond to those transmitted by the supply in its section. As IRJs are difficult to

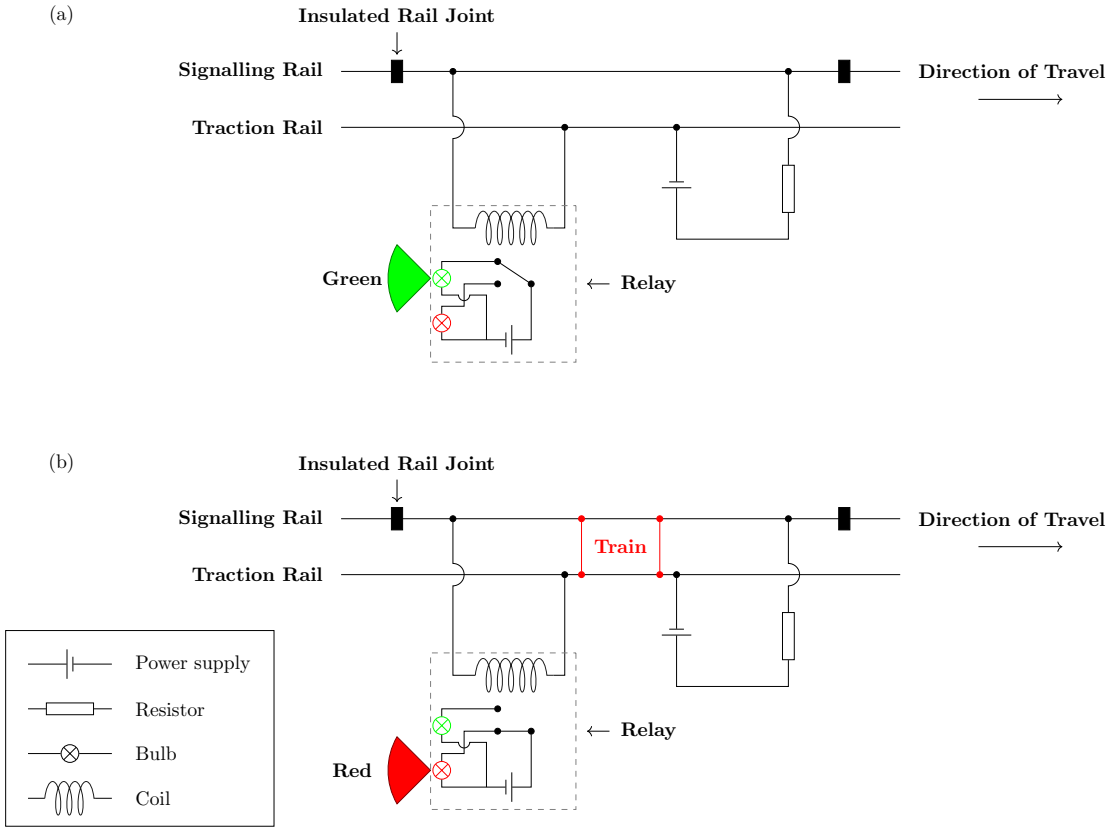

Figure 3.6: Circuit diagram of a railway signalling track circuit for a single block along a network in the cases of (a) the absence of a train in the block and (b) a train occupying the block. Insulated rail joints separate each block from its neighbours, while the continuous rail is connected across all blocks. A relay is connected to the side of the circuit from which the train enters (left in this case), formed of resistors and an electromagnet. A power supply and an accompanying resistor to protect it from short-circuiting is on the far end of the block (right in this case). In (a), the electromagnet is energised by the power supply, causing the switch to be in the configuration to display a green light, indicating the section is clear. When a train enters the block, as in (b), flows through the wheels and axle of the train instead of the relay causing the electromagnet to be de-energised, and the switch falls to the configuration that displays a red light, indicating the section is occupied.

maintain and prone to issues if current can leak across them, AFTCs are a notable improvement.

3.1.3.2 Axle Counters

While track circuits all operate based on the principle of a closed circuit, with the relay being de-energised when the trains are occupying the blocks they control, axle counters utilise a counting system. A system of transmitters and receivers are placed at the start and end of a signalling section, these are calibrated to count the number of wheels that pass through the axle counter. If the number of counts at the start of the section is equal to the number of counts at the end, then the block is designated as empty, and vice versa. The counting is achieved by the transmitter generating a strong, localised magnetic field around itself, which induces a voltage in the opposite side to be picked up by the receiver. When a wheel passes between the two, there is a drop in the induced voltage due to the wheel effectively reducing the flux that reaches the receiver. The extent of the voltage change can be used to define limits for the system to detect when wheels have passed through.

Axle counters do present some disadvantages over track circuits. First, if there is a disruption to axle counter system (such as power loss), then there is the potential for missed counts or information loss that could lead to signalling misoperations. Second, when workers are performing maintenance on track circuited lines, it is common to use jumper leads to connect the two rails together, simulating the axles of a train, and setting the signal to red to allow them to work safely. This cannot be done on axle counter controlled sections.

3.2 Geomagnetic Induction Modelling

This section covers the background theory and methodology of modelling geomagnetic induction in rails, and how to incorporate track circuit components to construct a network that can be used to determine the current flowing across the signalling

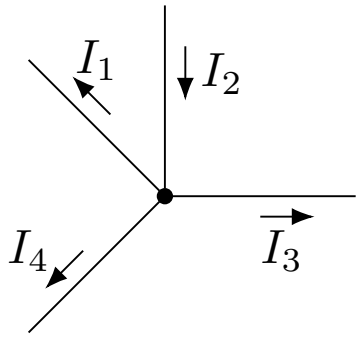

Figure 3.7: Currents flowing into and out from a node in an electrical circuit.

system relays in normal conditions and given an external electric field.

3.2.1 Kirchhoff's Laws and Ohm's Law

Kirchhoff's Laws are the name given to two laws that describe the behaviour of current and voltage in electrical circuits.

3.2.1.1 Kirchhoff's Current Law

Kirchhoff's current law (KCL), also known as Kirchhoff's first law, states that the sum of all currents flowing into a node in an electrical circuit is equal to the sum of all currents flowing out from that node.

For the case shown in Figure 3.7, KCL is applied as such

$$I_2 = I_1 + I_3 + I_4 \tag{3.1}$$

This can be generalised to the following

$$\sum_{k=1}^{N} I_k = 0 \tag{3.2}$$

where N is the total number of branches, with currents flowing into the node designated as positive, and currents flowing out from the node as negative.

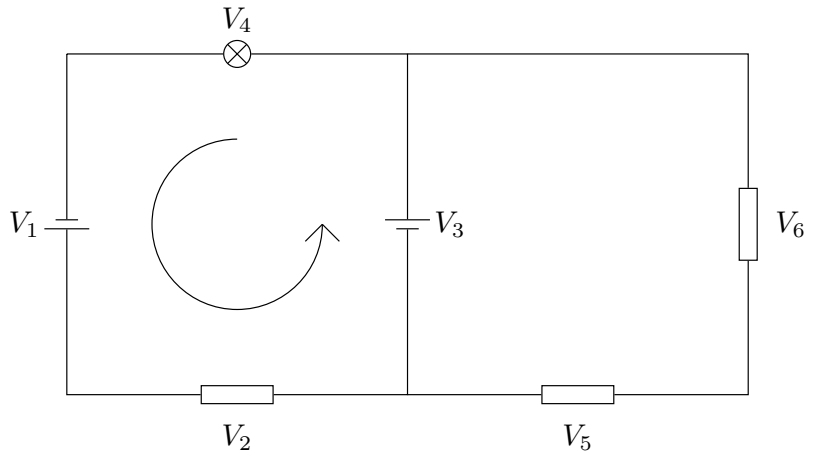

Figure 3.8: Circuit diagram showing the closed loop to be used with Kirchhoff's voltage law.

3.2.1.2 Kirchhoff's Voltage Law

Kirchhoff's voltage law (KVL), also known as Kirchhoff's second law, states that sum of all voltages (potential differences) around any closed loop in an electrical circuit is equal to zero.

For the example shown in Figure 3.8, KVL is applied as such

$$V_1 - V_2 + V_3 - V_4 = 0 \tag{3.3}$$

This can be generalised to the following

$$\sum_{k=1}^{N} V_k = 0 \tag{3.4}$$

where N is the total number of voltages in the circuit.

When using KVL, it is important to deduce the direction of the current through each component, as that determines whether the voltage contribution to the loop is positive or negative.

3.2.1.3 Ohm's Law

Ohm's Law (OL) states that the current flowing through a conductor between two points I is proportional to the voltage across those two points V, the constant

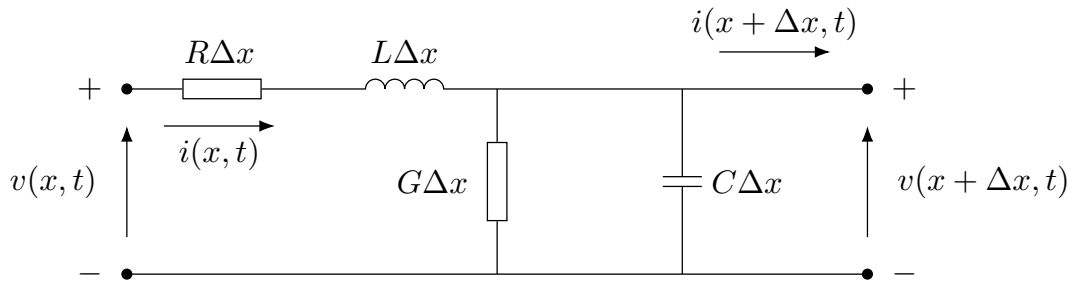

Figure 3.9: Infinitesimal section Δx of a transmission line showing resistance R, inductance L, capacitance C, and conductance G. The voltage and current at the left end are $v(x,t)$ and $i(x,t)$ respectively, and the voltage and current at the right end are $v(x+\Delta x,t)$ and $i(x+\Delta x,t)$ respectively.

of proportionality is called the resistance R. Ohm's law can be represented mathematically as

$$V = IR \tag{3.5}$$

3.2.2 Transmission Line Theory

Transmission line theory is an area of electrical engineering that describes how the voltage and current along a line are related to its electrical characteristics (Heaviside, 1876; Heaviside, 1892). It begins with representing the transmission line as an infinite number of infinitesimal sections, each containing components that represent the parameters of the line. These parameters are the resistance R describing the resistive losses along the line, represented by a series resistor and measured in ohms per unit length; the inductance L due to the magnetic field generated by the current, represented by a series inductor, and measured in henries per unit length; the capacitance C due to the ability of the transmission line to store electrical energy, represented by a parallel capacitor, and measured in farads per unit length; and the conductance G describing the conductive losses, represented by a parallel resistor, and measured in siemens per unit length, shown in Figure 3.9.

The series and parallel components respectively can be combined to give series

impedance Z and parallel admittance Y with equations

$$Z = R + j\omega L \tag{3.6}$$

$$Y = G + j\omega C \tag{3.7}$$

where j is the unit imaginary number. The propagation constant γ, which represents the rate at which a signal travels along the transmission line, is given by

$$\gamma = \sqrt{ZY} \tag{3.8}$$

The characteristic impedance Z_0, which is equivalent to the impedance of the transmission line if it had infinite length, is given by

$$Z_0 = \sqrt{\frac{Z}{Y}} \tag{3.9}$$

3.2.2.1 Telegrapher's Equations

Applying KVL to the electrical circuit of section Δx of the transmission line (Figure 3.9), taking the loop from the left end of the line past $R\Delta x$ and $L\Delta x$ and back through the right end of the line, we get the following equation

$$v(x,t) - (R\Delta x)i(x,t) - (L\Delta x)\frac{\partial}{\partial t}i(x,t) - v(x+\Delta x,t) = 0 \tag{3.10}$$

Rearranging the non-voltage terms to the right and dividing by Δx we get

$$-\frac{v(x+\Delta x,t) - v(x,t)}{\Delta x} = Ri(x,t) + L\frac{\partial}{\partial t}i(x,t) \tag{3.11}$$

Then taking the limit as $\Delta x \to 0$ gives

$$-\frac{\partial}{\partial x}v(x,t) = Ri(x,t) + L\frac{\partial}{\partial t}i(x,t) \tag{3.12}$$

Applying KCL to the right end of the line, we get

$$i(x,t) - (G\Delta x)v(x+\Delta x,t) - (C\Delta x)\frac{\partial}{\partial t}v(x+\Delta x,t) - i(x+\Delta x,t) = 0 \tag{3.13}$$

Rearranging the non-current terms to the right and dividing by Δx we get

$$-\frac{i(x+\Delta x,t) - i(x,t)}{\Delta x} = Gv(x+\Delta x,t) + C\frac{\partial}{\partial t}v(x+\Delta x,t) \tag{3.14}$$

Again, taking the limit as $\Delta x \to 0$ gives

$$-\frac{\partial}{\partial x}i(x,t) = Gv(x,t) + C\frac{\partial}{\partial t}v(x,t) \tag{3.15}$$

Equations 3.12 and 3.15 are called the telegrapher's equations in the time domain, which if given the electrical characteristics of the transmission line and boundary conditions, can be used to determine the voltage and current along the line. These equations can be simplified by expressing them in the phasor representation, where phasors V(x) and I(x) are defined as

$$v(x,t) = \Re\{V(x)e^{j\omega t}\} \tag{3.16}$$

$$i(x,t) = \Re\{I(x)e^{j\omega t}\} \tag{3.17}$$

where $\Re$ denotes the real part of the complex equation. From these we get

$$\begin{aligned}\frac{\partial}{\partial x}v(x,t) &= \frac{d}{dx}\Re\{V(x)e^{j\omega t}\} \\ &= \Re\{[\frac{d}{dx}V(x)]e^{j\omega t}\}\end{aligned} \tag{3.18}$$

such that

$$\frac{\partial}{\partial x}v(x,t) = \frac{d}{dx}V(x) \tag{3.19}$$

and

$$\begin{aligned}\frac{\partial}{\partial t}i(x,t) &= \frac{d}{dt}\Re\{I(x)e^{j\omega t}\} \\ &= \Re\{\frac{d}{dt}[I(x)e^{j\omega t}]\} \\ &= \Re\{[j\omega I(x)]e^{j\omega t}\}\end{aligned} \tag{3.20}$$

such that

$$\frac{\partial}{\partial t}i(x,t) = j\omega I(x) \tag{3.21}$$

Substituting equations 3.19 and 3.21 into equations 3.12 and 3.15, we get

$$-\frac{d}{dx}V(x) = [R + j\omega L]I(x) \tag{3.22}$$

and

$$-\frac{d}{dx}I(x) = [G + j\omega C]V(x) \tag{3.23}$$

which are the telegrapher's equations in phasor representation. Finally, substituting equations 3.6 and 3.7 to combine the series and parallel components and rearranging, we get

$$\frac{d}{dx}V(x) + ZI(x) = 0 \tag{3.24}$$

and

$$\frac{d}{dx}I(x) + YV(x) = 0 \tag{3.25}$$

3.2.2.2 Distributed Source Transmission Line Theory

To enable the study of the geomagnetic induction in the rails, the transmission line equations shown above are extended to include voltage sources E distributed along the rail which represent the induced electric field, this is known as distributed source transmission line (DSTL) theory (Schelkunoff, 1938; Boteler, 1997; Boteler, 2021). With this additional voltage source, equation 3.24 becomes

$$\frac{d}{dx}V(x) + ZI(x) = E \tag{3.26}$$

Differentiating and substituting equations 3.26 and 3.25 into each other, and using the expression for the propagation constant γ given in equation 3.8, we get

$$\frac{d^2}{dx^2}V(x) - \gamma^2 V(x) = \frac{d}{dx}E \tag{3.27}$$

and

$$\frac{d^2}{dx^2}I(x) - \gamma^2 I(x) = 0 \tag{3.28}$$

Assuming that the electric field is constant along this section of the rail, then $\frac{d}{dx}E = 0$, and equation 3.27 becomes

$$\frac{d^2}{dx^2}V(x) - \gamma^2 V(x) = 0 \tag{3.29}$$

The solutions to equations 3.29 and 3.28 are

$$V = Ae^{\gamma x} + Be^{-\gamma x} \tag{3.30}$$

and

$$I = \frac{E}{\gamma Z_0} - \frac{A}{Z_0}e^{\gamma x} + \frac{B}{Z_0}e^{-\gamma x} \tag{3.31}$$

where A and B depend on the conditions at the end of the line. See appendix A.1 for proof.

Taking the start of line to be i, where $x = 0$, equations 3.30 and 3.31 become

$$V_i = A + B \tag{3.32}$$

and

$$I_i = \frac{E}{\gamma Z_0} - \frac{A}{Z_0} + \frac{B}{Z_0} \tag{3.33}$$

Taking the end of the line to be k, where $x = L$, equations 3.30 and 3.31 become

$$V_k = Ae^{\gamma L} + Be^{-\gamma L} \tag{3.34}$$

and

$$I_k = \frac{E}{\gamma Z_0} - \frac{A}{Z_0}e^{\gamma L} + \frac{B}{Z_0}e^{-\gamma L} \tag{3.35}$$

Equations 3.32 and 3.34 can be used to obtain expressions for A and B

$$A = \frac{V_k - V_i e^{-\gamma L}}{e^{\gamma L} - e^{-\gamma L}} \tag{3.36}$$

$$B = \frac{V_i e^{\gamma L} - V_k}{e^{\gamma L} - e^{-\gamma L}} \tag{3.37}$$

with the proof given in appendix A.2.

Substituting the expressions for A and B into equations 3.30 and 3.31 gives

$$V = (\frac{V_k e^{\gamma L} - V_i}{e^{\gamma L} - e^{-\gamma L}})e^{-\gamma(L-x)} + (\frac{V_i e^{\gamma L} - V_k}{e^{\gamma L} - e^{-\gamma L}})e^{-\gamma x} \tag{3.38}$$

$$I = -\frac{1}{Z_0}(\frac{V_k e^{\gamma L} - V_i}{e^{\gamma L} - e^{-\gamma L}})e^{-\gamma(L-x)} + \frac{1}{Z_0}(\frac{V_i e^{\gamma L} - V_k}{e^{\gamma L} - e^{-\gamma L}})e^{-\gamma x} + \frac{E}{\gamma Z_0} \tag{3.39}$$

A and B can also be expressed in terms of V_i and I_i by rearranging equation 3.33 and substituting into equation 3.32

$$A = \frac{V_i}{2} - \frac{1}{2}(Z_0 I_i - \frac{E}{\gamma}) \tag{3.40}$$

$$B = \frac{V_i}{2} + \frac{1}{2}(Z_0 I_i - \frac{E}{\gamma}) \tag{3.41}$$

Substituting these expressions for A and B in equations 3.34 and 3.35 gives the voltage and current at the end of the line in terms of the voltage and current at the start of the line

$$V_k = V_i \cosh(\gamma L) - I_i Z_0 \sinh(\gamma L) + \frac{E}{\gamma} \sinh(\gamma L) \tag{3.42}$$

$$I_k = -\frac{V_i}{Z_0} \sinh(\gamma L) + I_i \cosh(\gamma L) - \frac{E}{\gamma Z_0}(\cosh(\gamma L) - 1) \tag{3.43}$$

with the proof given in appendix A.3.

3.2.3 Equivalent Pi-Circuits

To obtain a network model of track circuits as a whole, we will need to combine the transmission line models of multiple rail sections together. To simplify this process, an equivalent circuit (like that seen in Figure 3.9) can be converted to what is known as a π-circuit or pi-circuit. This is done by splitting the parallel admittance into two equal parts and placing them at either end of the circuit, as shown in Figure 3.10, where Z', Y', and E' are the total series impedance, parallel admittance, and voltage source due to the electric field in the section rather than the 'per unit length' values of Z, Y, and E.

Using KCL at node A and KVL around the clockwise loops between i and the left hand parallel admittance, k and the right hand parallel admittance, and between both parallel admittances, we can obtain an expression for V_k in terms of V_i and I_i

$$V_k = (1 + \frac{Y'Z'}{2})V_i - Z'I_i + E' \tag{3.44}$$

with the proof given in appendix A.4.

Equation 3.44 can be compared to equation 3.42 to obtain the following expressions

$$Z' = Z_0 \sinh(\gamma L) \tag{3.45}$$

$$\frac{Y'}{2} = (\cosh(\gamma L) - 1)\frac{1}{Z_0 \sinh(\gamma L)} \tag{3.46}$$

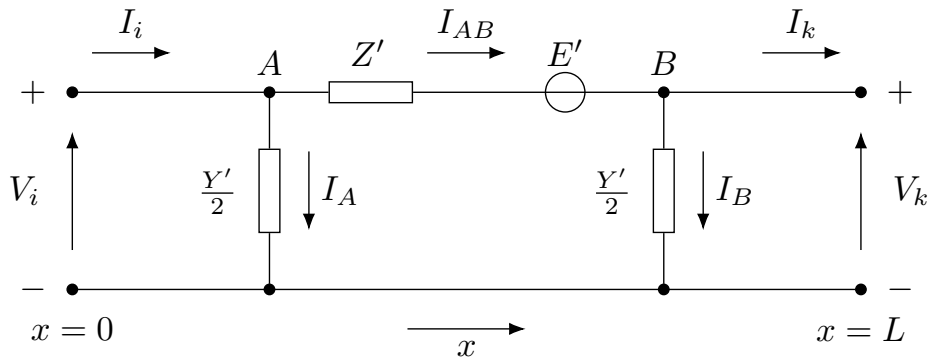

Figure 3.10: The equivalent pi-circuit of rail between i at $x = 0$ and k at $x = L$, with series impedance Z', voltage source due to the electric field E', and parallel admittances $\frac{Y}{2}$ at either end.

$$E' = \frac{E}{\gamma} \sinh(\gamma L) \tag{3.47}$$

The series impedance Z' and voltage source due to the electric field E' can also be represented as a series admittance Y_E and equivalent current source I_E, given by

$$Y_E = \frac{1}{Z_0 \sinh(\gamma L)} \tag{3.48}$$

and

$$I_E = \frac{E}{Z} \tag{3.49}$$

With these equations, all of the parameters of an equivalent pi-circuit can be calculated.

3.2.4 Nodal Admittance Network

To model a rail in its entirety, the equivalent pi-circuits of connected sections can be combined to form a nodal admittance network. For example, take a rail that consists of three sections (A, B, and C), as shown in Figure 3.11a. The leftmost and rightmost nodes of the circuit do not have any connected sections, so the admittance connected to them can remain the same. However, for the nodes in between (e.g., the right node of A and the left node of B), adjacent parallel admittances can be

summed together and the nodes merged into one. The nodes in the new network can then be numbered from 0 upwards, as shown in Figure 3.11b, where the new terms are defined as

$$y_0 = \frac{y'_A}{2} \qquad\qquad y_3 = \frac{y'_C}{2} \tag{3.50}$$

for the parallel admittances connected to nodes at the end, and

$$y_1 = \frac{y'_A}{2} + \frac{y'_B}{2} \qquad\qquad y_2 = \frac{y'_B}{2} + \frac{y'_C}{2} \tag{3.51}$$

for the parallel admittances connected to nodes in between. The series admittances of the equivalent pi-circuits become the series admittances of the sections in the new nodal admittance network

$$y_{01} = y_A \qquad y_{12} = y_B \qquad y_{23} = y_C \tag{3.52}$$

as do the equivalent current sources

$$j_{01} = j_A \qquad j_{12} = j_B \qquad j_{23} = j_C \tag{3.53}$$

which are henceforth denoted by j to differentiate them from the total current i.

The DC track circuits analysed in this thesis consist of a power supply at one end of the section, and a relay at the other end. The power supply can be represented by a voltage source V_{power} and a resistor Z_{power} connected in series that protects it during short circuit conditions. However, to be consistent with the other components in the network, this can be converted to an admittance y_{power} and equivalent current source j_{power} by the same method as before, with

$$j_{power} = \frac{V_{power}}{Z_{power}} \qquad\qquad y_{power} = \frac{1}{Z_{power}} \tag{3.54}$$

The relay can be represented as an impedance Z_{relay}, which can be similarly converted to an admittance y_{relay}

$$y_{relay} = \frac{1}{Z_{relay}} \tag{3.55}$$

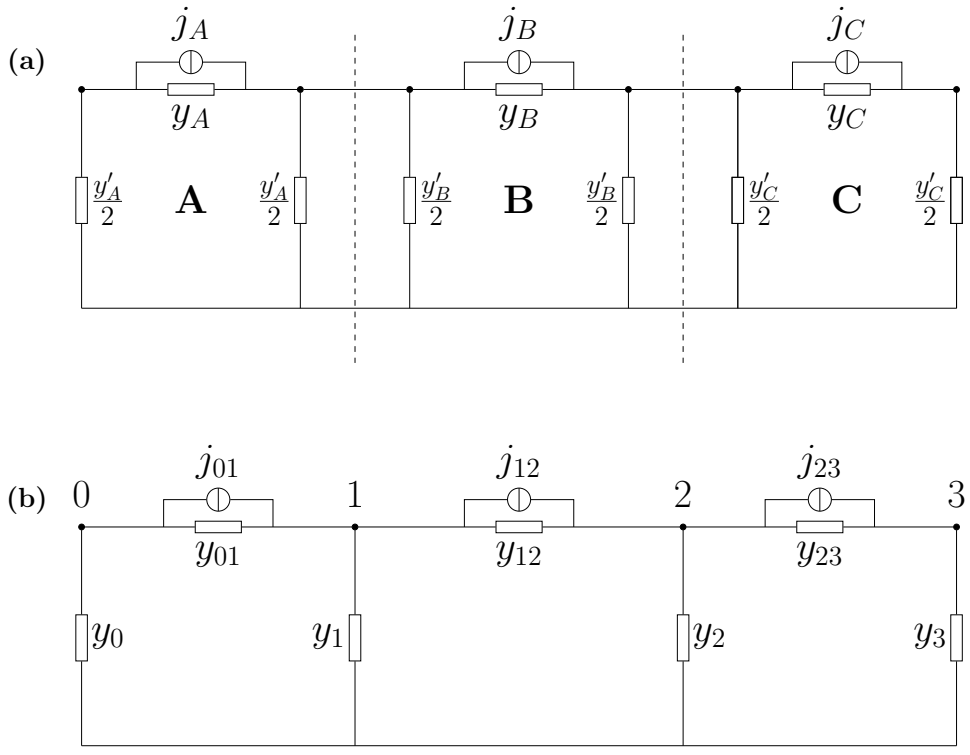

Figure 3.11: Converting equivalent pi-circuits to a nodal admittance network.

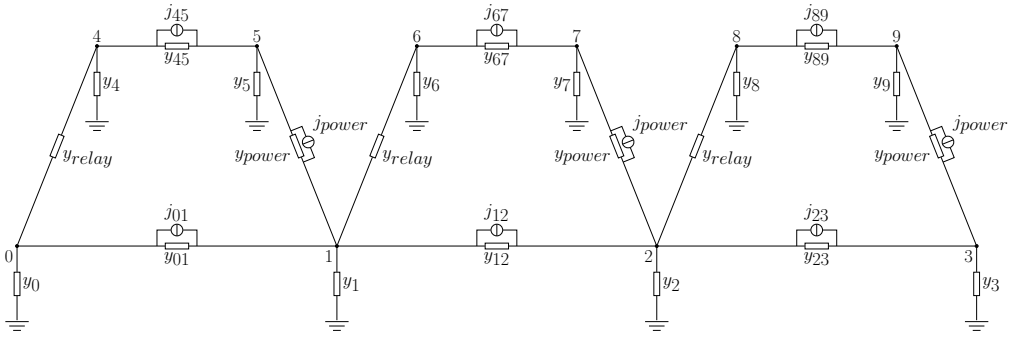

Figure 3.12: Circuit diagram showing the nodal admittance network of three blocks. Track circuit blocks are separated by insulated rail joints in one rail but share a continuous traction rail. The components making up the network are the equivalent current source and admittance of the power supply (j_{power} and y_{power} respectively), the admittance of the relay (y_{relay}), the admittance to the ground at each node n (y_n), the admittance due to the rail between nodes n and m, (y_{nm}), and the equivalent currents induced in the rails due to the geoelectric field between nodes n and m, (j_{nm}). Note that the y_n, y_{nm} and j_{nm} are dependent on the length of the segment and the rail's electrical characteristics, and would have varying values.

3.2.5 Track Circuit Modelling

Combining the rails and track circuit components together allows us to complete the nodal admittance networks for a track circuit or series of track circuits. Consider a railway line with three blocks, each with a track circuit, as shown in Figure 3.12. Nodes 0, 1, 2, and 3 are along the continuous traction return rail, whereas nodes 4, 5, 6, 7, 8, 9 are along the individual signalling rails, which (as described above) are separated by IRJs, hence why there are no connections between 5-6 or 7-8. The track circuit relays connect nodes 0-4, 1-6, and 2-8, and the power supplies connect nodes 1-5, 2-7, and 3-9.

To calculate the voltages of the nodes, first we need to apply KCL to each of the nodes in the network, this gives the following relationships

$$-i_{04} - i_{01} - i_0 = 0 \tag{3.56a}$$

$$i_{01} - i_{15} - i_{16} - i_{12} - i_1 = 0 \tag{3.56b}$$

$$i_{12} - i_{27} - i_{28} - i_{23} - i_2 = 0 \tag{3.56c}$$

$$i_{23} - i_{39} - i_3 = 0 \tag{3.56d}$$

$$i_{04} - i_{45} - i_4 = 0 \tag{3.56e}$$

$$i_{45} + i_{15} - i_5 = 0 \tag{3.56f}$$

$$i_{16} - i_{67} - i_6 = 0 \tag{3.56g}$$

$$i_{67} + i_{27} - i_7 = 0 \tag{3.56h}$$

$$i_{28} - i_{89} - i_8 = 0 \tag{3.56i}$$

$$i_{89} + i_{39} - i_9 = 0 \tag{3.56j}$$

The current flowing in each line can be given as the sum of the equivalent current sources along the line and the product of the voltage between the nodes and the line admittance as per OL, this gives

$$i_{01} = (v_0 - v_1)y_{01} + j_{01} \tag{3.57a}$$

$$i_{12} = (v_1 - v_2)y_{12} + j_{12} \tag{3.57b}$$

$$i_{23} = (v_2 - v_3)y_{23} + j_{23} \tag{3.57c}$$

$$i_{04} = (v_0 - v_4)y_{04} \tag{3.57d}$$

$$i_{45} = (v_4 - v_5)y_{45} + j_{45} \tag{3.57e}$$

$$i_{15} = (v_1 - v_5)y_{15} + j_{power} \tag{3.57f}$$

$$i_{16} = (v_1 - v_6)y_{16} \tag{3.57g}$$

$$i_{67} = (v_6 - v_7)y_{67} + j_{67} \tag{3.57h}$$

$$i_{27} = (v_2 - v_7)y_{27} + j_{power} \tag{3.57i}$$

$$i_{28} = (v_2 - v_8)y_{28} \tag{3.57j}$$

$$i_{89} = (v_8 - v_9)y_{89} + j_{89} \tag{3.57k}$$

$$i_{39} = (v_3 - v_9)y_{39} + j_{power} \tag{3.57l}$$

Once again using OL, we know that the current to the ground i_n at any node n is given by

$$i_n = v_n y_n \tag{3.58}$$

we can substitute this and equations 3.57 into equations 3.56, giving

$$-(v_0 - v_4)y_{04} - (v_0 - v_1)y_{01} - j_{01} = v_0 y_0 \tag{3.59a}$$

$$(v_0-v_1)y_{01}+j_{01}-(v_1-v_5)y_{15}-j_{power}-(v_1-v_6)y_{16}-(v_1-v_2)y_{12}-j_{12} = v_1 y_1 \tag{3.59b}$$

$$(v_1-v_2)y_{12}+j_{12}-(v_2-v_7)y_{27}-j_{power}-(v_2-v_8)y_{28}-(v_2-v_3)y_{23}-j_{23} = v_2 y_2 \tag{3.59c}$$

$$(v_2 - v_3)y_{23} + j_{23} - (v_3 - v_9)y_{39} - j_{power} = v_3 y_3 \tag{3.59d}$$

$$(v_0 - v_4)y_{04} - (v_4 - v_5)y_{45} - j_{45} = v_4 y_4 \tag{3.59e}$$

$$(v_4 - v_5)y_{45} + j_{45} + (v_1 - v_5)y_{15} + j_{power} = v_5 y_5 \tag{3.59f}$$

$$(v_1 - v_6)y_{16} - (v_6 - v_7)y_{67} - j_{67} = v_6 y_6 \tag{3.59g}$$

$$(v_6 - v_7)y_{67} + j_{67} + (v_2 - v_7)y_{27} + j_{power} = v_7 y_7 \tag{3.59h}$$

$$(v_2 - v_8)y_{28} - (v_8 - v_9)y_{89} - j_{89} = v_8 y_8 \tag{3.59i}$$

$$(v_8 - v_9)y_{89} + j_{89} + (v_3 - v_9)y_{39} + j_{power} = v_9 y_9 \tag{3.59j}$$

Rearranging so that the current source terms are on the left and the other terms are grouped on the right gives

$$-j_{01} = (y_0 + y_{04} + y_{01})v_0 - y_{01}v_1 - y_{04}v_4 \tag{3.60a}$$

$$j_{01}-j_{power}-j_{12} = -y_{01}v_0+(y_1+y_{01}+y_{15}+y_{16}+y_{12})v_1-y_{12}v_2-y_{15}v_5-y_{16}v_6 \tag{3.60b}$$

$$j_{12}-j_{power}-j_{23} = -y_{12}v_1+(y_2+y_{12}+y_{27}+y_{28}+y_{23})v_2-y_{23}v_3-y_{27}v_7-y_{28}v_8 \tag{3.60c}$$

$$j_{23} - j_{power} = -y_{23}v_2 + (y_3 + y_{23} + y_{39})v_3 - y_{39}v_9 \tag{3.60d}$$

$$-j_{45} = -y_{04}v_0 + (y_4 + y_{04} + y_{45})v_4 - y_{45}v_5 \tag{3.60e}$$

$$j_{45} + j_{power} = -y_{15}v_1 - y_{45}v_4 + (y_5 + y_{45} + y_{15})v_5 \tag{3.60f}$$

$$-j_{67} = -y_{16}v_1 + (y_6 + y_{16} + y_{67})v_6 - y_{67}v_7 \tag{3.60g}$$

$$j_{67} + j_{power} = -y_{27}v_2 - y_{67}v_6 + (y_7 + y_{67} + y_{27})v_7 \tag{3.60h}$$

$$-j_{89} = -y_{28}v_2 + (y_8 + y_{28} + y_{89})v_8 - y_{89}v_9 \tag{3.60i}$$

$$j_{89} + j_{power} = -y_{39}v_3 - y_{89}v_8 + (y_9 + y_{89} + y_{39})v_9 \tag{3.60j}$$

where the left-hand side of the equation is now the sum of the equivalent current sources directed into each node n, which we take to be J_n, so

$$J_0 = (y_0 + y_{04} + y_{01})v_0 - y_{01}v_1 - y_{04}v_4 \tag{3.61a}$$

$$J_1 = -y_{01}v_0 + (y_1 + y_{01} + y_{15} + y_{16} + y_{12})v_1 - y_{12}v_2 - y_{15}v_5 - y_{16}v_6 \tag{3.61b}$$

$$J_2 = -y_{12}v_1 + (y_2 + y_{12} + y_{27} + y_{28} + y_{23})v_2 - y_{23}v_3 - y_{27}v_7 - y_{28}v_8 \tag{3.61c}$$

$$J_3 = -y_{23}v_2 + (y_3 + y_{23} + y_{39})v_3 - y_{39}v_9 \tag{3.61d}$$

$$J_4 = -y_{04}v_0 + (y_4 + y_{04} + y_{45})v_4 - y_{45}v_5 \tag{3.61e}$$

$$J_5 = -y_{15}v_1 - y_{45}v_4 + (y_5 + y_{45} + y_{15})v_5 \tag{3.61f}$$

$$J_6 = -y_{16}v_1 + (y_6 + y_{16} + y_{67})v_6 - y_{67}v_7 \tag{3.61g}$$

$$J_7 = -y_{27}v_2 - y_{67}v_6 + (y_7 + y_{67} + y_{27})v_7 \tag{3.61h}$$

$$J_8 = -y_{28}v_2 + (y_8 + y_{28} + y_{89})v_8 - y_{89}v_9 \tag{3.61i}$$

$$J_9 = -y_{39}v_3 - y_{89}v_8 + (y_9 + y_{89} + y_{39})v_9 \tag{3.61j}$$

Equations 3.61 can be represented in matrix form as

$$\begin{bmatrix} J_0 \\ J_1 \\ \vdots \\ J_8 \\ J_9 \end{bmatrix} = \begin{bmatrix} y_0 + y_{04} + y_{01} & -y_{01} & \dots & 0 & 0 \\ -y_{01} & y_1 + y_{01} + y_{15} + y_{16} + y_{12} & \dots & 0 & 0 \\ \vdots & \vdots & \ddots & \vdots & \vdots \\ 0 & 0 & \dots & y_8 + y_{28} + y_{89} & -y_{89} \\ 0 & 0 & \dots & -y_{89} & y_9 + y_{89} + y_{39} \end{bmatrix} \begin{bmatrix} v_0 \\ v_1 \\ \vdots \\ v_8 \\ v_9 \end{bmatrix} \tag{3.62}$$

with the full matrix given in appendix B.1.

The matrix containing the admittances is termed the admittance matrix $[Y]$, and this is multiplied by the matrix of voltages $[V]$ to give the matrix of currents $[J]$, as follows

$$[J] = [Y][V] \tag{3.63}$$

To obtain the voltages at each node, we can multiply both sides of equation 3.63 by the inverse of the admittance matrix, giving

$$[Y]^{-1}[J] = [Y]^{-1}[Y][V]$$

$$[V] = [Y]^{-1}[J] \tag{3.64}$$

Using similar methodology, we can obtain the general equations for a network. Applying KCL to each node m in a network, we get

$$\sum_{n=0}^{N} i_{nm} + i_m = 0 \qquad\qquad (n \neq m) \tag{3.65}$$

where N is the maximum node index.

As with equations 3.57, the current i_{nm} flowing in the line between nodes n and m is given as

$$i_{nm} = j_{nm} + (v_n - v_m)y_{nm} \tag{3.66}$$

where j_{nm} and y_{nm} are the equivalent current source and admittance between nodes n and m, and v_n and v_m are the voltages at nodes n and m respectively.

Substituting this and equation 3.58 into equation 3.65, we get

$$\sum_{n=0}^{N} j_{nm} + \sum_{n=0}^{N}(v_n - v_m)y_{nm} = v_m y_m \qquad\qquad (n \neq m) \tag{3.67}$$

where y_m is the admittance to ground at node m, and $\sum_{n=0}^{N} j_{nm}$ is equal to the sum of all current sources into node m, such that

$$J_m = \sum_{n=0}^{N} j_{nm} \qquad\qquad (n \neq m) \tag{3.68}$$

Equation 3.68 can be substituted into equation 3.67 and rearranged to give

$$J_m = v_m y_m + \sum_{n=0}^{N} v_m y_{nm} - \sum_{n=0}^{N} v_n y_{nm} \tag{3.69}$$

which can be represented in matrix form as $[J] = [Y][V]$ (equation 3.63).

Dissecting the nodal admittance matrix $[Y]$, we can see that the diagonal terms Y_{mm} are given by the sum of all admittances connected to that node, this can be represented as

$$Y_{mm} = y_m + \sum_{n=0}^{N} y_{nm} \qquad (n \neq m) \tag{3.70}$$

and the off-diagonal terms Y_{nm} are equal to the negative of the admittances between the nodes, give to be

$$Y_{nm} = -y_{nm} \qquad (n \neq m) \tag{3.71}$$

Once the equations are solved for the nodal voltages $[V]$, the potential difference across the relays can be calculated by taking the difference in voltage between the nodes on either side of the relays. For the network in Figure 3.12

$$\text{Leftmost relay: } V_{relay} = V_4 - V_0 \tag{3.72a}$$

$$\text{Middle relay: } V_{relay} = V_6 - V_1 \tag{3.72b}$$

$$\text{Rightmost relay: } V_{relay} = V_8 - V_2 \tag{3.72c}$$

Using OL, the current flowing across each relay can then be calculated

$$\text{Leftmost relay: } I_{relay} = \frac{V_4 - V_0}{R_{relay}} \tag{3.73a}$$

$$\text{Middle relay: } I_{relay} = \frac{V_6 - V_1}{R_{relay}} \tag{3.73b}$$

$$\text{Rightmost relay: } I_{relay} = \frac{V_8 - V_2}{R_{relay}} \tag{3.73c}$$

In summary, each rail is first modeled as a transmission line with series impedance and parallel admittance corresponding to the resistance of the rail and the leakage to ground respectively. Next, the transmission line of each rail is converted to a number of individual equivalent pi-circuits, each representing a single block. The equivalent-pi circuits of adjacent blocks are then combined, with the connection

points represented as single nodes, to form a nodal network. To complete the nodal network, the power supply and relay components are added, and this connects both rails together. The impedances in the network are then converted to admittances, and the nodal admittance matrix $[Y]$ is constructed. In $[Y]$ the diagonal terms are equal to the sum of all admittances connected to the node corresponding to that index, and the off-diagonal terms are given by the negative of the admittance between nodes. The admittances between each pair of nodes that are not connected (such as where the IRJs separate the signalling rails) are set at zero. The induced electric field is then added as individual voltage sources distributed between the nodes of each block, and the voltage sources are converted to equivalent current sources. The sum of equivalent current sources directed into each node are then calculated to form $[J]$ (a matrix of nodal equivalent current sources). The nodal voltages are obtained by inverting the matrix $[Y]$ and multiplying by the nodal equivalent current sources $[J]$. The potential difference across the relay is given by the difference between the signaling rail and traction rail nodal voltages on either side of the relay, from which the current flowing across the relay is calculated. The current across the relay is therefore defined as positive when it flows from the signaling rail to the traction rail.

Chapter 4

"Right Side" Failures

The following chapter contains published work from the article:
Patterson, C. J., Wild, J. A., & Boteler, D. H. (2023a). Modeling the impact of geomagnetically induced currents on electrified railway signaling systems in the United Kingdom. *Space Weather*, *21*(3), e2022SW003385. https://doi.org/10.1029/2022SW003385

This chapter advances recent theoretical work on GICs in railway signalling systems by modelling realistic railway lines with parameters from current industrial standards. Focusing on two example lines in the United Kingdom with different locations and orientation, a range of uniform electric fields are simulated along each modelled line. The results show that misoperations could be caused by geomagnetic interference at disturbance levels expected to recur over timescales of several decades. We also demonstrate that the UK estimate for the geoelectric field induced by a 1-in-100 year extreme storm would be strong enough to cause widespread signal misoperations in both lines studied.

4.1 Introduction

As described in the previous chapter, space weather poses a risk to infrastructure in space and on the ground. GICs are one of the foremost space weather hazards.

During geomagnetic disturbances, fluctuating ionospheric currents produce changes to the magnetic fields observed at the Earth's surface. As described by Faraday's Law of Induction, this rapidly changing magnetic field drives electric currents in the Earth and through grounded conductors such as power transmission networks (Boteler, 2014; Lewis et al., 2022; Pirjola, 1985), oil and gas pipelines (Boteler and Trichtchenko, 2015; Pulkkinen et al., 2002) and railways (Darch et al., 2014).

Section 4.2 provides an overview of track circuit railway signalling systems and the mechanisms via which they can be impacted by space weather. Section 4.3 gives the electrical characteristics of the rails and the track circuit parameters used in the model, based on specifications from current United Kingdom industry standards. Section 4.4 introduces the two routes of the UK railway network being studied in this chapter. Section 4.4.1 discusses factors that must be considered depending on whether an entire railway line, or only a portion of the line, is being modelled. The aspects of a railway line's design which contribute the most to space weather susceptibility are also examined. In Section 4.4.2, uniform electric fields are applied to both routes to find the threshold electric field strength needed to cause misoperations. Both lines are then subjected to uniform electric fields with strength known to have led to misoperations in Sweden in the recent past, and finally for a 1-in-100 year extreme event.

4.2 Track Circuits

The operational principles for track circuits are covered in the Section 3.1.3.1, and briefly recapped here.

IRJs are spaced along one of the rails (the signalling rail) which separates it into blocks, the other rail (the traction rail) is not broken into sections as it provides the return path for the traction current used to power the train. A relay is positioned at the start of the block (relative to the direction of travel) which forms a circuit via the signalling and traction rails to a power supply at the end of the block. The power

supply energises the relay which causes a green signal to be displayed, indicating there is no train present. However, if a train is occupying the block, the wheels and axle redirect the current before it can reach the relay and it is not energised, leading to a red signal that indicates a train is present.

The lengths of track circuit blocks and the traction rail can vary depending on if the section is located in a rural or an urban area. The two lines investigated in this study had a range of track circuit block lengths from 0.4−1.9 km and traction rail lengths of around 34 km and 76 km; for comparison, values for the Swedish railway studied by Alm (2020) and Lejdström and Svensson (2020) were 1 km and 4 km for track circuit blocks and 100 km for the traction rail.

By design, the normal operation of a track circuit relay requires it to energise or de-energise at specific current thresholds. This balance can be offset by geomagnetically induced currents which can either work to de-energise a relay in a block with no train present causing a "right side failure" (a mode of failure that does not compromise the safety of trains) or energise a relay in a block with a train present causing a "wrong side failure" (one which does compromise the safety of trains).

4.3 Rail and Track Circuit Properties

Obtaining realistic values for the electrical characteristics of an AC railway network is crucial to analysing the impacts of GICs in DC signalling systems to the best degree of accuracy. The sections of track considered in this chapter are 2-track with single-rail return and no earth wires, where 2-track means that there are two pairs of rails side-by-side, one for each direction of travel. The electrical characteristics of the rails used for the modelling in this thesis are detailed in Section 3.1.2 and summarised in Table 4.1.

Track circuit parameters, including power supply and relay components, vary across the world and even within a specific country, with many different types of

Table 4.1: Electrical characteristics of the rails and parameters for track circuit components.

Rail Resistance	($\Omega\,\mathrm{km}^{-1}$)
Signalling rail	0.0289
Traction rail	0.0289
Leakage	($\mathrm{S}\,\mathrm{km}^{-1}$)
Signalling rail (wet)	0.4
Traction rail (wet)	2.0
Signalling rail (moderate)	0.1
Traction rail (moderate)	1.6
Signalling rail (dry)	0.025
Traction rail (dry)	1.530
Track Circuit Parameters	
Power supply	10 (V)
Power supply resistor	7.2 (Ω)
Relay coil resistance	20 (Ω)
Pick-up current	0.081 (A)
Drop-out current	0.055 (A)

equipment and configurations being used. For the UK lines, we obtained the relevant data from the Network Rail Standards Portal. In this study, we have used the combination of 'BR867 AC Immune DC Track Feed Unit' (NR/BR/867, 1990) and the 'BR939A Miniature Tractive Armature AC Immune DC Neutral Track Relay' (NR/BR/939A, 1971). This represents the preferred design according to the most recent Network Rail standards (NR/PS/SIG/11755, 2000). The side of the track circuit from where the train enters consists of a 10 V power supply in series with a 7.2 Ω resistor to limit the current when short-circuited by the locomotive, the far end consists of the relay coil with a resistance of 20 Ω. The pickup current of the relay is 0.081 A with the dropout current being 68 per cent of that value at 0.055 A, this means when the current flowing through an energised relay drops below 0.055 A, the relay will be de-energised and for it to be energised again, the current will need to exceed 0.081 A.

4.4 Results

4.4.1 Railway Line Modelling

The geographical data for the railway lines studied, i.e., the longitudes and latitudes of points along the line were obtained from OpenStreetMap. The lengths of track circuit blocks and hence their start and end points were estimated using Network Rail Sectional Appendices and the railway tracking website Traksy (https://traksy.uk/live). Once the lines were separated into blocks, the orientation of each block in the line was calculated and used to determine the parallel electric field component along each line segment.

The sections of the railway network chosen for this study are introduced in Figure 4.1: the 76 km Glasgow to Edinburgh via Falkirk line and a 34 km portion of the West Coast Main Line (WCML) from Preston to Lancaster. Both lines are electrified with 50 Hz AC at 25 kV. The two sections were selected for their different orientation (east-west for the Glasgow to Edinburgh line and north-south for the

Preston to Lancaster section of the WCML) and different geological terrane. Each track circuit is assumed to consist of one relay at the start of the block (relative to the direction of travel) and one power supply at the end of the block. For details of the model, please see Section 3.2.

4.4.1.1 Modelling a Section of a Line

When modelling track circuits within a section of traction rail that extends beyond the area of study such as the Preston to Lancaster segment of the WCML, the entire length of the rail must be represented in the model to provide a valid voltage profile along the traction rail section and accurate current values across the relays. To more accurately model the geomagnetic interference on the Preston to Lancaster section, $310\times1\,\mathrm{km}$ blocks before the section and $230\times1\,\mathrm{km}$ blocks after the section were included in the model, with orientation representative of the general line geometry of the WCML. The Preston to Lancaster section of the line still uses the original estimated block lengths, which range from $0.6-1.8\,\mathrm{km}$. Figure 4.2 compares the voltage profiles along the section of traction rail between Preston and Lancaster when (1) the ends of the traction rail are set at Preston and Lancaster and (2) the ends of the traction rail are extended to encompass the entire WCML using the method detailed above. A northwards electric field of strength $-2\,\mathrm{V\,km^{-1}}$ is applied in both cases. It can be seen that the voltage profile is significantly different if the entire length of the traction rail is not considered. If detailed information about the adjacent rail sections is not available, but the adjacent rails are uniform and nearly straight, they can be represented by an equivalent 'active termination' (Boteler, 1997) where the external portion of the rail is a single voltage source and series resistance connected to ground. Calculations with active terminations to represent the northern and southern sections of the WCML give almost identical results to those from calculations including the additional representative sections beyond the area of study, thus active terminations are used from this point on to reduce the computational complexity of the code.

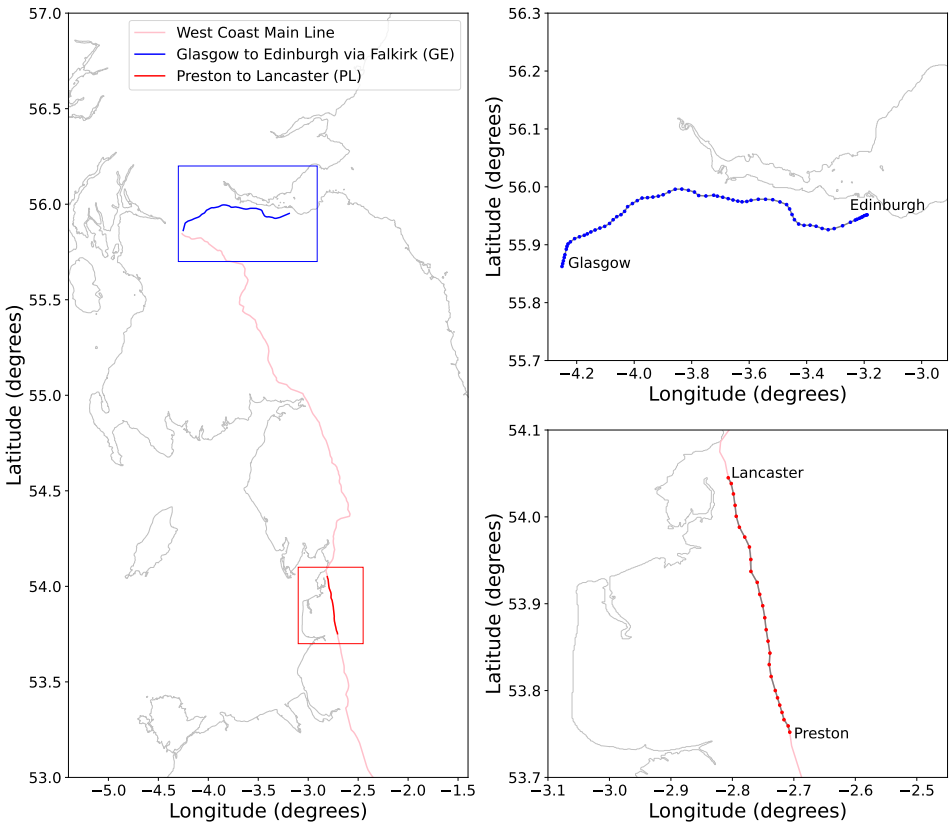

Figure 4.1: A geographic map of a northern portion of the United Kingdom showing both chosen railway lines for study in this chapter with areas of interest highlighted and enhanced (top right and bottom right) to show the locations of signals. The top line (blue) is the Glasgow to Edinburgh line, stretching in an east-west orientation; the bottom line (red) is a portion of the WCML from Preston to Lancaster, with the extension beyond those sections displayed in pink, stretching in a north-south orientation.

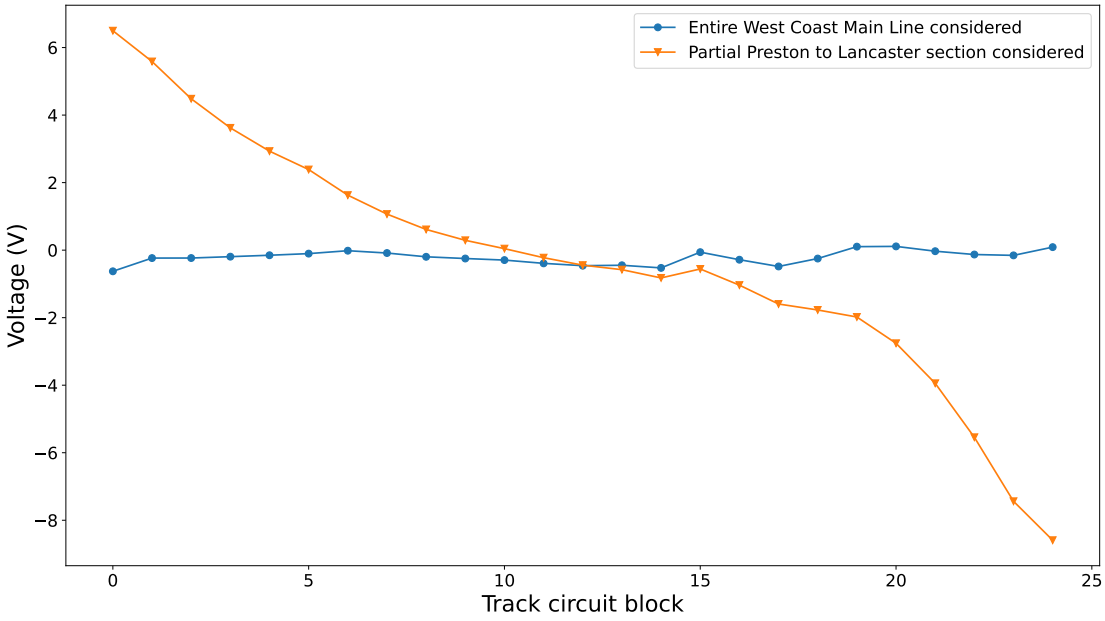

Figure 4.2: The voltage profiles along the traction rail in the southwards direction between Preston and Lancaster with different termination conditions. A northwards electric field of strength $-2\,\mathrm{V\,km^{-1}}$ is applied in both cases. The orange line with triangles shows the voltage profile where the traction rail ends have been set at Preston and Lancaster; the blue line with dots shows the profile where the traction rail has been extended with $310\times1\,\mathrm{km}$ blocks south of Preston and $230\times1\,\mathrm{km}$ blocks north of Lancaster with orientations representative of the general line geometry to account for the portions of the WCML beyond the area of study.

4.4.1.2 Modelling the Entire Line

The methodology described above is suitable for analysing portions of lines that do not include either or both ends of the traction rail. But additional considerations have to be made when modelling the entire traction rail due to the effects of the ends of the line. To demonstrate this, a simplified track circuit model has been produced, consisting of $70 \times 1\,\mathrm{km}$ blocks all orientated directly westwards. The track circuit voltage has been set to zero, allowing us to examine the effects of only the induced currents. Figure 4.3 shows the voltage profiles and nodal voltages along the traction rail and each of the signalling rails when an eastward electric field of $-2\,\mathrm{V\,km^{-1}}$ is applied. The short thin lines illustrate how rail voltage is neither constant from node-to-node nor continuous across nodes. The potential differences across the relays in each track circuit block are shown in a separate panel. The voltage profiles along the traction rail and signalling rails agree with the characteristic electrically long and electrically short profiles as shown in Boteler (2021), respectively. It can be seen that with a constant uniform electric field applied, the nodal voltages of the traction rail and signalling rails, although having different minima and maxima, decrease along the line, following a sideways S-shaped curve. At the left end of the line, the voltages start at their maximum point, decreasing to a central plateau. At a point near the right end of the line, the nodal voltages of both rails converge, causing the potential difference across the relay to be zero. Closer to the right end of the line the polarity of the potential difference is reversed. It can also be seen that the location of the crossover point where the potential difference reverses remains constant regardless of the electric field strength applied. In Figure 4.4, the crossover point can be seen at track circuit block 64, and beyond that point the polarity of the currents is reversed.

Considering this from a mathematical point of view: we know that the nodal voltages are the result of matrix multiplication between the inverse of the admittance matrix ($[Y]^{-1}$) and the equivalent current sources ($[J]$). When we increase or decrease the electric field strength (E), we are only changing the values of $[J]$,

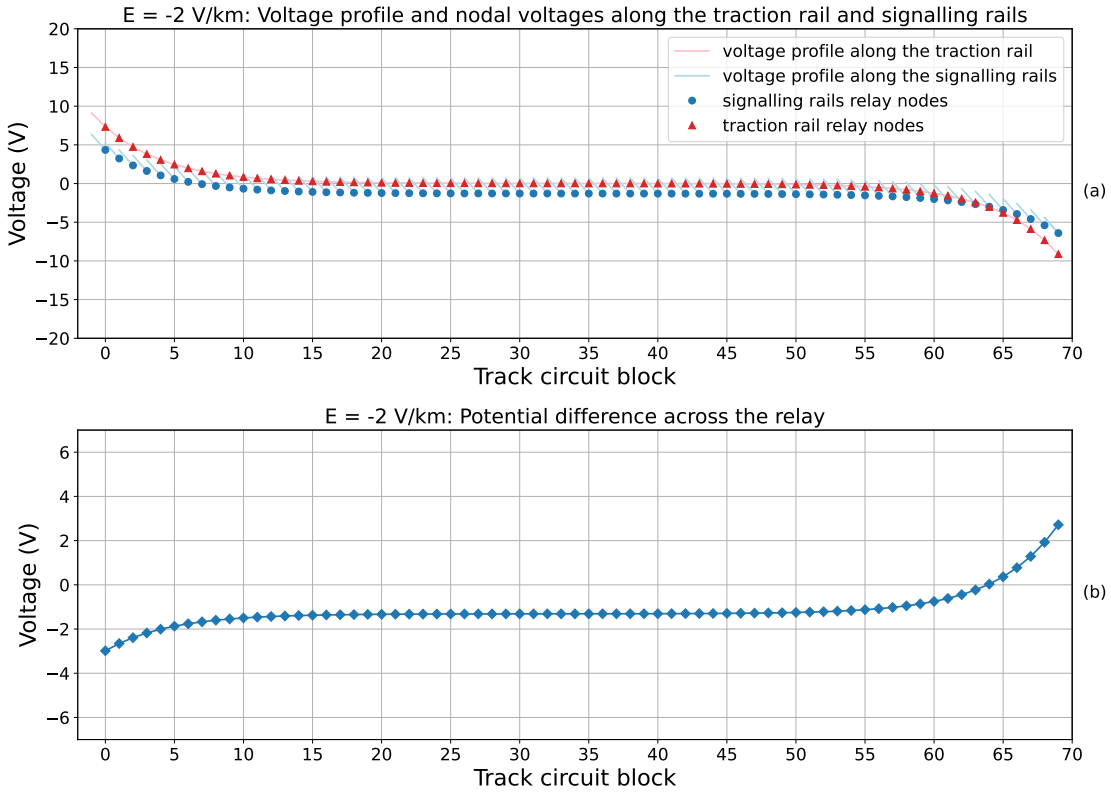

Figure 4.3: Parameters in a network of 70×1 km blocks facing directly westwards, where the track circuit voltage is set to zero. For an electric field strength of $-2\,\mathrm{V\,km^{-1}}$: (a) the voltage profiles and nodal voltages along the traction rail (red triangles) and signalling rails (blue dots) and (b) the potential difference across the relays along the line (blue diamonds). The point at which the signalling rail voltage and traction rail voltage are equal and hence the point at which the potential difference is zero occurs at the same location regardless of electric field strength.

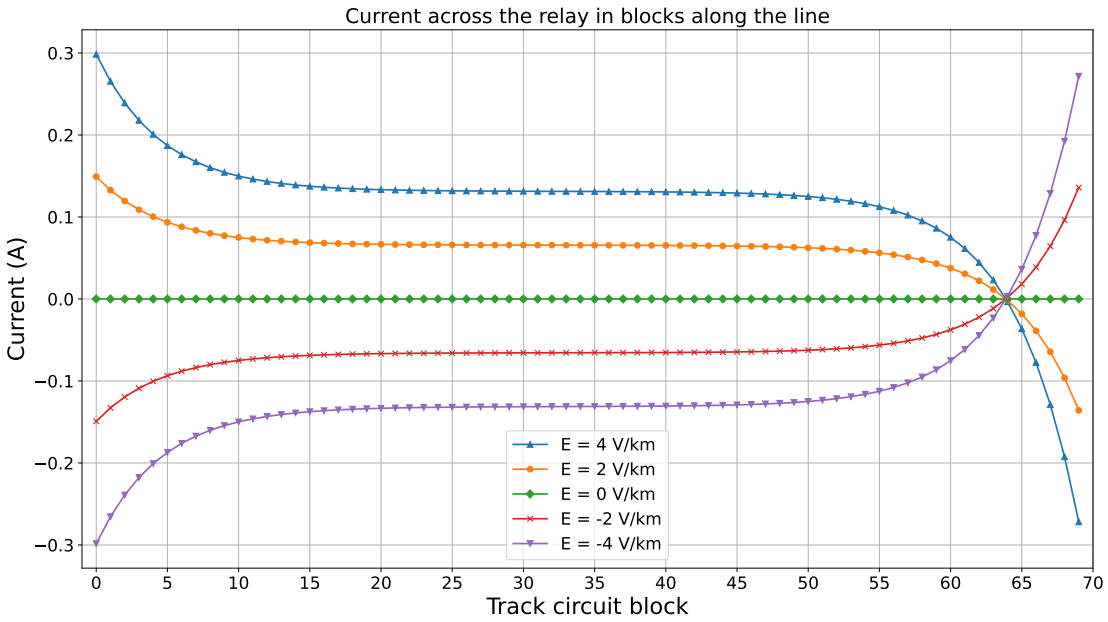

Figure 4.4: Parameters in a network of 70×1 km blocks facing directly westwards, where the track circuit voltage is set to zero: the current across the relays along the line for electric field strengths ranging from $4\,\mathrm{V\,km^{-1}}$ to $-4\,\mathrm{V\,km^{-1}}$. Independent of electric field strength, the currents cross zero at a common point.

as $[Y]$ is determined by the electrical characteristics of the rails and the track circuit components. $[J]$ is proportional to E and inversely proportional to the rail impedance. However, as the impedances of the signalling rails and traction rail are equal, changing E scales the currents induced in all rails by the same factor. As $[Y]^{-1}$ is constant and $[J]$ has been scaled by a certain factor, the result of the matrix multiplication is that $[V]$ would be scaled by the same factor. The current across the relays is determined by the relay resistance, which is constant, and the potential difference across the rail, which is the difference between two voltage nodes within $[V]$. This means that the potential difference is again scaled by that same factor. Consequently, when the potential difference is zero, scaling it by any factor would still result in zero, leading to a common crossover point that is independent of the electric field strength.

4.4.1.3 Susceptibility to Geomagnetic Interference

In this section, we investigate the factors which contribute to the susceptibility of a track circuit relay to induced currents. For the westwards direction of the Glasgow to Edinburgh line, the model was run for eastwards electric field values of 0 to $-4\,\mathrm{V\,km^{-1}}$ in increments of 0.1, recording the current across the relay in each block for every E-field value. The blocks were then sorted by length and the range of currents across each relay was plotted to determine if there was a dependence on block length. To examine the effects of the angle between a block's rails and the geoelectric field, a second set of modelled data was taken with the E-field in each block orientated along the rail. The results of this modelling are shown in Figure 4.5. Due to the effects of the ends of the traction rail on the voltage profiles, we split the blocks near the ends from those in the centre. When compared with blocks of similar length in the centre of the line, the range of current values across relays towards the ends of the line is larger near the start and smaller and oppositely directed near the termination. The angle between the E-field and the rails has a definite impact, the currents induced in the section will be largest when the E-field

is parallel to the rail and zero when the E-field is perpendicular to the rail. Most of the rails in blocks between Glasgow and Edinburgh are closely aligned with the direction of the E-field so the currents through most of the relays experience only minor variation, the exceptions we see are mainly due to the northwards orientation of the track near the Glasgow end of the line. If we consider only blocks at the centre of the line, the length of the blocks is a first-order indicator of the current through the relay. Considering the case when the E-field is aligned with the rails (shown by blue dashed lines in Figure 4.5), relay misoperations occur where the blocks are the longest. Other subtle effects can also be noted, i.e., the length of surrounding blocks, which affects the current across the relay of a block in between. This analysis was repeated for the southwards direction of travel of the Preston to Lancaster section of the WCML with a southwards electric field, there was no need to filter blocks near the ends due to it being a central segment of a longer line. The results, as shown in Figure 4.6, agree with those for the Glasgow to Edinburgh line, i.e., the longer blocks are more susceptible to geomagnetic interference than shorter ones.

4.4.2 Applying Electric Fields

4.4.2.1 Uniform Electric Fields

For the following analysis, each block is assumed to not be occupied by trains. This means, when not misoperating, signals should display a green light with the current flowing through the relay at a value above the relay dropout threshold.

Threshold Electric Field Strength to Cause Misoperations

Assuming the field is uniform across the entire area of the section, electric fields starting from strength 0 and increasing in intervals of $0.1\,\mathrm{V\,km^{-1}}$ were applied until the first "right side" failure occurred. For the "east-west" orientated Glasgow to Edinburgh line, the electric field was aligned to geographic east (E_y). For the "north-south" orientated Preston to Lancaster section, a geographic north direction (E_x)

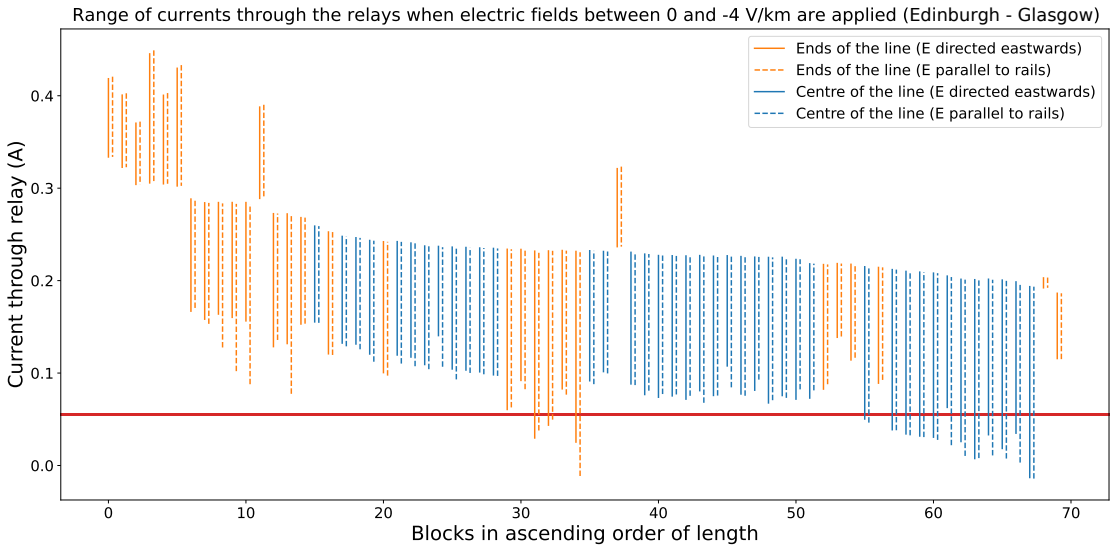

Figure 4.5: The range of currents across each relay in blocks along the westwards direction of the Glasgow to Edinburgh line for electric fields between 0 and $-4\,\mathrm{V\,km^{-1}}$. Solid lines show the results for when there is an angular separation between the rails and the electric field, and the dashed lines show the results for when the electric field is parallel to the rails in each block. Blocks at the centre of the rail are shown as blue lines and blocks at the ends as orange lines. The horizontal red line indicates the threshold below which the track circuit would de-energise.

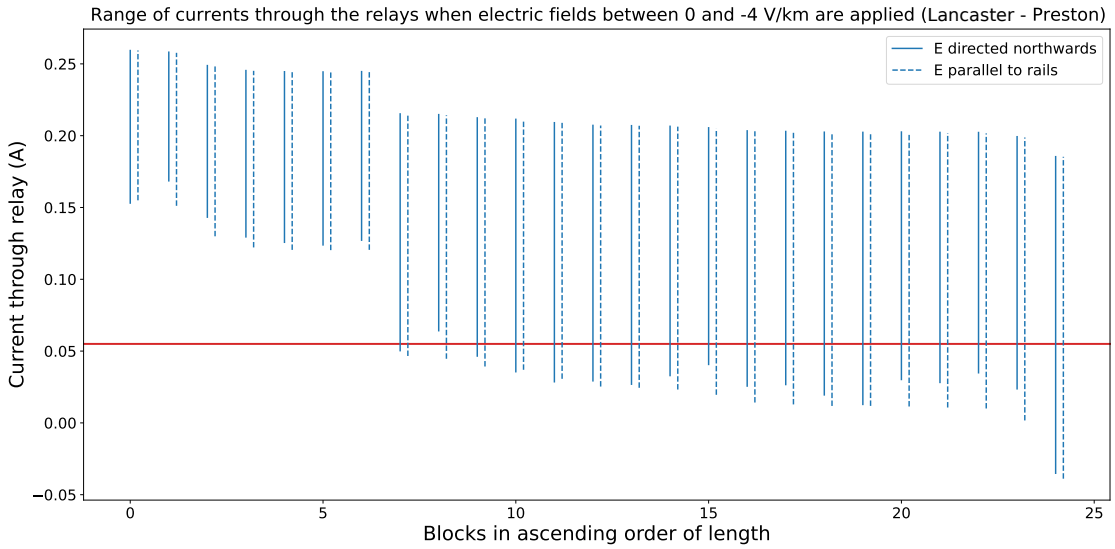

Figure 4.6: The range of currents across each relay in blocks along the southwards direction of the Preston to Lancaster section of the WCML for electric fields between 0 and $-4\,\mathrm{V\,km^{-1}}$. Solid lines show the results for when there is an angular separation between the rails and the electric field, and dashed lines show the results for when the electric field is parallel to the rails in each block. The horizontal red line indicates the threshold below which the track circuit would de-energise.

was chosen.

The current through the relay of each track circuit block along the Glasgow to Edinburgh line, assuming no external electric field is applied, is shown for the eastwards direction of travel in Figure 4.7(a) and the westwards direction of travel in Figure 4.7(b). For each point, a green outline with no fill indicates normal operation and black outline with red fill indicates a false signal. It can be seen that all relays are operating normally, with the differences in current arising from network design factors such as the length of blocks. The threshold electric field value at which signal misoperations begin to occur along the Glasgow to Edinburgh line is $E_y = 1.9\,\mathrm{V\,km^{-1}}$ for the eastwards direction of travel, shown in Figure 4.7(c), and $E_y = -2.8\,\mathrm{V\,km^{-1}}$ for the westwards direction of travel, shown in Figure 4.7(d).

The threshold electric field values required to cause a "right side" failures in blocks along both directions of the Glasgow to Edinburgh line are shown in Figure 4.8. In some cases, .i.e., block 9 in the eastwards direction of travel and block 61 in the westwards direction of travel, there is not misoperation value for moderate conditions due to those blocks being at the crossover point. However, when the leakage changes with environmental conditions, so does the position of the crossover point, which is why there is a threshold value at that block for wet and dry conditions. There are also some cases, e.g., around the left end of the line in the eastwards direction of travel and around the right end of the line in the westwards direction, where only the threshold value for wet conditions are shown, as the electric field needed to cause misoperation in dry conditions was outside the $\pm 30\,\mathrm{V\,km^{-1}}$ range used in this analysis. Finally, for some blocks, e.g., block 12 in the eastward direction of travel and block 60 in the westward direction of travel, the threshold value for moderate conditions can be higher or lower than for wet and dry conditions, which is also due to the shifting of the crossover point.

Assuming moderate environmental conditions, from Figure 4.8, the total number of "right side" failures that would occur in blocks along the Glasgow to Edinburgh line over a range of electric field strengths can be determined, as shown in Figure 4.9.

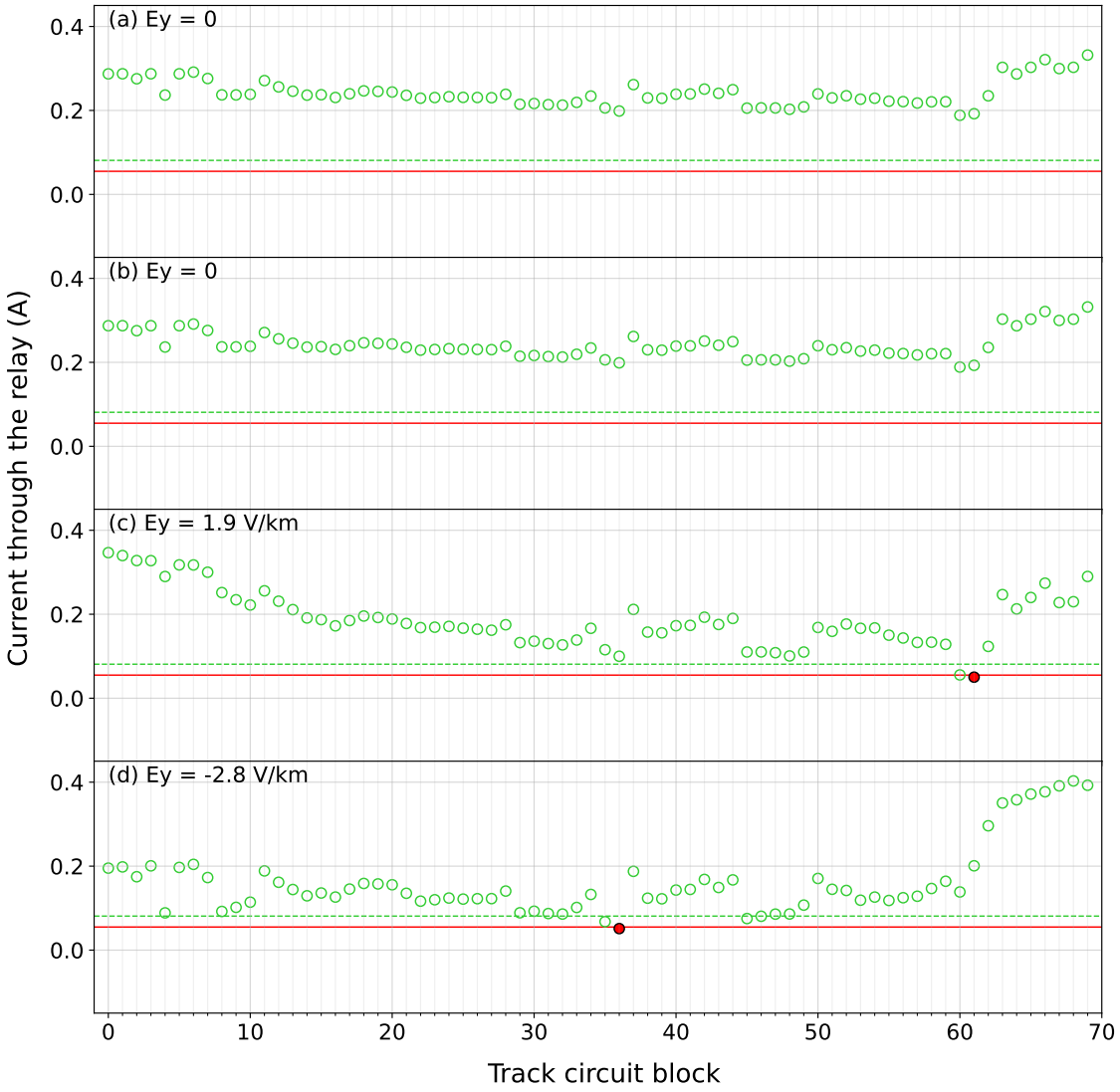

Figure 4.7: In the absence of any trains, with no external electric field applied for the (a) eastward and (b) westward directions of travel, and at the threshold electric field value required for misoperations to occur in the (c) eastward and (d) westward directions of travel: the current through the 70 track circuit relays between Glasgow and Edinburgh. An unfilled green circle means normal operation and a black circle filled red indicates a misoperation. The red (solid) line shows the threshold below which the track circuit would de-energise and display an incorrect signal, and the green (dashed) line shows the threshold the current would need to rise above to re-energise if de-energised.

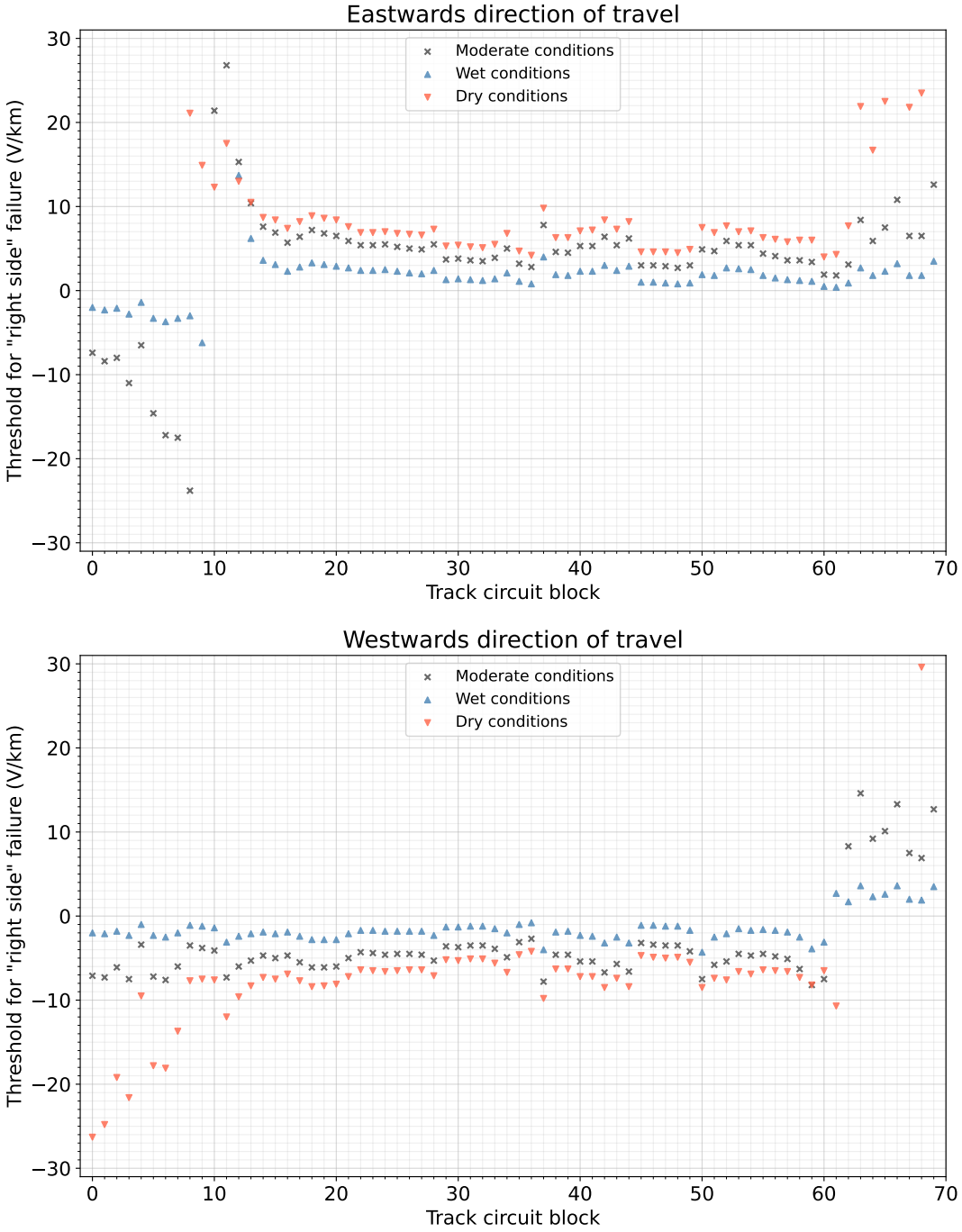

Figure 4.8: Glasgow to Edinburgh: The threshold eastward electric field values to cause "right side" failure for each track circuit block in both eastward and westward directions of travel during moderate, wet and dry environmental conditions. In both directions of travel, Glasgow is on the left and Edinburgh on the right.

For the eastwards direction of travel, the blocks that misoperate when the electric field strength is negative are beyond the crossover point, near the end of the line relative to the direction of travel.

For the Preston to Lancaster section of the WCML, the current through the relay of each track circuit block, assuming no external electric field is applied, is shown for the northwards direction of travel in Figure 4.10(a) and the southwards direction of travel in Figure 4.10(b). The threshold electric field value at which signal misoperations begin to occur is $E_x = 2.7\,\mathrm{V\,km^{-1}}$ for the the northwards direction of travel, shown in Figure 4.10(c), and $E_x = -2.5\,\mathrm{V\,km^{-1}}$ for the southwards direction of travel, shown in Figure 4.10(d).

The threshold electric field values required to cause a "right side" failures in blocks along both directions of the Preston to Lancaster section of the WCML are shown in Figure 4.11. In this case, the crossover point does not impact these results due to this route being in the middle of a longer line.

Assuming moderate environmental conditions, from Figure 4.11, the total number of "right side" failures that would occur on the Preston to Lancaster section of the WCML over a range of electric field strengths can be determined, as shown in Figure 4.12.

Electric Field Strength that has Caused Misoperation in the Past

Electric fields of strength $\pm 4\,\mathrm{V\,km^{-1}}$ have been applied to each route, based on the lower limit of geoelectric field values observed in Sweden during the storm of July 1982, where interference on railway signalling was observed (Wik et al., 2009).

Along the Glasgow to Edinburgh line, at $E_y = 4\,\mathrm{V\,km^{-1}}$, the currents induced in the track circuits are sufficiently strong to cause 18 misoperations in the eastwards direction of travel, as seen in Figure 4.13(a), and no misoperations in the westwards direction of travel, shown in Figure 4.13(b). At $E_y = -4\,\mathrm{V\,km^{-1}}$, the situation is reversed, with no misoperations in the eastward direction of travel, shown in Figure 4.13(c), and 14 misoperations in the westward direction of travel. With the Glasgow

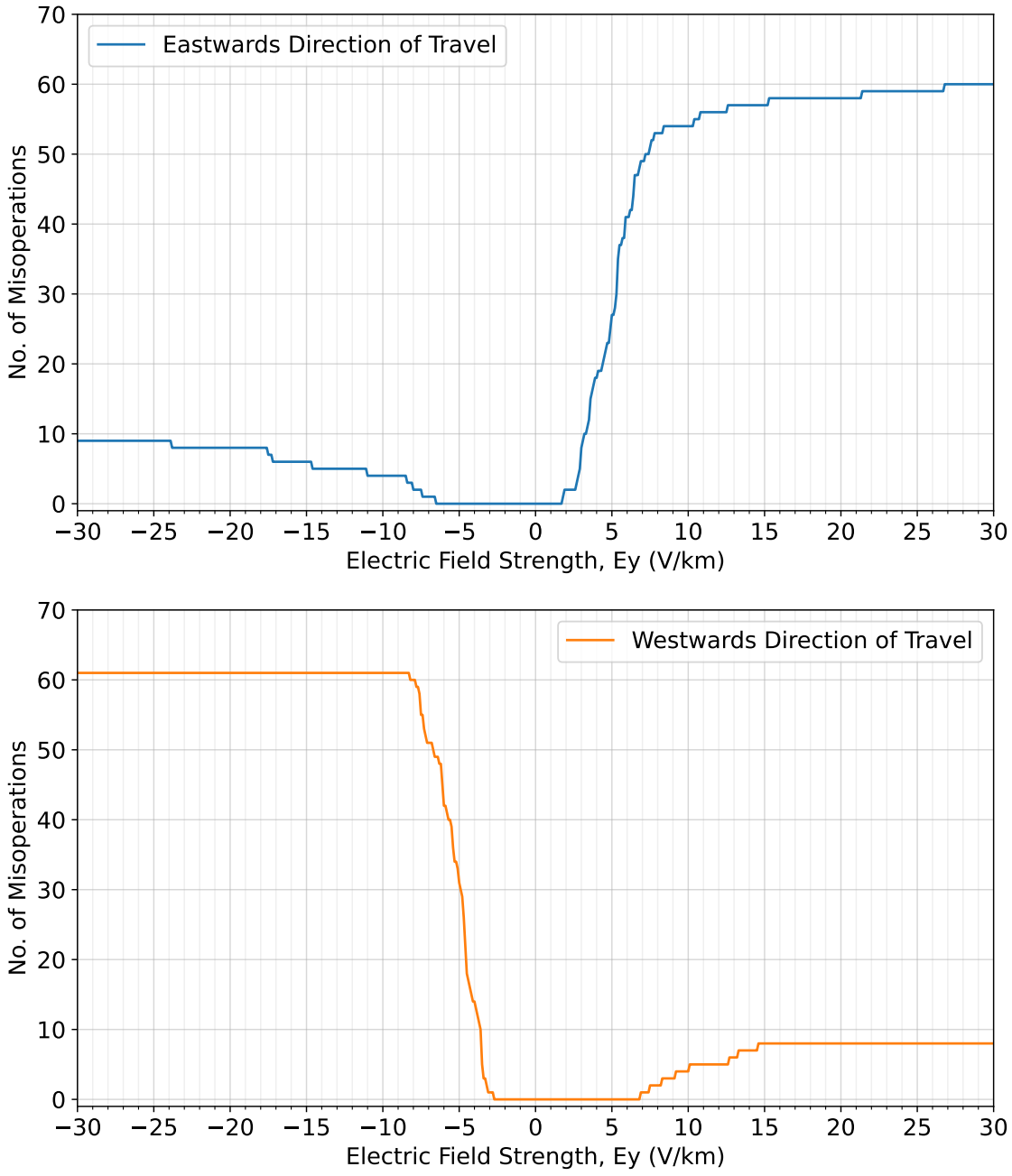

Figure 4.9: Glasgow to Edinburgh: The number of track circuit blocks with the potential to experience "right side" failures at different magnitudes of electric field strength for both the eastwards and westwards directions of travel.

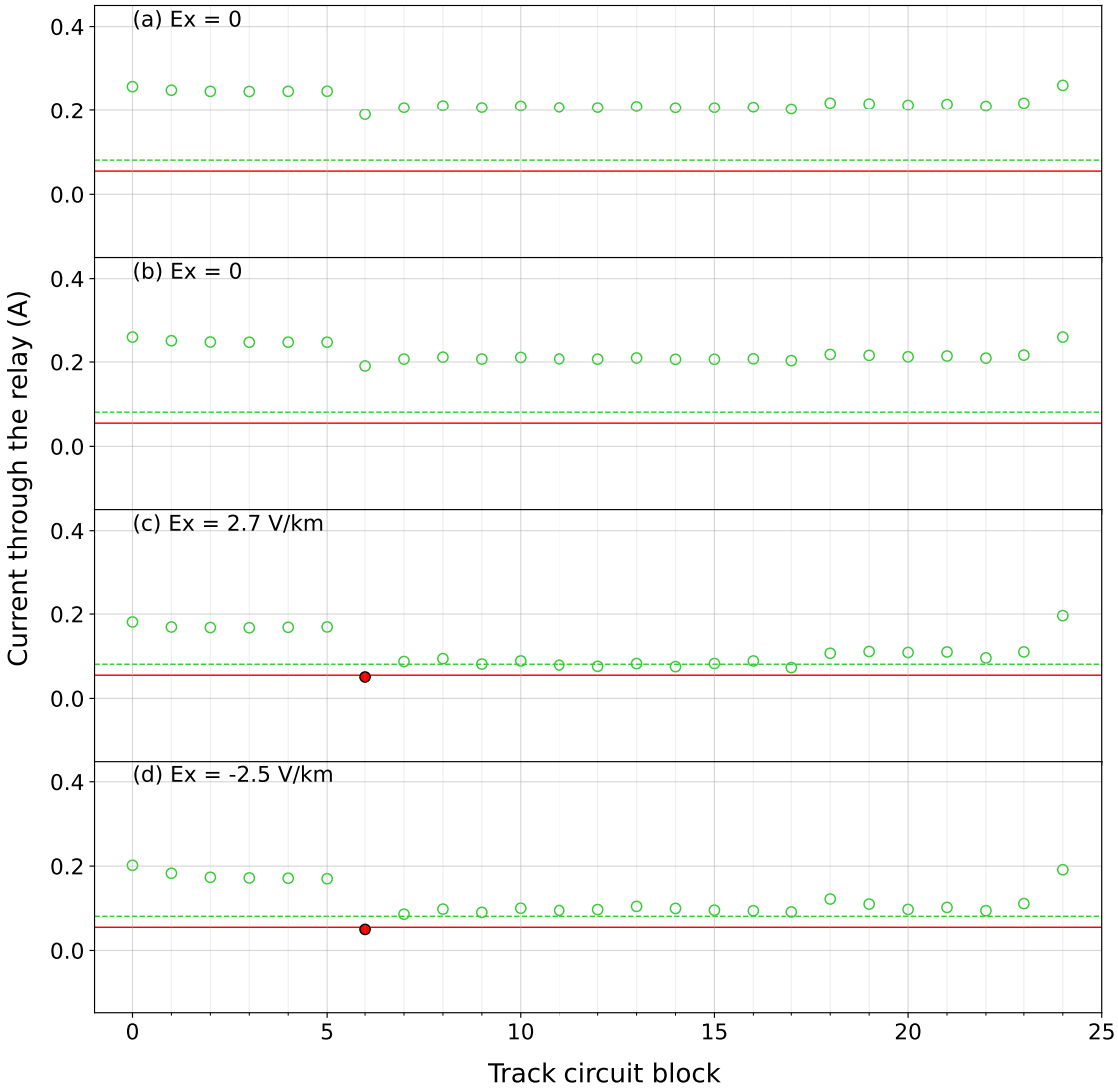

Figure 4.10: In the absence of any trains, with no external electric field applied for the (a) northward and (b) southward directions of travel, and at the threshold electric field value required for misoperations to occur in the (c) northward and (d) southward directions of travel: the current through the 25 track circuit relays between Preston and Lancaster. An unfilled green circle means normal operation and a black circle filled red indicates a misoperation. The red (solid) line shows the threshold below which the track circuit would de-energise and display an incorrect signal, and the green (dashed) line shows the threshold the current would need to rise above to re-energise if de-energised.

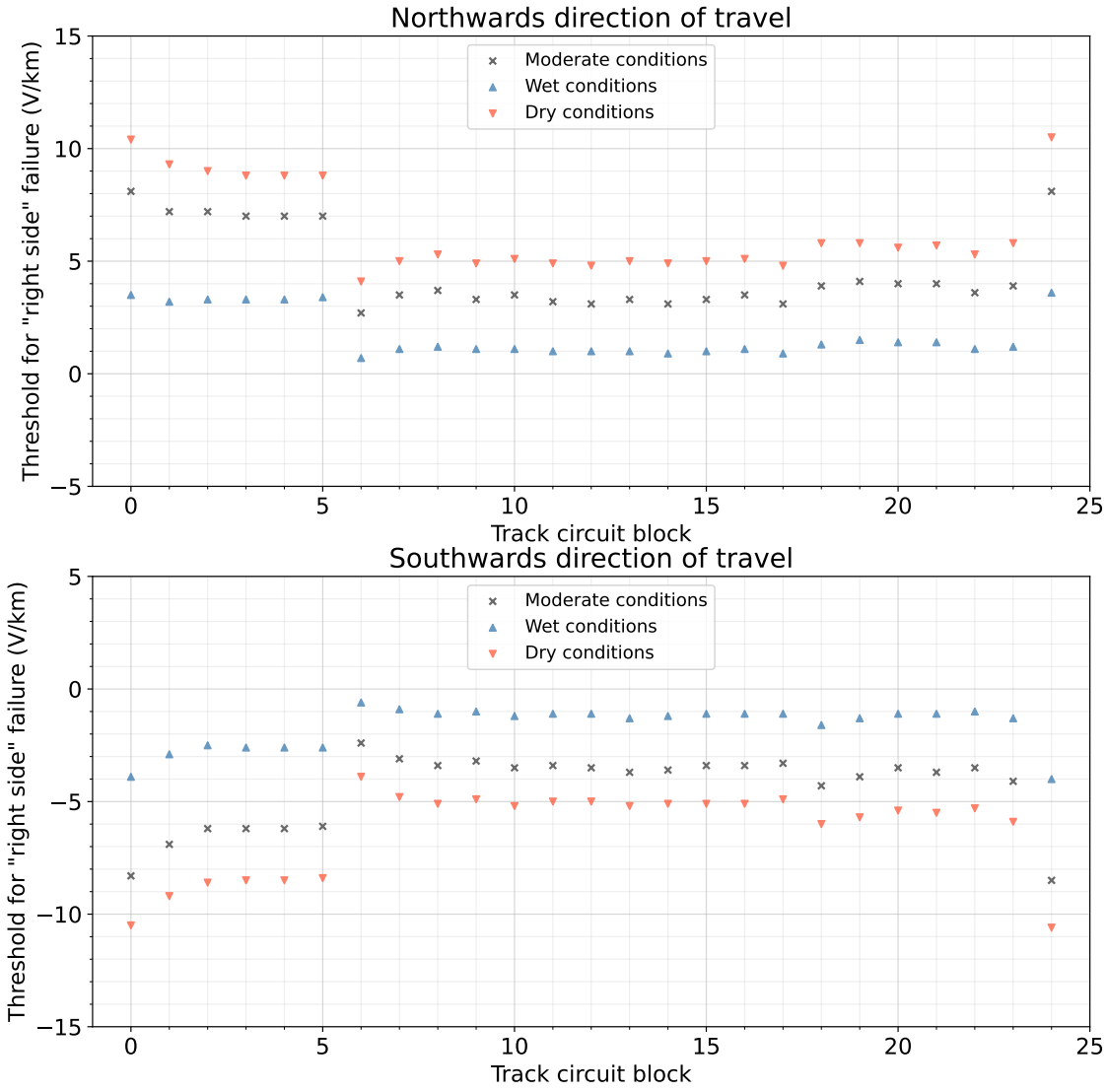

Figure 4.11: Preston to Lancaster: The threshold northwards electric field values to cause "right side" failure for each track circuit block in both northwards and southwards directions of travel during moderate, wet and dry environmental conditions. In both directions of travel, Preston is on the left and Lancaster on the right.

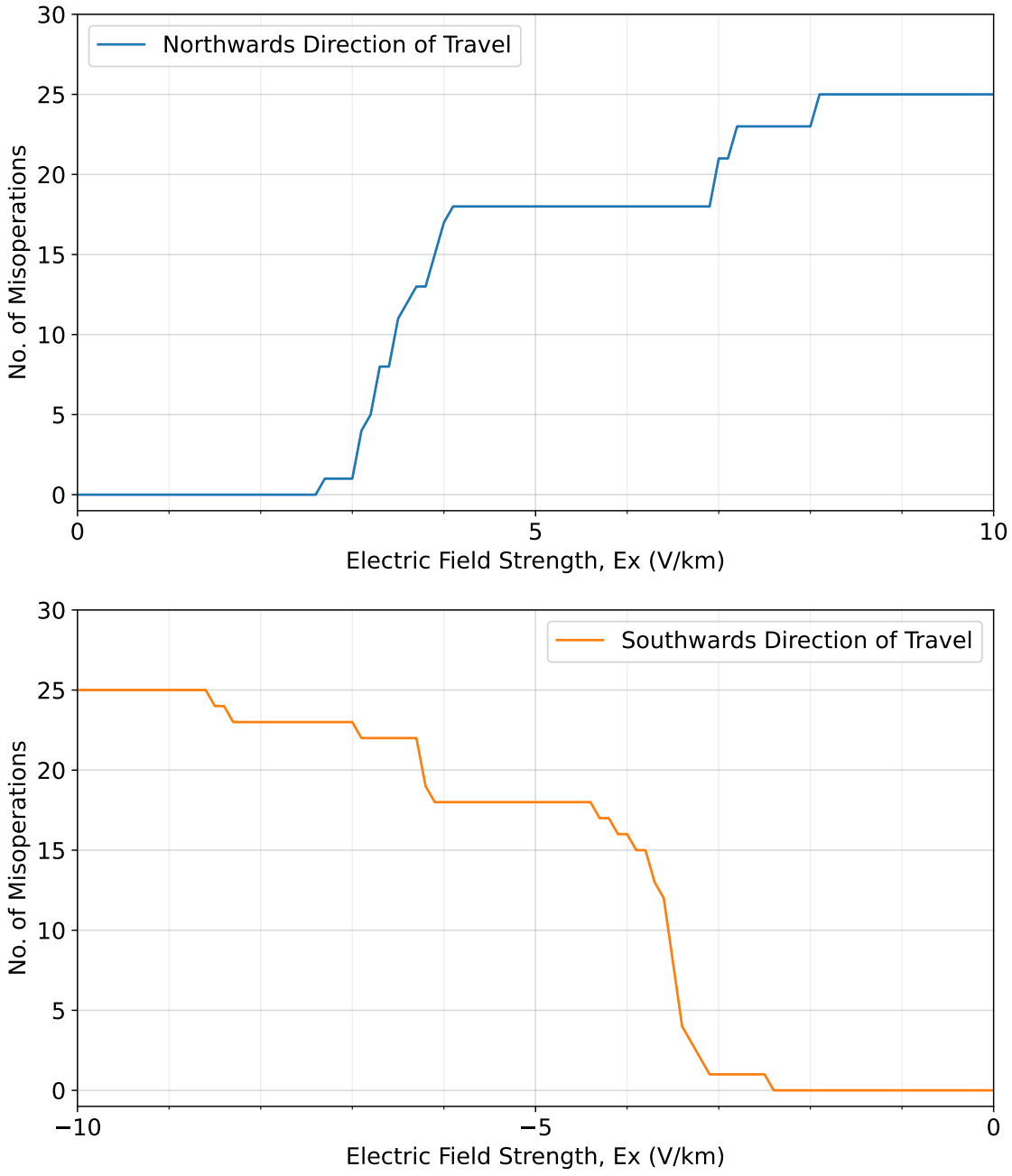

Figure 4.12: Preston to Lancaster: The number of track circuit blocks with the potential to experience "right side" failures at different magnitudes of electric field strength for both the northwards and southwards directions of travel.

to Edinburgh line, as we are modelling the entire line, it is important to consider the case of positive and negative electric fields for both directions of travel due to the reversed potential difference beyond the crossover point. At $E_y = 4\,\mathrm{V\,km^{-1}}$, the de-energisation of the blocks beyond the crossover can be seen in Figure 4.13(b) when compared with the profiles of the negative electric fields, as in Figure 4.13(d). However, no signal misoperations occur due to the shorter length of the blocks near that end of the line.

The same analysis was performed on the Preston to Lancaster section of the WCML. At $E_x = 4\,\mathrm{V\,km^{-1}}$, there are 14 misoperations in the northwards direction of travel, as seen in Figure 4.14(a), and no misoperations in the southwards direction of travel, as shown in Figure 4.14(b). For $E_x = -4\,\mathrm{V\,km^{-1}}$, there are no misoperations in the northwards direction of travel, as seen in Figure 4.14(c), and 17 misoperations in the southwards direction of travel, as shown in Figure 4.14(d).

4.4.2.2 1-in-100 Year Extreme

An estimate for a 1-in-100 year extreme geoelectric field for the UK is estimated by Beggan et al. (2013) to be approximately $5\,\mathrm{V\,km^{-1}}$. The currents across the relays for the Glasgow to Edinburgh line and the Preston to Lancaster section of the WCML are shown in Figures 4.15 and 4.16 respectively. For the Glasgow to Edinburgh line, we see a third of blocks in the eastwards direction of travel misoperating at $5\,\mathrm{V\,km^{-1}}$, and almost half of the blocks in the westwards direction misoperating at $-5\,\mathrm{V\,km^{-1}}$. For the Preston to Lancaster section of the WCML, at $5\,\mathrm{V\,km^{-1}}$ and $-5\,\mathrm{V\,km^{-1}}$, almost all of the blocks are misoperating in the northwards and southwards directions of travel respectively. This suggests that a 1-in-100 year extreme event would result in significant signal misoperations on both routes.

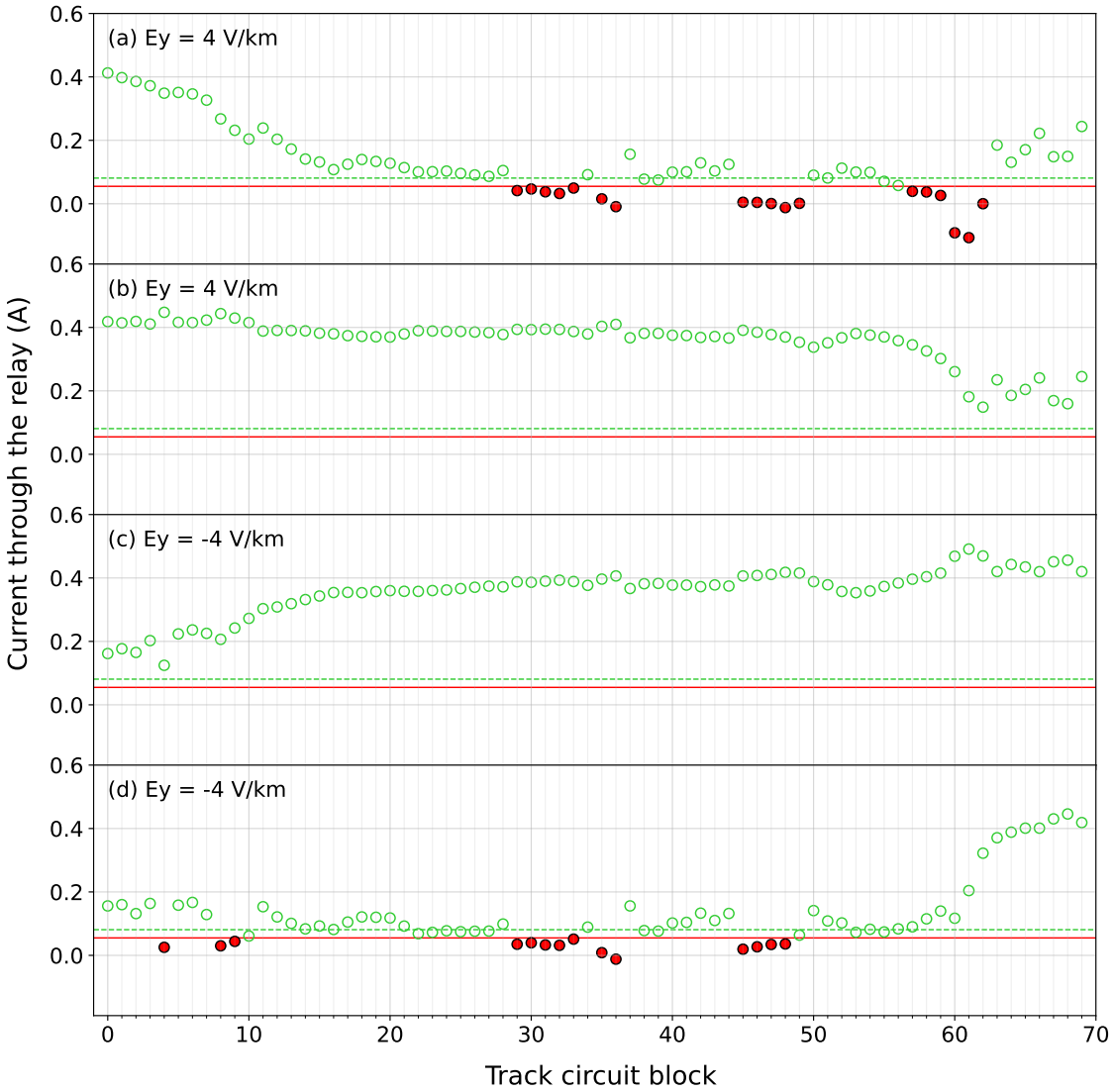

Figure 4.13: In the absence of any trains, at $E_y = 4\,\mathrm{V\,km^{-1}}$ for the (a) eastward and (b) westward directions of travel, and at $E_y = -4\,\mathrm{V\,km^{-1}}$ for the (c) eastward and (d) westward directions of travel: the current through the 70 track circuit relays between Glasgow and Edinburgh. An unfilled green circle means normal operation and a black circle filled red indicates a misoperation. The red (solid) line shows the threshold below which the track circuit would de-energise and display an incorrect signal, and the green (dashed) line shows the threshold the current would need to rise above to re-energise if de-energised.

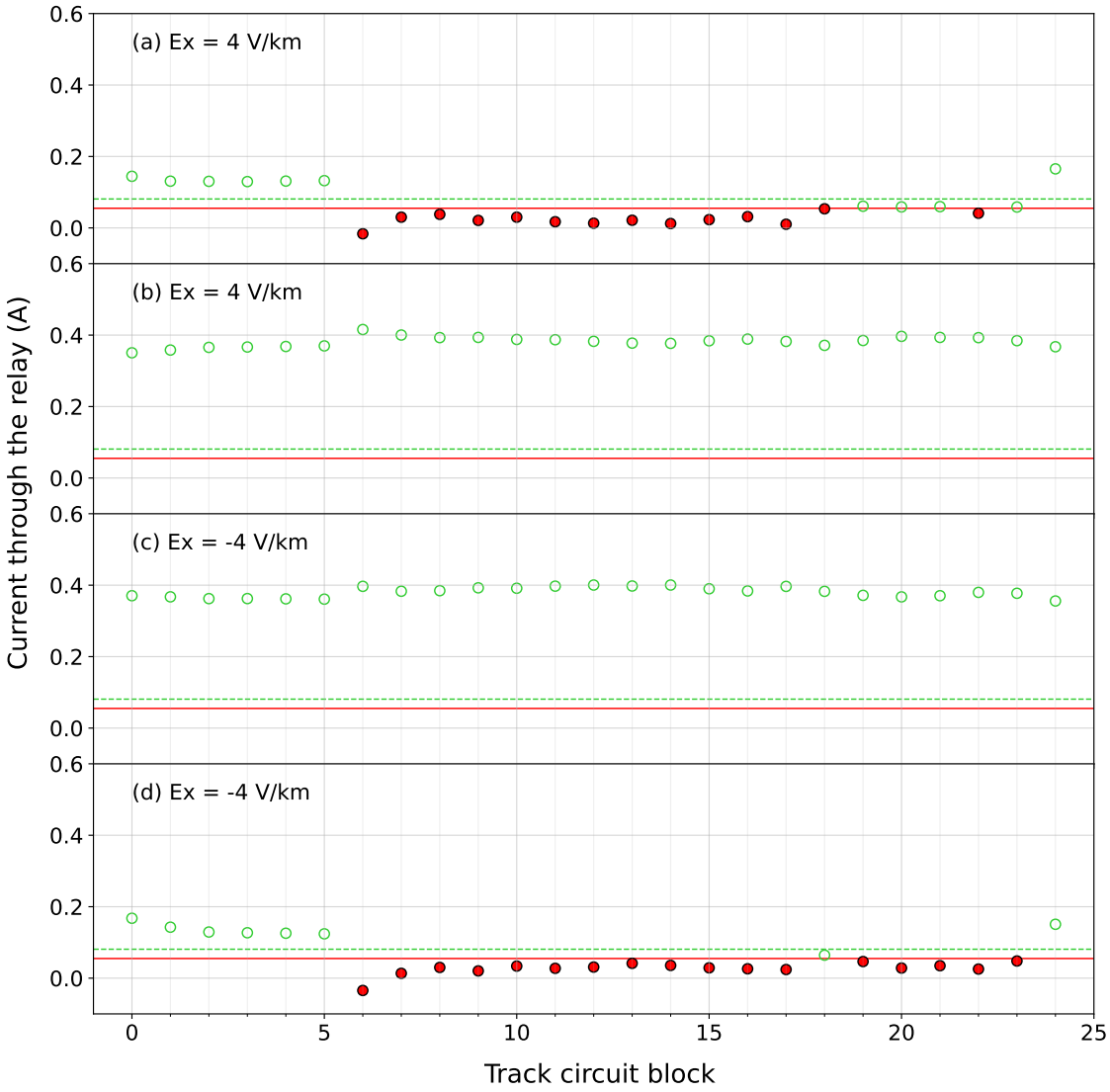

Figure 4.14: In the absence of any trains, at $E_x = 4\,\mathrm{V\,km^{-1}}$ for the (a) northward and (b) southward directions of travel, and at $E_x = -4\,\mathrm{V\,km^{-1}}$ for the (c) northward and (d) southward directions of travel: the current through the 25 track circuit relays between Preston and Lancaster. An unfilled green circle means normal operation and a black circle filled red indicates a misoperation. The red (solid) line shows the threshold below which the track circuit would de-energise and display an incorrect signal, and the green (dashed) line shows the threshold the current would need to rise above to re-energise if de-energised.

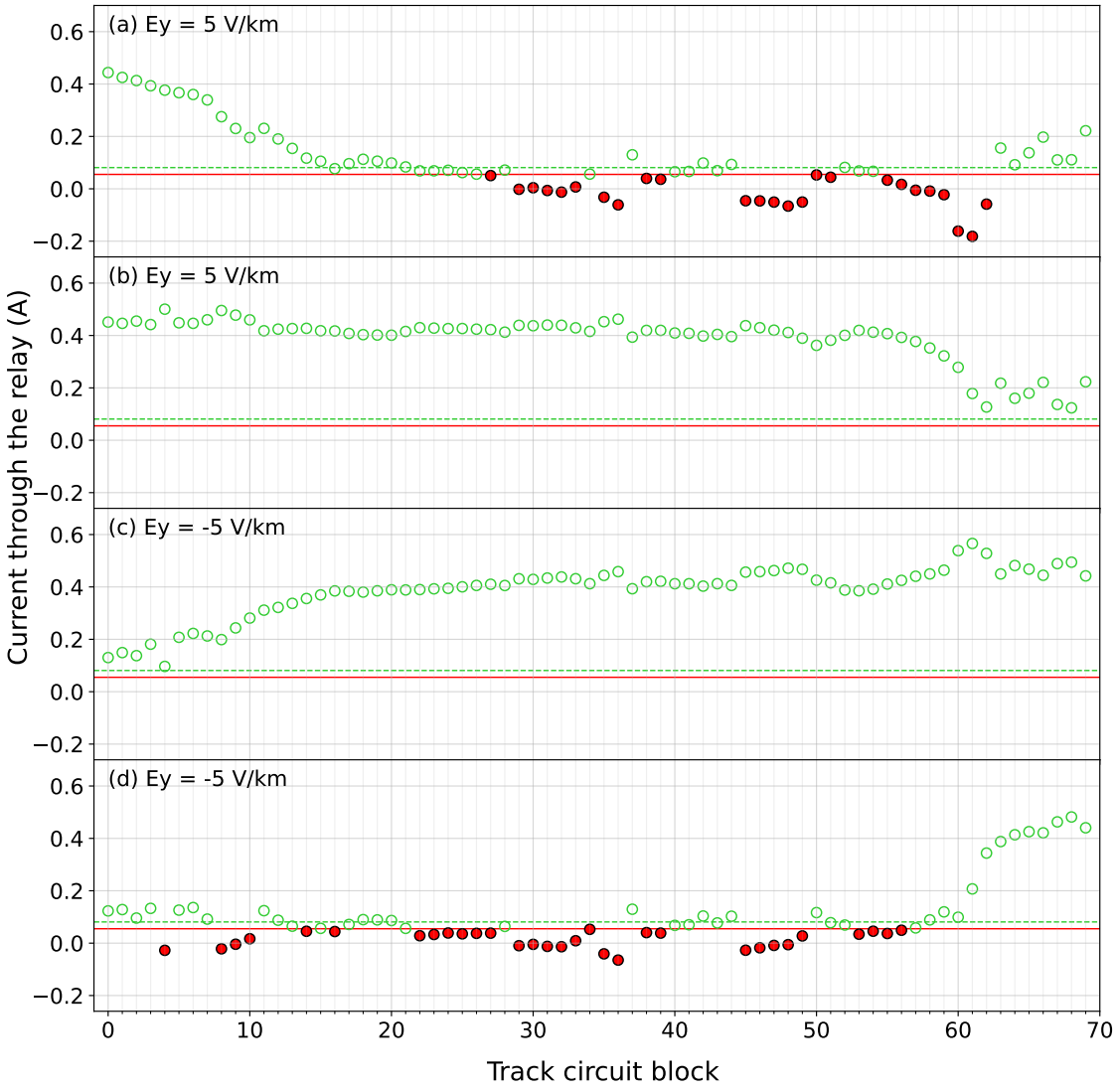

Figure 4.15: In the absence of any trains, at $E_y = 5\,\mathrm{V\,km^{-1}}$ for the (a) eastward and (b) westward directions of travel, and at $E_y = -5\,\mathrm{V\,km^{-1}}$ for the (c) eastward and (d) westward directions of travel: the current through the 70 track circuit relays between Glasgow and Edinburgh. An unfilled green circle means normal operation and a black circle filled red indicates a misoperation. The red (solid) line shows the threshold below which the track circuit would de-energise and display an incorrect signal, and the green (dashed) line shows the threshold the current would need to rise above to re-energise if de-energised.

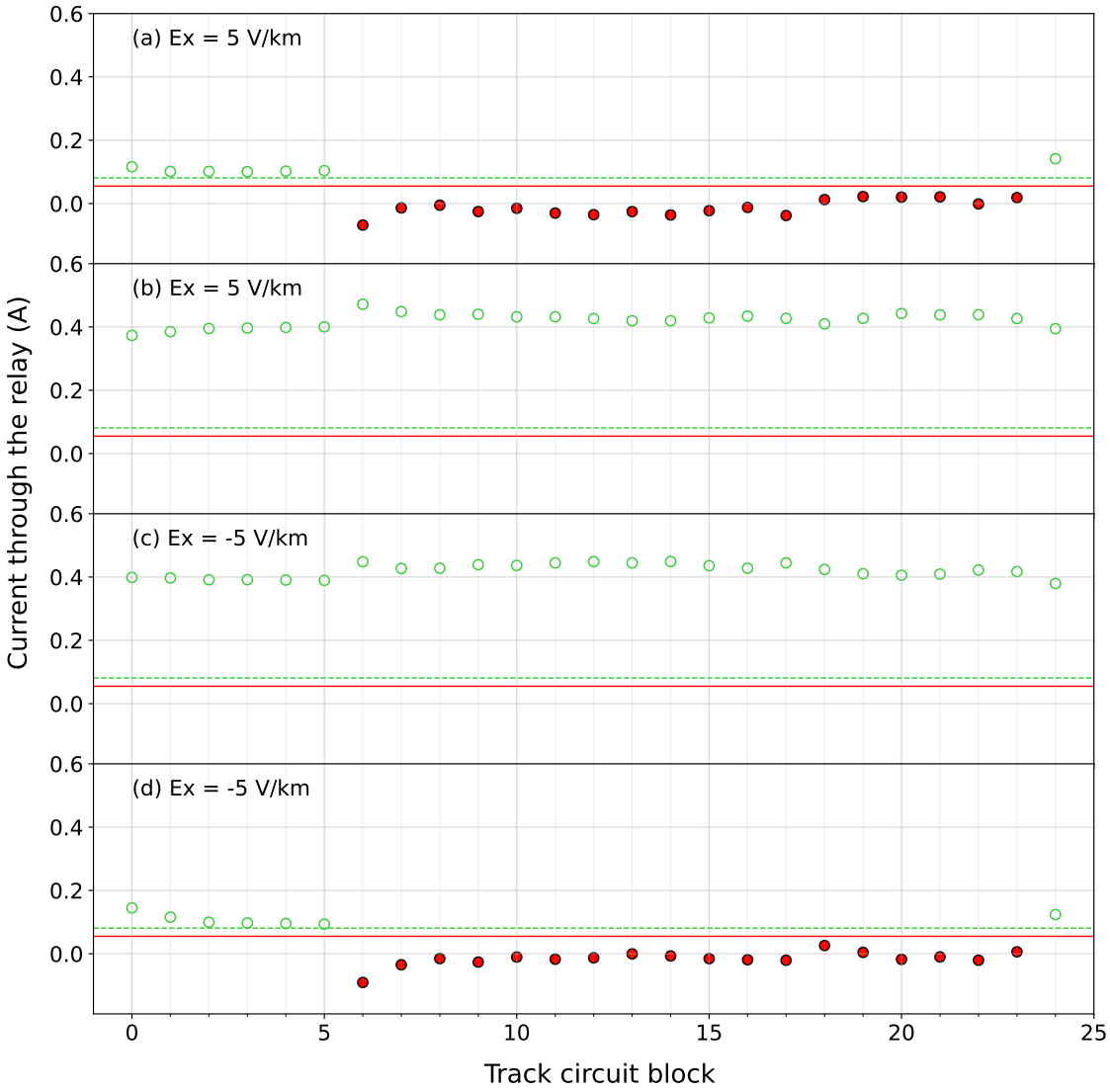

Figure 4.16: In the absence of any trains, at $E_x = 5\,\mathrm{V\,km^{-1}}$ for the (a) northward and (b) southward directions of travel, and at $E_x = -5\,\mathrm{V\,km^{-1}}$ for the (c) northward and (d) southward directions of travel: the current through the 25 track circuit relays between Preston and Lancaster. An unfilled green circle means normal operation and a black circle filled red indicates a misoperation. The red (solid) line shows the threshold below which the track circuit would de-energise and display an incorrect signal, and the green (dashed) line shows the threshold the current would need to rise above to re-energise if de-energised.

4.5 Discussion

This study expands upon the theoretical work of Alm (2020), Lejdström and Svensson (2020) and Boteler (2021) by modelling realistic railway lines with parameters from current industrial standards. The electrical characteristics and parameters for the rails and track circuit components are specific to the UK 25 kV, 50 Hz AC railway lines, e.g., the WCML and the Glasgow to Edinburgh line. These values can be replaced as necessary which allow the modelling to be used for any combination of rails, blocks and relay types, provided the data for those components are available. The main reason we chose a section of the WCML was because it is one of the UK's most important railway lines. It provides rail links to major cities, including an arterial connection between England and Scotland. With a pre-pandemic estimate of 35 million passengers annually (Department for Transport, 2015), the WCML provides crucial services including local and regional travel as well as freight. The Glasgow to Edinburgh line was chosen for its east-west orientation and due to it being a connection between two major cities.

The model showed that the potential difference across track circuit relays near to the ends of the line can vary greatly from those in the centre even if they have identical properties and parameters. This means that the susceptibility of a track circuit block to induced currents cannot simply be determined from its length and orientation (i.e., alignment to the direction of the electric field). However, we have also shown that those assumptions are valid when studying sections of a longer line that are not near the ends of the traction rail.

Comparing the electric field values at which signal misoperations begin to occur with estimates of electric fields across the UK for different timescales by Beggan et al. (2013), the value is equivalent to an event that could occur once about every 30 years. Electric fields in the UK estimated for a 1-in-100 year extreme geomagnetic field by Beggan et al. (2013) were demonstrated to cause significant disruptions to the two lines studied, with a large number of signal misoperations occurring.

While the electrical characteristics of the rails used in most of the examples

in this study are the conventional values given in Network Rail standards, the variation in leakage from the rails to the ground was shown to cause changes in the threshold electric field strength needed to cause "right side" failures. The misoperation threshold values for different environmental conditions were obtained using the range of leakage from the rails to the ground from Network Rail standard NR/GN/ELP/27312 (2006), and the results are as follows. It was found that when the leakage to the ground was maximised ($0.4\,\mathrm{S\,km^{-1}}$ for the signalling rail and $2\,\mathrm{S\,km^{-1}}$ for the traction rail), the threshold electric field values at which signal misoperations begin to occur was lowered to $0.4\,\mathrm{V\,km^{-1}}$ in the eastwards direction of travel and $-0.8\,\mathrm{V\,km^{-1}}$ in the westwards direction of travel for the Glasgow to Edinburgh line, and lowered to $0.7\,\mathrm{V\,km^{-1}}$ in the northwards direction of travel and $-0.6\,\mathrm{V\,km^{-1}}$ in the southwards direction of travel for the Preston to Lancaster section of the WCML. When the leakage to the ground was minimised ($0.025\,\mathrm{S\,km^{-1}}$ for the signalling rail and $1.53\,\mathrm{S\,km^{-1}}$ for the traction rail), the threshold electric field values at which signal misoperations begin to occur was raised to $4\,\mathrm{V\,km^{-1}}$ in the eastwards direction of travel and $-4.2\,\mathrm{V\,km^{-1}}$ in the westwards direction of travel for the Glasgow to Edinburgh line, and lowered to $4.1\,\mathrm{V\,km^{-1}}$ in the northwards direction of travel and $-3.9\,\mathrm{V\,km^{-1}}$ in the southwards direction of travel for the Preston to Lancaster section of the WCML. This means we are more likely to see signal misoperations on days that are wetter than average and vice versa. The impact of altering the rail resistance was also analysed, but it was found that varying either or both of the rail's resistance values did not result in a significant change to the results.

It was shown that signal misoperations only occur when the applied electric field was along the direction of travel. This is due to the field being orientated such that the induced currents mostly contributed towards de-energising the relays, flowing across the relay in a direction opposite to the current provided by the track circuit power supply. When the electric field was orientated opposite to the direction of travel, most of the relays became more energised. However, if the model includes

the entirety of the traction rail, the currents across the relays in blocks near a characteristic crossover point become less sensitive to the changes in the electric field. Also, in blocks beyond the crossover point, the direction of current across the relays will be reversed. In these blocks, if the electric field is orientated opposite to the direction of travel, they become increasingly de-energised as the strength of the field increases.

In this chapter, we have focused on geoelectric fields of constant direction and magnitude, when in reality they typically vary in intensity and direction over time. The impact of time-varying fields will be considered in future chapters.

The impact of space weather on railway signalling is but one aspect of a multifaceted system that is intrinsically connected. Alongside signalling systems, the operation of a railway network also relies upon many interdependent systems such as power transmission, communication and GNSS, all of which are susceptible to the effects of space weather (Hapgood et al., 2021). The UK report on rail resilience to space weather Darch et al. (2014) states: "Accidents are rarely caused by a single failure; compound effects from multiple impacts are likely to create a problem" (p.5). Considering the delays that the railway network could be subjected to in the case of extensive signalling misoperations, passengers could potentially be trapped on a stationary train for extended periods. This is especially likely if other interdependent systems are also affected. The onboard air-conditioning and toilet systems are unable to continue operating for long periods without external power sources, subjecting passengers to uncomfortable and potentially harmful conditions. In this eventuality, if passengers were to take it upon themselves to leave the train unaided, then they would be subjected to severe risk due to currents flowing in the rails, trains on adjacent lines and a plethora of other hazards from walking unattended along a potentially remote section of track.

4.6 Conclusion

This study presents the most realistic model of geomagnetic interference in DC signalling systems on AC-electrified railway lines to date. Built upon the techniques detailed in Boteler (2021) we have modelled two sections of the UK railway network, the north-south orientated Preston to Lancaster section of the WCML and the east-west orientated Glasgow to Edinburgh via Falkirk line.

Comparing these two sections, the model showed that the extent to which induced currents can affect track circuit relays depends heavily on whether the section studied includes the ends of the traction rail or whether it is part of a longer line. When considering the impact on relays in the centre of a line it can be seen that block length is a first-order indicator of current across the relays. The angular difference between the rail orientation and the electric field direction is also a factor, with blocks aligned parallel to the electric field having the largest currents induced along them. There are also further subtle effects such as the lengths of blocks adjacent to a given track circuit block which can affect the overall voltage profile.

Uniform electric fields were applied to the track sections in our model to find the threshold electric field that would generate sufficiently strong GICs to cause relay de-energisation of signalling relays in the Glasgow to Edinburgh line and the Preston to Lancaster section of the WCML. For the Glasgow to Edinburgh line, the threshold values were $E_y = 1.9\,\mathrm{V\,km^{-1}}$ for the eastwards direction of travel, and $E_y = -2.8\,\mathrm{V\,km^{-1}}$ for the westwards direction of travel. For the Preston to Lancaster section of the WCML, the threshold values were $E_x = 2.7\,\mathrm{V\,km^{-1}}$ for the the northwards direction of travel, and $E_x = -2.5\,\mathrm{V\,km^{-1}}$ for the southwards direction of travel. These values are equivalent to those generated by events that could occur approximately once every 30 years.

When the electric field was strengthened to $\pm 4\,\mathrm{V\,km^{-1}}$ (a geoelectric field value known to have impacted railway signalling in Sweden during the storm of July 1982), many misoperations were shown to occur on both lines.

Applying a 1-in-100 year extreme geoelectric field, estimated to be $\pm 5\,\mathrm{V\,km^{-1}}$,

the GICs generated were strong enough to affect many of the signals along both routes, leading to significant operational impacts.

Chapter 5

"Wrong side" Failures

The following chapter contains published work from the article:
Patterson, C. J., Wild, J. A., & Boteler, D. H. (2023b). Modeling "wrong side" failures caused by geomagnetically induced currents in electrified railway signaling systems in the UK. *Space Weather*, *21*(12), e2023SW003625. https://doi.org/10.1029/2023SW003625

This chapter extends the modelling presented in Chapter 4 which explored the impact of geomagnetic effects on DC signalling for AC-electrified railways in the UK, focusing on "right side" failures in which green signals are turned to red. The extended model reported here allows the study of "wrong side" failures where red signals are turned green: a failure mode that is potentially more dangerous. This chapter shows that a relay is most susceptible to "wrong side" failure when a train is at the end of a track circuit block. Assuming that each train is positioned at the end of the block it is occupying, the results show that the geoelectric field threshold at which "wrong side" failures can begin to occur is lower than for "right side" failures. A geomagnetic storm of this magnitude occurs on a timescale of once every 10 or 20 years. It is also shown that the estimated peak geoelectric field during a 1-in-100 year event could cause a significant number of "wrong side" failures at multiple points along the railway lines studied, although this depends on the number of trains on the line at that time.

5.1 Introduction

Chapter 4 details how DC track circuit signalling systems on AC electrified railways in the United Kingdom are impacted by GICs, as given in Patterson et al. (2023a). The chapter focused on the simplest case of misoperation, known as "right side" failures, which have the potential to cause disruption, but are not hazardous. The analysis involved building a network model of two UK railway lines (see Section 4.4.1) and applying varying levels of uniform geoelectric field to identify the thresholds for "right side" failure. The study concluded that the return period for an event strong enough to cause "right side" failures would be about once every 30 years, and that a 1-in-100 year event would cause a significant number of misoperations across both lines. In this chapter, we extend the work described above to focus on the potentially hazardous failure mode, known as "wrong side" failures.

Section 5.2 expands on the operational principles of track circuit signalling in Section 4.2, and describes how "wrong side" failures may occur. Section 5.3 details the modifications made to the model to produce this newest iteration. In Section 5.4, we provide the results of the modelling. In 5.4.1 and 5.4.2, we show the effects of the additions to the model (cross bonds and train axles, respectively) and how they may impact the results; 5.4.3 gives the threshold electric field strength for "wrong side" failures in each block, and 5.4.4 discusses how those thresholds differ with changes to the leakage to the ground due to weather conditions. Section 5.4.5 shows examples of the resultant currents through the relays at a range of electric field values from the misoperation threshold to a 1-in-100 year extreme assuming a number of trains spaced along the line.

5.2 Track Circuit Signalling

Railway technologies and infrastructures are constantly evolving. In the UK, Network Rail's Digital Railway initiative aims to reduce the reliance on track-side signals. For high-capacity intercity lines there is a push to introduce radio-based

European Train Control System technology. These newer technologies, and the widespread use of axle counters, may reduce the susceptibility of future signalling systems to GICs and are being rolled out progressively on existing UK main lines. However, this technology is unlikely to be deployed on all lines due to cost and probably not even the majority of lines. Since typical railway infrastructure has a lifetime of 30-40 years, rolling technology upgrades also occur over long timescales. Meanwhile, DC track circuits (of the kind modelled in this study) are relatively cheap and there are thousands installed in the UK network that will remain in use for decades to come (Knight-Percival et al., 2020).

As the speed of trains has increased over time, the basic, two-aspect, red/green signals have been substituted, where needed, by three-aspect or four-aspect signalling, which give drivers advanced notice of the signal state in the next three or four blocks. This allows them to have sufficient time to safely reduce their speed as they approach a red signal. The state of the yellow signals in three-aspect and four-aspect signalling is determined by the logic of the occupied block ahead, rather than the presence or absence of trains in the previous blocks. Figure 5.1 demonstrates the principles of four-aspect signalling systems, and how "right side" and "wrong side" failures can impact their operation. The cases shown are to demonstrate how misoperations impact four-aspect signalling, however, only a subset of possible misoperations are shown. In (a), we see normal operation: train A is occupying block 5, the four signals preceding it, from closest to furthest are red (danger/stop) - indicating there is a train occupying the next block, single yellow (caution) - indicating to the driver that they must stop at the next signal, double yellow (preliminary caution) - indicating that the next signal is a single yellow, and green (clear) - the train can proceed normally. If train A remains in block 5, train B would enter block 2 normally, start to slow down in block 3, and slow to a stop in block 4. In (b), a "right side" failure has occurred in block 2: without advanced caution from the single or double yellow signals, the driver of train B now sees the signal change from green to red, meaning they would have to decelerate

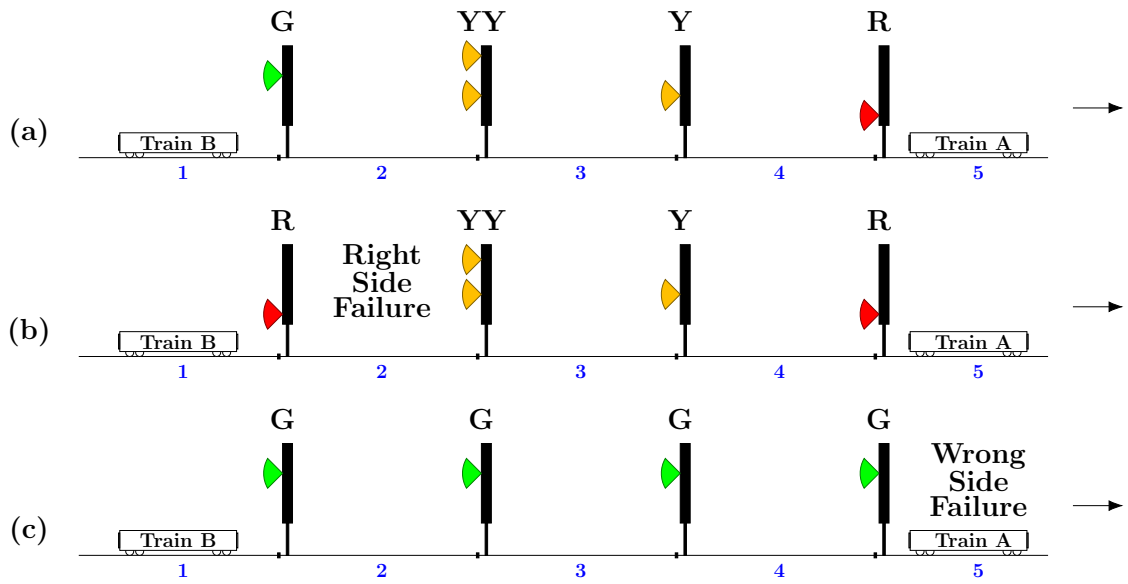

Figure 5.1: Diagram showing the operation of four-aspect signalling during (a) normal conditions, (b) a "right side" failure in block 2, and (c) a "wrong side" failure in block 5. The direction of travel is left to right.

the train more rapidly than normal to attempt to avoid passing the red signal. In the case of a space weather induced misoperation, there is nothing hazardous in block 2 causing the signal to change, it is the induced currents causing the relay to misoperate. However, the driver does not know this, and the rapid deceleration of the train also has the potential to cause injuries to those on-board. In (c), a "wrong side" failure has occurred in block 5, currently occupied by train A: the driver of train B continues along the line, unaware that block 5 is actually occupied. This is potentially a far more hazardous case, as if the misoperation persists, there is the potential of a collision as train B may not be able to decelerate fast enough to avoid colliding with the rear of train A. Three-aspect signalling uses the same principles described above, but without the double yellow signal.

In this chapter, the analyses again focus on the Glasgow to Edinburgh via Falkirk line and the Preston to Lancaster section of the West Coast Main Line (WCML). The Glasgow to Edinburgh line is split into 70 blocks with lengths varying between 0.4−1.9 km, and the traction rail was calculated to be just over 76 km long. The

Preston to Lancaster section of the WCML consists of 25 blocks with lengths varying between 0.8−1.6 km, and the total traction rail length is not specified as this is a section of a much longer line. It is also worth noting that the Glasgow to Edinburgh line is predominantly east-west orientated, while the Preston to Lancaster section of the WCML is largely north-south orientated. The geographical location and individual track circuit blocks for both lines are shown in Figure 4.1.

5.3 Signalling System Modelling

The model used in this study is described in detail in Section 3.2. A summary of the additions made to the model to better represent a realistic railway signalling system and enable the analysis of "wrong side" failures is given below. The electrical characteristics of the rails and parameters for track circuit components are summarised in Table 4.1.

5.3.1 Cross Bonding

Where previously the model considered each single track (pair of rails) in one direction of travel individually, now it has been modified to simultaneously model both directions of track connected by wires with a total admittance of 1000 S (1 mΩ) (NR/SP/SIG/50004, 2006) called cross bonds which electrically bond both traction rails every 400 m (NR/SP/ELP/21085, 2007). The main purpose of cross bonds is to ensure traction rail continuity, if there is a break in one of the traction rails, the traction return current still has an alternate path to flow. The cross bonds effectively add two new nodes to the network (one in each direction of travel), splitting the traction rail into smaller segments in both directions, and changing the values of y_g and y_r at these nodes and adjacent nodes. As the total number of nodes has increased, the dimensions of [Y] also increases, and the sum of admittances into each node that forms the diagonal elements of [Y] that correspond to the cross bonds have an additional admittance equal to y_{cb}.

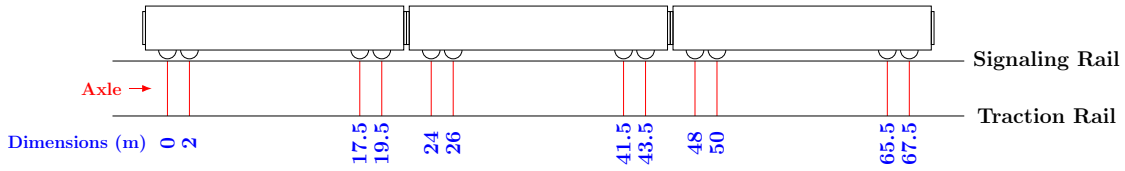

Figure 5.2: The dimensions of the wheelsets for the three-car British Rail Class 385 AT-200 that is used on the Glasgow to Edinburgh via Falkirk line. The axles (shown in red) electrically connect both rails, as the current travels between the rails through the wheels and axle.

5.3.2 Train Axles

To study "wrong side" failures, the admittances of train axles that connect the signalling and traction rails must be considered. The Glasgow to Edinburgh via Falkirk line mainly uses British Rail Class 385 AT-200 trains built by Hitachi Rail for ScotRail. We have used the three-car set as an example, detailed below, but the model could easily be adapted to other train configurations. Every car has four wheelsets (two at each end) each consisting of two wheels and an axle, and the distances between the axles has been estimated based on specifications given by Iwasaki et al. (2017), and shown in Figure 5.2. It is assumed that each axle has a resistance (known as the train shunt resistance) of 25.1 mΩ (39.8 S) (NR/SP/SIG/50004, 2006). For Preston to Lancaster, we have used the 11-car British Rail Class 390 Pendolino trains, assuming each car has the same axle dimensions as the Class 385 given above. Each axle adds two new nodes to the network (one on the signalling rail and one on the traction rail), splitting both rails into smaller segments, and changing the values of y_g and y_r at these nodes and connecting nodes. As the total number of nodes has increased, the dimensions of [Y] also increase, and the sum of admittances into each node that forms the diagonal elements of [Y] that correspond to the axles now have an additional admittance equal to y_{axle}. An updated circuit diagram (from Figure 3.12) with the addition of cross bonds and train axles is shown in Figure 5.3.

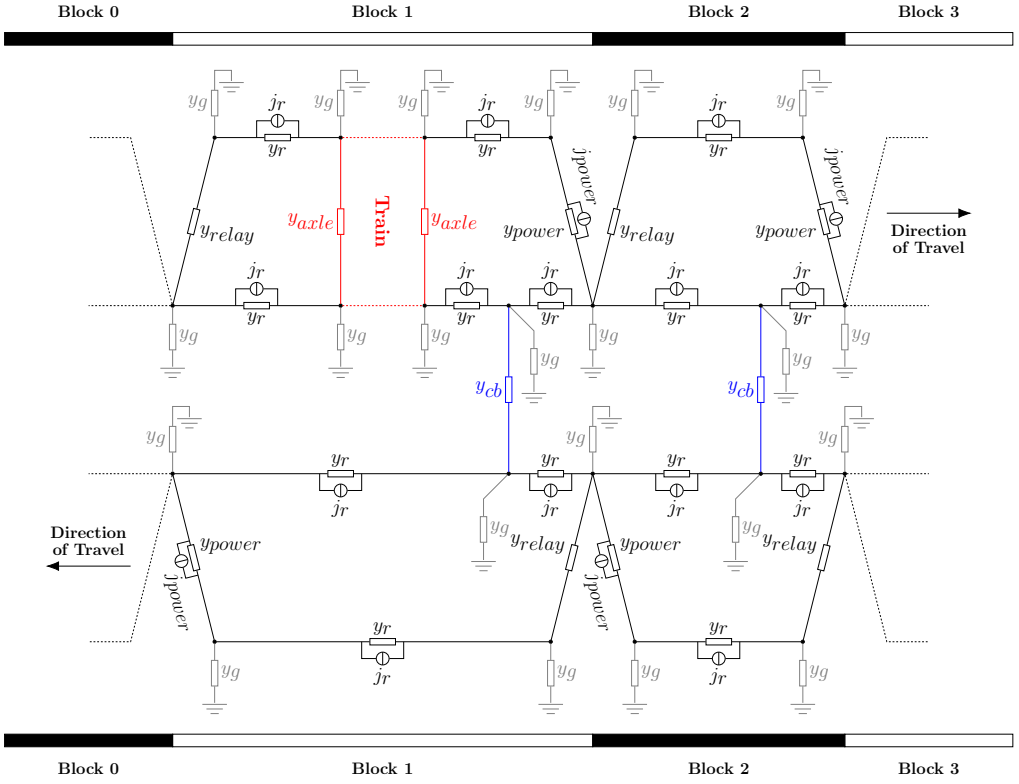

Figure 5.3: Circuit diagram showing the nodal admittance network of a section of a line with two track circuit blocks in each direction of travel. Track circuit blocks are separated by insulated rail joints in one rail but share a continuous traction rail. The traction rails are periodically connected with cross bonds (shown in blue), and there is a train in the top left block (shown in red). Only the first and last axle of the train is shown here for simplification, but every axle is included in the model. The components making up the network are the current source and admittance of the power supply (j_{power} and y_{power} respectively), the admittance of the relay (y_{relay}), the admittance to the ground at each node (y_g), the admittance due to the rail between nodes, (y_r), the currents induced in the rails due to the geoelectric field between nodes (j_r), the admittance of the cross bond (y_{cb}), and the admittance of the train axles (y_{axle}). Note that the y_g, y_r and j_r are dependent on the length of the segment and the rail's electrical characteristics, and would have varying values.

5.4 Results

5.4.1 Cross Bonding Effects

To study the effects that cross bonds have on the current through the relays at different magnitudes of geoelectric field strength, we have run the model both with and without the inclusion of cross bonds for 0, 5, and $-5\,\mathrm{V\,km^{-1}}$ and compared the results. Figure 5.4 shows the current differences through the relays when cross bonds are added. For each relay in the eastwards direction, we see that the current differences are shifted in a positive or negative direction depending on the orientation of the electric field, and this shift is reversed for the opposite direction of travel. We also see that the extent to which the current differences change with electric field strength is less prominent at the ends of the line and more significant at the centre. This is due to the inherent properties of the line discussed in Chapter 4, and the shorter length of track circuit blocks at both ends of the line, which may not contain a cross bond. When compared with the range of normal current values of -0.5 to $0.5\,\mathrm{A}$, it is apparent that the magnitude of the current differences is very small, so the inclusion of cross bonds has minimal impact on the operation of the track circuits both during normal operation and during a geomagnetic storm. However, cross bonds are still included to ensure the model is as realistic as possible. A similar analysis was undertaken for the effects of axles, but it was found that trains (multiple sets of axles) within a block had no significant impact on the currents in adjacent blocks.

5.4.2 Distance Along a Block

While investigating the conditions required for "wrong side" failures to occur, it was found that the position of the train in a block is a major factor, as the distance a train has travelled along the block, and hence the lengths of rail between the rear-most axle and the start of the block, will impact the amount of GIC that can affect the relay.

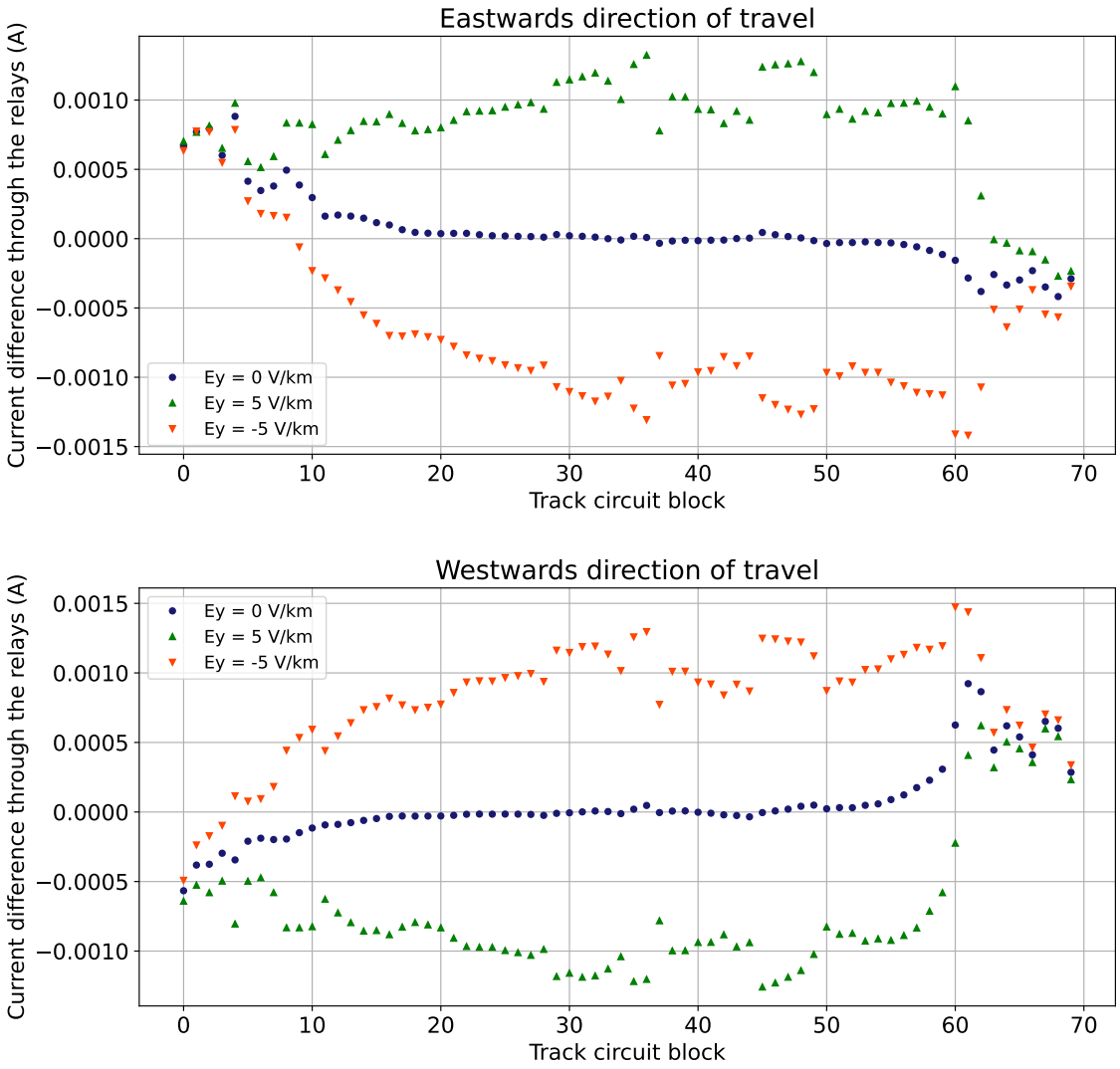

Figure 5.4: The difference in relay current with and without cross bonds for the Glasgow to Edinburgh via Falkirk line in the eastwards and westwards directions of travel at electric field values of 0, 5, and $-5\,\mathrm{V\,km^{-1}}$. The current differences are shifted in a positive or negative direction depending on the orientation of the electric field, and this shift is reversed for the opposite direction of travel.

How the signals change as a train moves along the line for the example of two-aspect signalling is shown in Figure 5.5. Focusing on the middle (blue) block: In Figure 5.5(a), when a train first enters the block, the signal changes to red as the axles bypass the relay. At this point, the signal in the previous block should also be red, as the train has yet to vacate it completely. In Figure 5.5(b), the train has moved forward such that it is now completely within the block, the signal behind changes to green as the previous block is now unoccupied. As the train starts moving away from the relay, if there is an external electric field, induction in the rails behind the train starts to drive a current through the relay. Figure 5.6 shows that because the relay is positioned at the end of the block that the train enters from, the length of rail on the relay side of the train (from which induced currents can reach the relay) increases as the train moves through the block, causing the amount of induced current through the relay to increase as the train progresses. The effect on the current through the relay is shown in Figure 5.7, where we see that the magnitude of the current increases with both distance travelled through the block and the electric field strength applied. Finally, in Figure 5.5(c), most of the train has passed into the next block, so the signal for that section is red since it is occupied by a train. When the train is at the end of a block, the potential for "wrong side" failure is highest, as the distance between the relay and the rearmost axle of the train has reached a maximum while the train is still occupying the block. It is also worth noting that the unoccupied blocks (with green signals) are potentially vulnerable to misoperations in the form of "right side" failures. In the analyses below, the positions of the trains are always set at the power supply end of the block, i.e., just prior to exiting the block, to model the worst case scenario in terms of positioning that will have the biggest impact on signalling systems.

5.4.3 Thresholds for "Wrong Side" Failure

To find the thresholds at which "wrong side" failures occur for each block in both directions of travel, increasing values of uniform electric field were applied to each

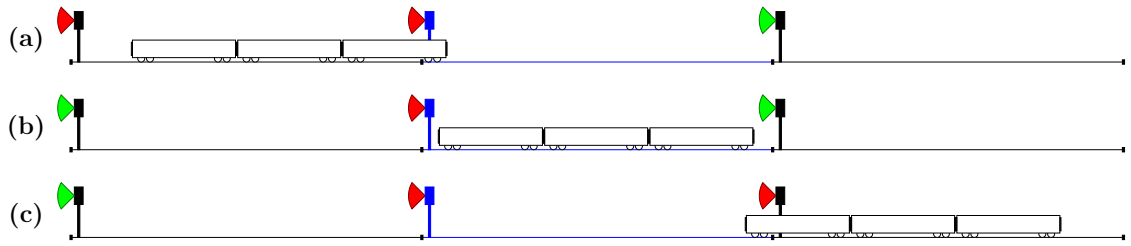

Figure 5.5: Diagram showing how the signals in a two-aspect system change as a train is travelling along a line. In (a), the train has just entered the block, the signal changes to red as the axles bypass the relay. The signal in the previous block remains red, as it is still occupied by the back end of the train. In (b), the train is now completely within a block, the signal in the previous block changes to green as it is now unoccupied. In (c), almost the entire train has entered the next section, turning the signal for that block red. When the train is positioned at this end of the block, the potential for "wrong side" failure is highest, as it is the maximum distance between the relay and the axles of the train while the train is still occupying the block.

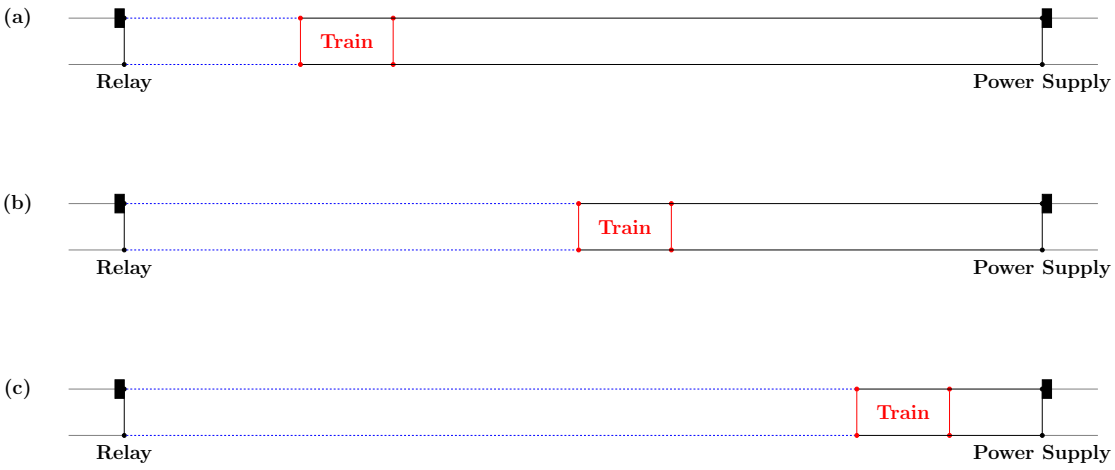

Figure 5.6: Train axles (indicated by vertical red lines) cut off the power supply current from the relay, effectively splitting the block into two circuits. The number of axles on a train is dependent on the number of carriages, only a single set is shown here for simplicity. In this case, the only source of current reaching the relay is induced in the rails by the electric field. The blue (dashed lines) show the portion of the rails within the relay-side circuit. As the train moves from its position in (a) to (b) to (c), the size of the relay-side circuit grows, and more of the current induced in the rails can reach the relay.

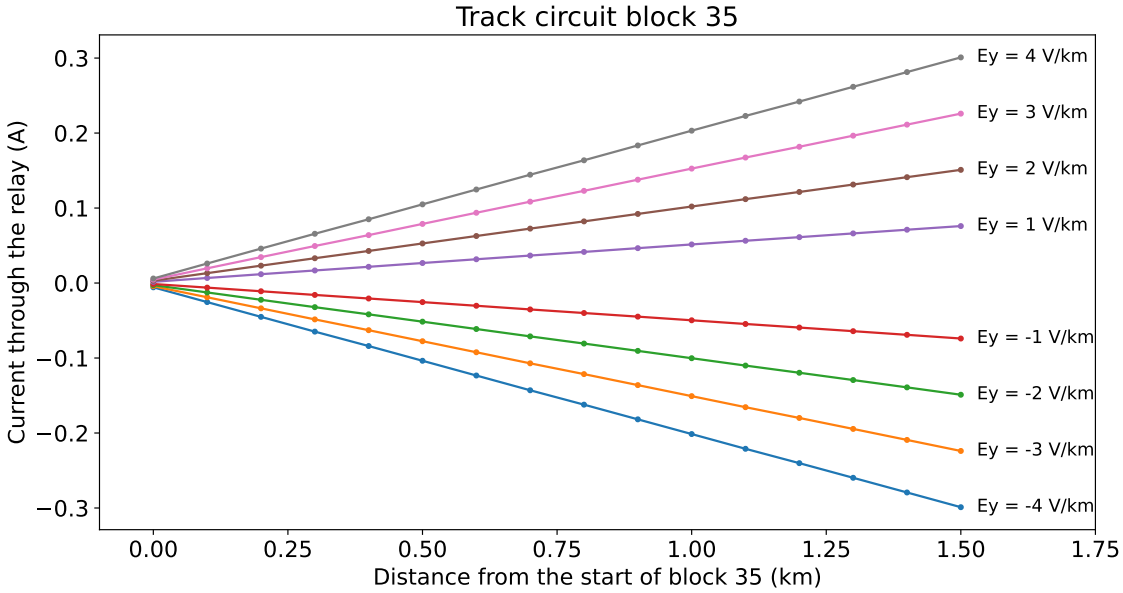

Figure 5.7: As a train passes through a track circuit block, the magnitude of current across the relay increases. This is due to the distance increase along the block between the axle (which is cutting off the power supply current) and the relay, so more of the rail's induced current is able to reach the relay. The magnitude of the current through the relay also increases with an increased electric field strength.

block (eastwards orientated for Glasgow to Edinburgh and northwards orientated for Preston to Lancaster) until the first "wrong side" failure occurred, and the electric field strength at that point was recorded. In this case, the train is at the power supply end of the block to allow the largest amount of induced current to reach the relay. Figure 5.8 shows the threshold electric field required to trigger a "wrong side" failure in each track circuit block for both directions of travel on the Glasgow to Edinburgh line. The blue crosses indicate the threshold at moderate leakage values, while the blue lines illustrate how the threshold changes with differing leakage in response to environmental conditions, as described later in Section 5.4.4. Leakage values for wet, moderate and dry conditions are given in Table 4.1. For a few track circuit blocks at either end of the line, the thresholds for misoperation are not shown. This is due to these values far exceeding the reasonable value for electric field strengths during space weather events, with some values in the hundreds of volts per kilometre. It is shown that the smallest magnitude electric field strength threshold for "wrong side" failure occurs in track circuit block 36 for both the eastwards and westwards directions of travel with values of $-1.0\,\mathrm{V\,km^{-1}}$ and $1.0\,\mathrm{V\,km^{-1}}$ respectively. This is likely due to this block's position towards the centre of the line, its long block length, and its almost east-west orientation. Figure 5.9 shows the results for the Preston to Lancaster section of the WCML, the smallest magnitude electric field strength threshold for "wrong side" failure occurs in track circuit block 6 for northwards and southwards directions of travel with values of $-1.1\,\mathrm{V\,km^{-1}}$ and $1.1\,\mathrm{V\,km^{-1}}$ respectively. The asymmetry between the threshold electric field value at each block in both directions of travel comes from the relative position of the cross bonds within the blocks, and the reversed positioning of the power supply and relay.

As the magnitude of the electric field is increased, the number of blocks that have the potential to experience "wrong side" failures increases, as shown in Figure 5.10 (obtained using Figure 5.8). This shows the total number of track circuits in the Glasgow to Edinburgh line that have the potential to experience "wrong side"

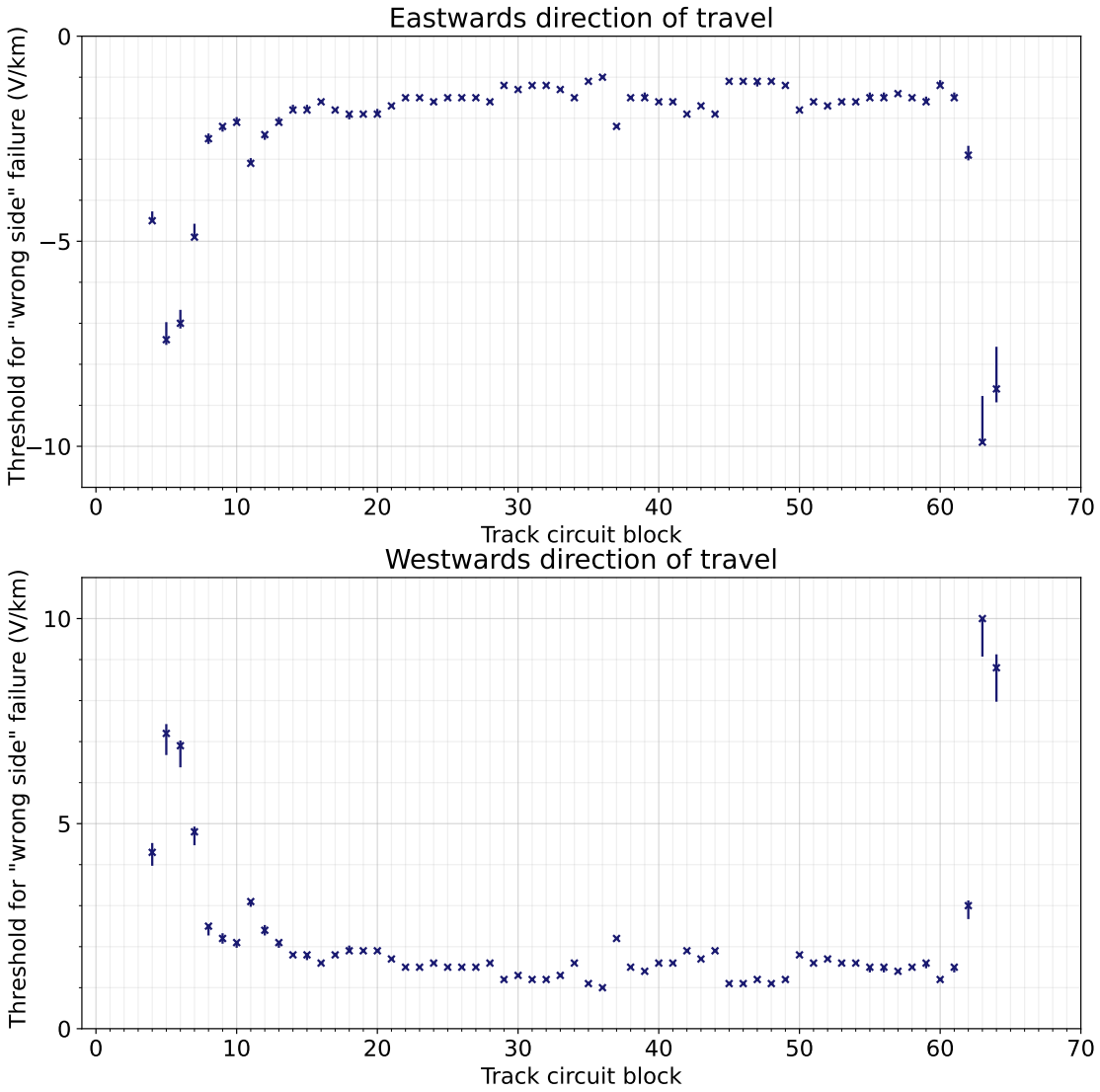

Figure 5.8: Glasgow to Edinburgh: The threshold west-east electric field values to cause "wrong side" failure for each track circuit block in both eastwards and westwards directions of travel. In both directions of travel, Glasgow is on the left and Edinburgh on the right.

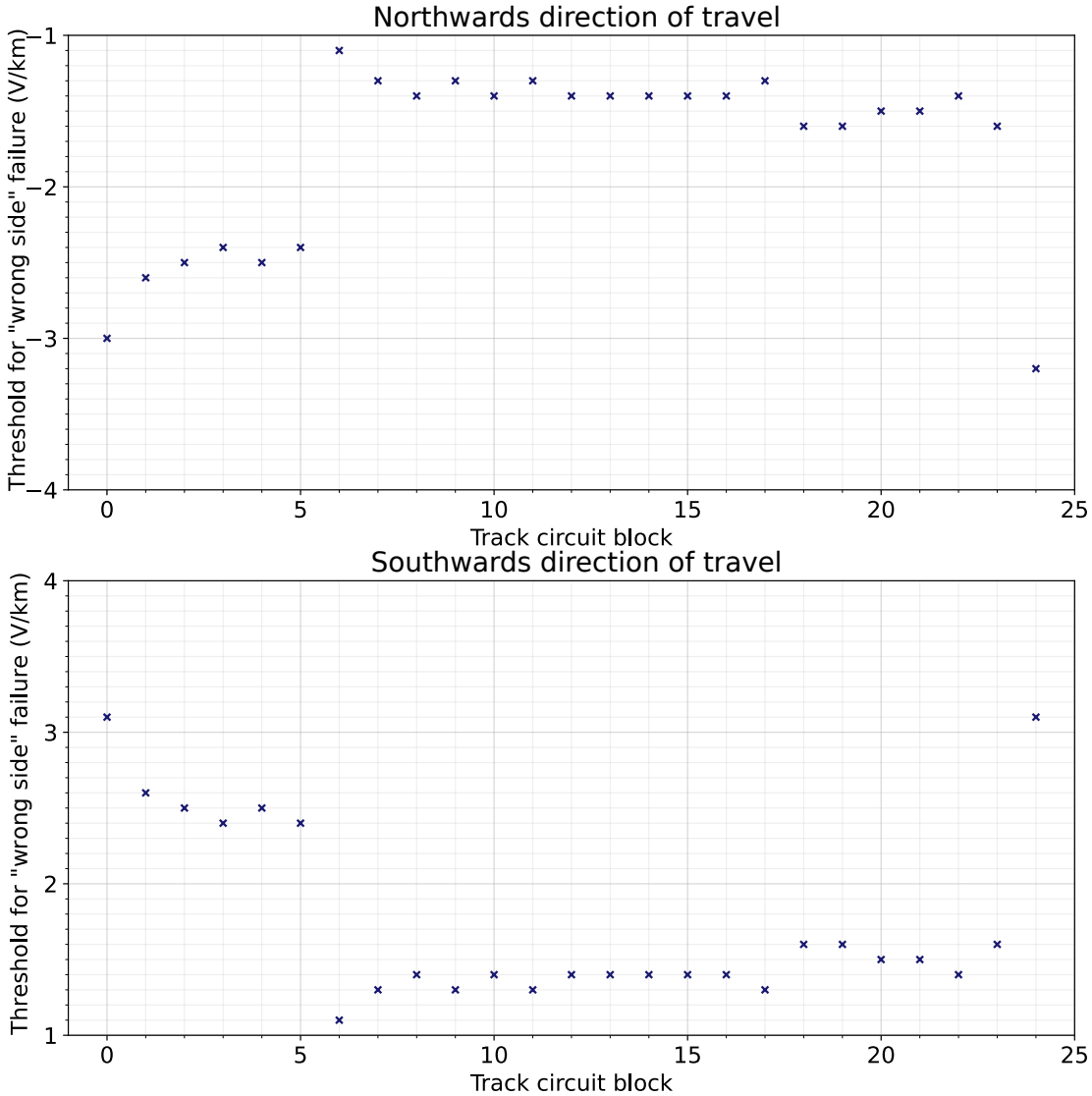

Figure 5.9: Preston to Lancaster: The threshold south-north electric field values to cause "wrong side" failure for each track circuit block in both northwards and southwards directions of travel.

failures for a given electric field strength, regardless of their location within the line. It is important to note that in reality, not all blocks will be occupied by trains at the same time, so this represents a worst case scenario and highlights the number of relays that have the potential to experience "wrong side" failures. In practice, as we explore in Section 4.5, the precise number of "wrong side" failures will depend on the number and distribution of trains on the line as well as the electric field applied. The blue (right facing) triangles indicate the eastwards direction of travel and the orange (left facing) triangles are the westwards direction of travel. Between 1 to $3\,\mathrm{V\,km^{-1}}$ for the westwards direction of travel and -1 to $-3\,\mathrm{V\,km^{-1}}$ for the eastwards direction of travel, there is a steep increase in the number of potential "wrong side" failures, meaning that the threshold for misoperation for most blocks lies within these ranges. Beyond $\pm 3\,\mathrm{V\,km^{-1}}$, larger increase in the magnitude of the electric field strength is needed to cause further potential "wrong side" failures. This is due to multiple factors: (1) some blocks are orientated in such a way that the component of the eastwards electric field parallel to the rails is small, so a larger electric field is needed to induce enough current to cause a misoperation; (2) blocks of shorter length need larger electric fields to induce the currents required to cause a misoperation; (3) the innate properties of the transmission line discussed in Chapter 4, which are independent of block length and orientation, cause the current through the relays in blocks at the ends of each line to be more resistant to changes with electric field strength. These factors mean that the threshold for "wrong side" failure in some blocks is much higher, a few of which exceed hundreds of volts per kilometre and are not shown here. We see a similar result for the Preston to Lancaster section of the WCML in Figure 5.11 (obtained using Figure 5.9), however, as it is a centre section of the WCML, we do not see the effects of the ends of the line as we do with the Glasgow to Edinburgh line. At $-3.2\,\mathrm{V\,km^{-1}}$ and $3.1\,\mathrm{V\,km^{-1}}$ respectively, all of the relays in the northwards and southwards directions of travel would have the potential to experience "wrong side" failures.

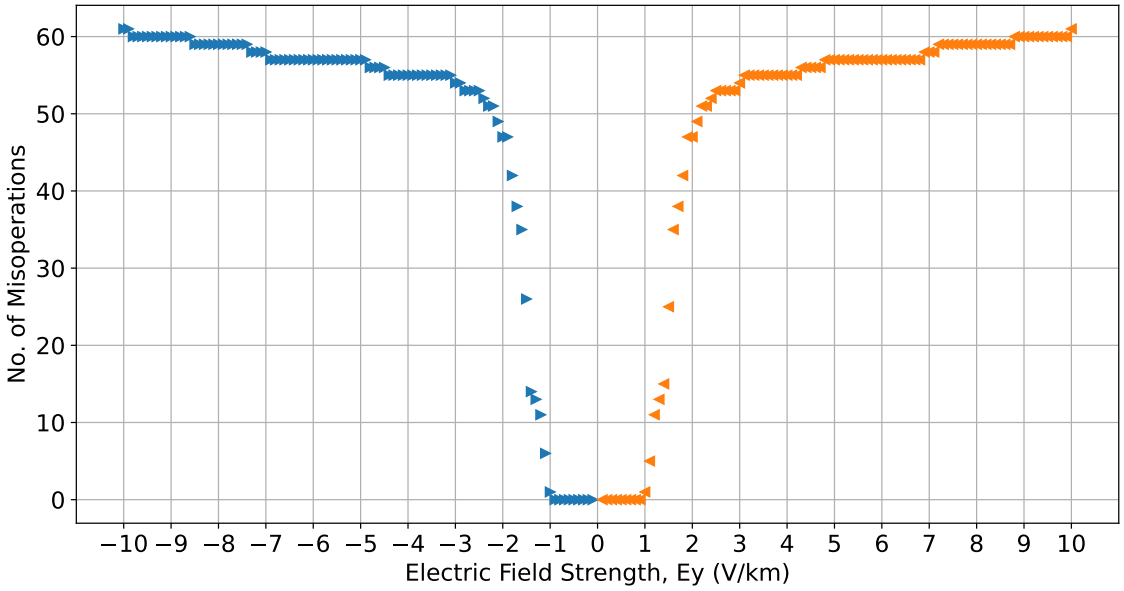

Figure 5.10: Glasgow to Edinburgh: The number of track circuit blocks with the potential to experience "wrong side" failures at different magnitudes of electric field strength for both the eastwards and westwards directions of travel. The blue (right facing) triangles and the orange (left facing) triangles indicate the eastwards and westwards directions of travel respectively.

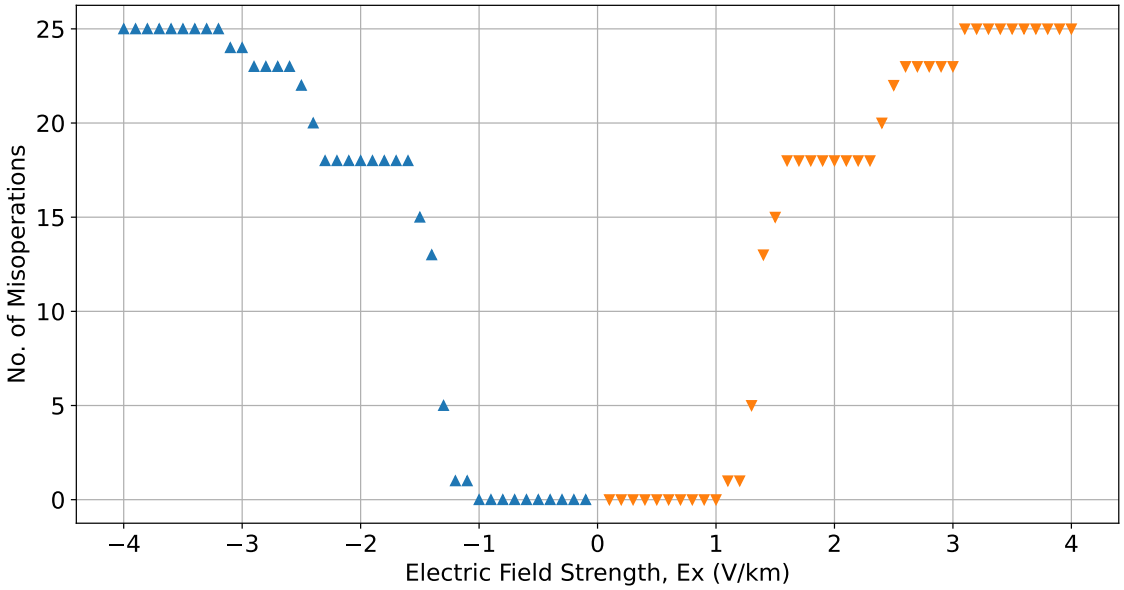

Figure 5.11: Preston to Lancaster: The number of track circuit blocks with the potential to experience "wrong side" failures at different magnitudes of electric field strength for both the northwards and southwards directions of travel. The blue (up facing) triangles and the orange (down facing) triangles indicate the northwards and southwards directions of travel respectively.

5.4.4 Effects of Leakage Change

The leakage from the rails to the ground can change with environmental conditions, increasing in wetter weather and decreasing in drier weather. The model was run with leakage values derived from Network Rail standard NR/GN/ELP/27312 (2006), shown in Table 1, to provide a range of "wrong side" failure thresholds. Figure 5.8 shows that increasing or decreasing the leakage of the rails affects the track circuit blocks towards the ends of the line more than at the centre, this is largely due to the properties of the transmission line. This can be demonstrated by creating a test network of $70 \times 1\,\mathrm{km}$ blocks in each direction of travel with the same orientation (parallel to the electric field direction), each occupied by a train. This makes the results independent of the two other main factors that determine the misoperation thresholds - block length and orientation. In Figure 5.12, the blue crosses indicate moderate leakage, the orange (upwards) triangles are maximum leakage, and the green (downwards) triangles are minimum leakage. Both directions of travel have an electric field of $E_y = -5\,\mathrm{V\,km^{-1}}$ applied. The current across the relays in the eastwards direction of travel have increased, possibly driving "wrong side" failures, and the currents across the westwards direction of travel have decreased, which would not lead to "wrong side" failures. This is consistent with the results from Figure 5.8, which show that negative electric fields can cause "wrong side" failures in the eastwards direction of travel, but not the westwards direction of travel. It is shown that the difference in leakage has a larger impact on the current through the relays that are near the ends of the line when compared with those in the middle, hence the threshold for "wrong side" failures for blocks near the end are more sensitive to changes in leakage due to transmission line properties, and not block length or orientation. This explains why we do not see leakage having an impact on the blocks in the Preston to Lancaster section of the WCML, due to it being a centre part of a longer line.

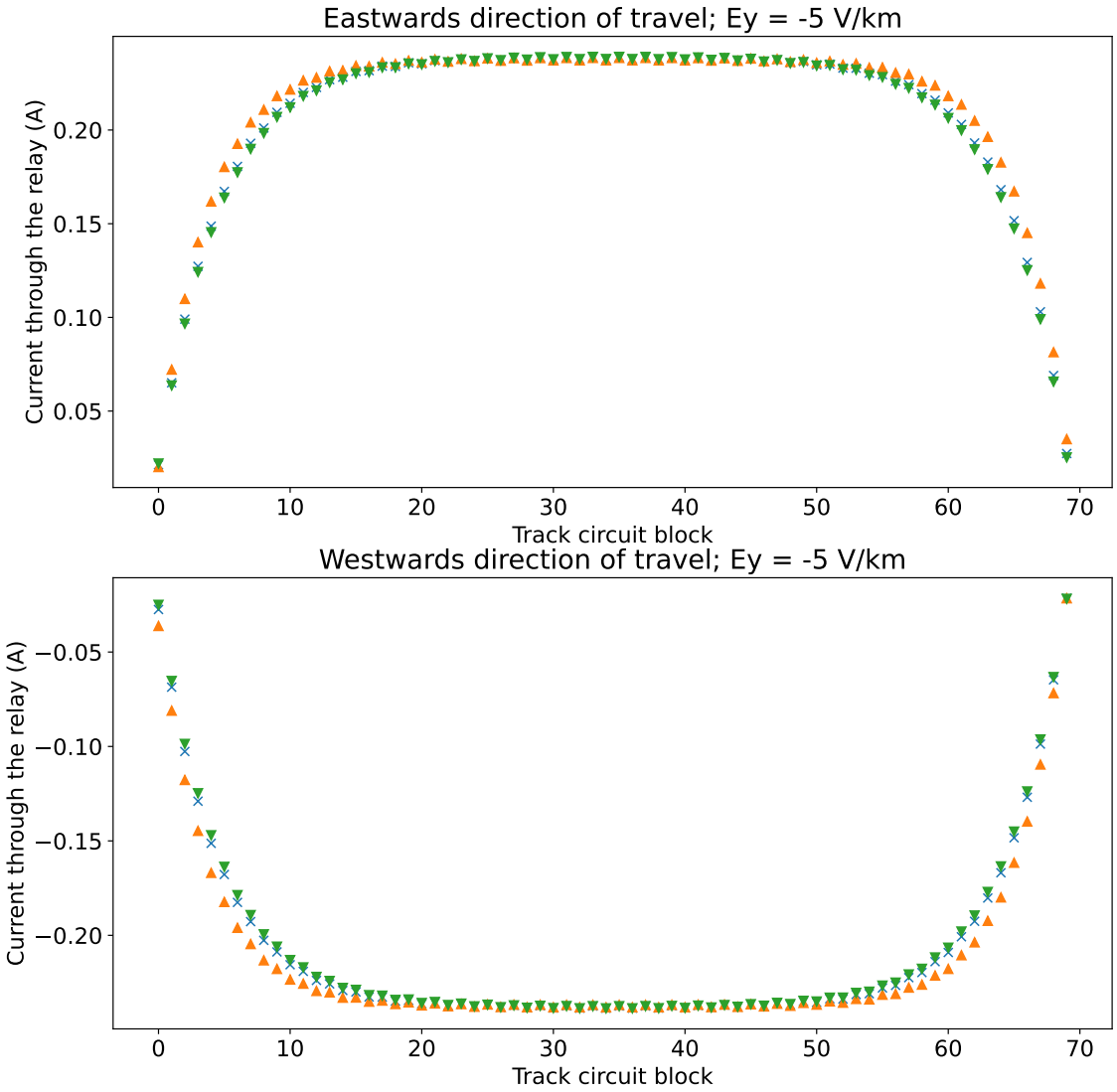

Figure 5.12: The current through the relays in the eastwards and westwards directions for the 70×1 km block test network where all blocks are orientated parallel to the direction of the electric field ($E_y = -5\,\mathrm{V\,km^{-1}}$), and it is assumed that each block is occupied by a train meaning no current from the power supply is reaching the relay. The blue crosses indicate moderate leakage, the orange (upwards) triangles are maximum leakage, and the green (downwards) triangles are minimum leakage.

5.4.5 Applying Uniform Electric Fields

In the following analysis, we have used the example where 7 trains are relatively evenly spaced along the Glasgow to Edinburgh line, and 5 are spaced along the Preston to Lancaster section of the WCML, this is so we can show "right side" failures occurring at the same time as "wrong side" failures. The choice of the number of trains is loosely based on the frequency of trains along those routes, however, this number can differ greatly depending on the density of traffic, which in turn changes depending on the time of day. The number of "wrong side" failures is dependent on how many trains are occupying the blocks and where those occupied blocks are along the line. We use Figure 5.10 and Figure 5.11 to quantify the total number of track circuits that have the potential to experience "wrong side" failures given the previously stated assumptions that trains are near the ends of the blocks for both the Glasgow to Edinburgh line and the Preston to Lancaster section of the WCML in the analysis that follows.

5.4.5.1 Threshold Value

Figures 5.13(a) and (b) show the current through the relay of each track circuit block in the eastwards and westwards directions of travel of the Glasgow to Edinburgh line, respectively, assuming no external electric field is applied and 7 trains in each direction. The red (solid) line is the 'drop-out current' the value below which the current must drop to de-energise the relay, turning the signal red; the green (dashed) line is the 'pick-up current', the value above which the current must rise to energise the relay, turning the signal green. A green ring with no fill indicates an unoccupied block operating normally, and a red triangle with no fill is an occupied block operating normally, with the direction of the triangle showing the direction of travel (right for eastwards and left for westwards). It can be seen that under these conditions, all relays are operating normally. The threshold electric field value at which "wrong side" failures begin to occur is shown in the bottom two panels, $E_y = -1.0\,\mathrm{V\,km^{-1}}$ for eastwards in Figure 5.13(c), and $E_y = 1.0\,\mathrm{V\,km^{-1}}$ for westwards

in Figure 5.13(d). In both directions of travel, block 36 experiences the first "wrong side" failure, which is indicated by a filled green triangle. Figure 5.14 shows the same results for Preston to Lancaster but assuming 5 trains in each direction, with the direction of the triangle showing the direction of travel (right for northwards and left for southwards). Figures 5.14(a) and (b) show the case when no external electric field is applied, and all relays are operating correctly. The threshold electric field value at which "wrong side" failures begin are $E_x = -1.1\,\mathrm{V\,km^{-1}}$ for northwards in Figure 5.14(c), and $E_x = 1.1\,\mathrm{V\,km^{-1}}$ for southwards in Figure 5.14(d), occurring in block 6 in both cases.

5.4.5.2 Known Misoperation Value

The magnitude of the electric field known to have caused signalling misoperations in the past in Sweden is estimated to be around $4\,\mathrm{V\,km^{-1}}$ (Wik et al., 2009). With an electric field of this strength applied, Figure 5.15 shows the example for the Glasgow to Edinburgh line, where both types of misoperation ("wrong side" failures and "right side" failures) occur. According to Figure 5.10, 55 blocks have the potential to experience a "wrong side" failure for both the eastwards at $E_y = -4\,\mathrm{V\,km^{-1}}$ and the westwards direction of travel at $E_y = 4\,\mathrm{V\,km^{-1}}$. As for "right side" failures, we see 16 misoperations in the eastwards at $E_y = 4\,\mathrm{V\,km^{-1}}$ and 12 misoperations in the westwards direction of travel at $E_y = -4\,\mathrm{V\,km^{-1}}$. Figure 5.16 shows the cases for the Preston to Lancaster section of the WCML, where, according to Figure 5.11, 25 blocks have the potential to experience a "wrong side" failure for both northwards at $E_x = -4\,\mathrm{V\,km^{-1}}$ and southwards at $E_x = 4\,\mathrm{V\,km^{-1}}$. As for "right side" failures, there are 11 misoperations along the northwards at $E_x = 4\,\mathrm{V\,km^{-1}}$, and 13 misoperations in the southwards direction of travel at $E_x = -4\,\mathrm{V\,km^{-1}}$.

5.4.5.3 1-in-100 Year Extreme Estimate

If we apply the estimate for a 1-in-100 year extreme geoelectric field for the UK, estimated by Beggan (2015) to be approximately $5\,\mathrm{V\,km^{-1}}$, the examples are

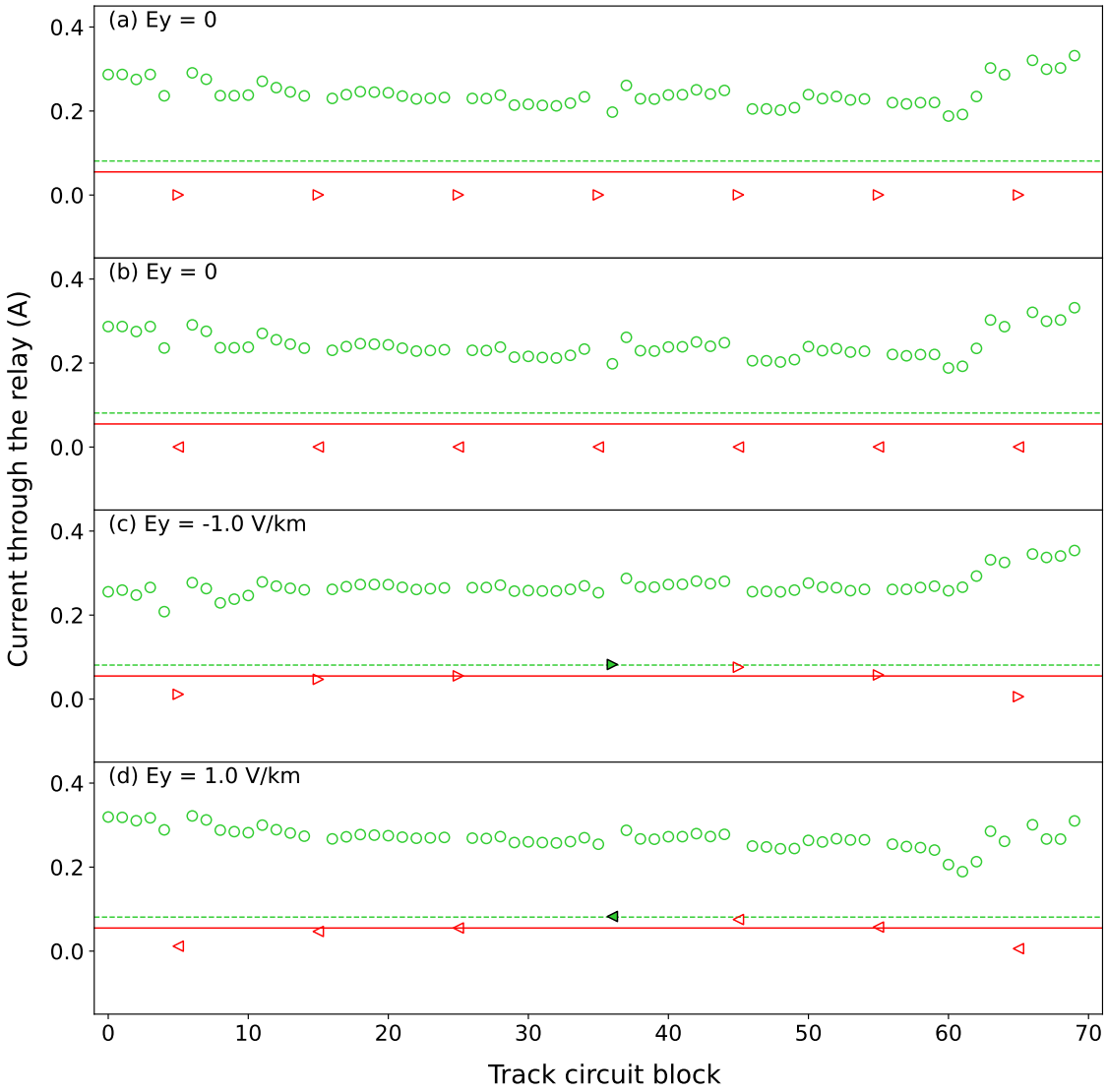

Figure 5.13: Glasgow to Edinburgh: The current through each relay when no electric field is applied for the eastwards (a) and westwards (b) directions of travel, and at the threshold for "wrong side" failure in the (c) eastwards and (d) westwards directions of travel. With no electric field applied, all relays are operating normally. At the threshold for "wrong side" failure, we see one misoperation in either direction of travel.

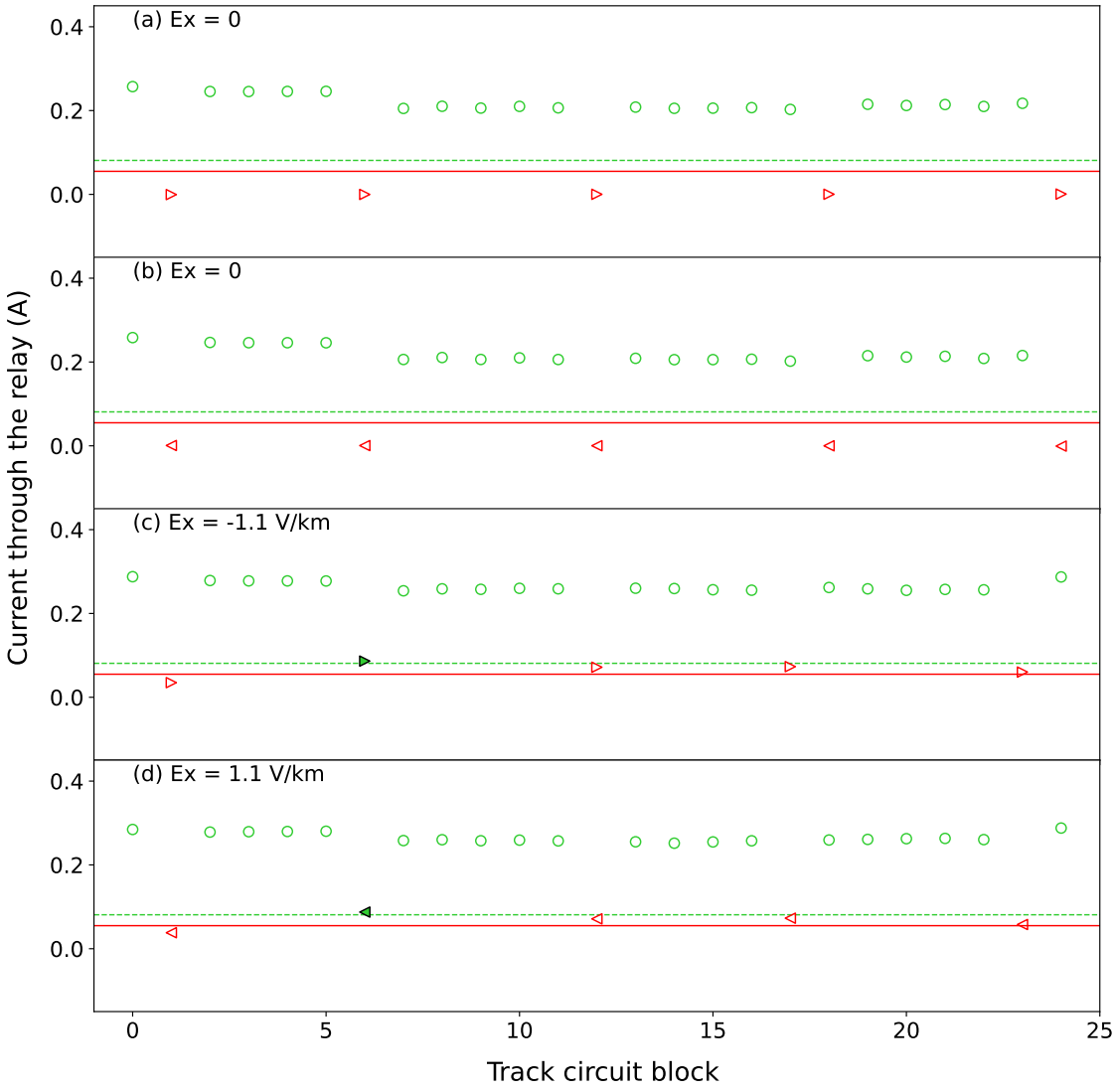

Figure 5.14: Preston to Lancaster: The current through each relay when no electric field is applied for the northwards (a) and southwards (b) directions of travel, and at the threshold for "wrong side" failure in the (c) northwards and (d) southwards directions of travel. With no electric field applied, all relays are operating normally. At the threshold for "wrong side" failure, we see one misoperation in either direction of travel.

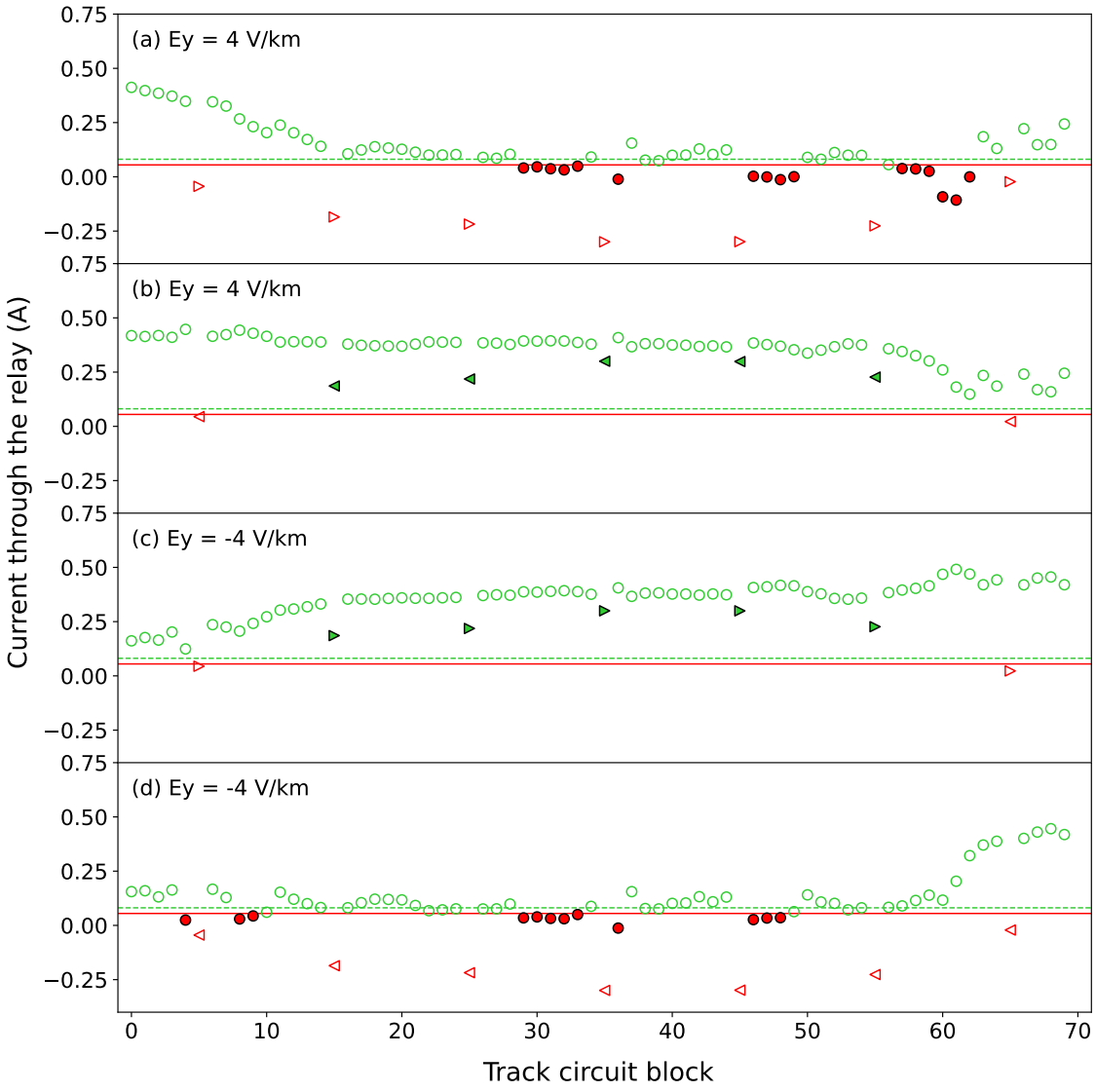

Figure 5.15: Glasgow to Edinburgh: The current through each relay at $E_y = 4\,\mathrm{V\,km^{-1}}$ in the (a) eastwards and (b) westwards directions of travel, and at $E_y = -4\,\mathrm{V\,km^{-1}}$ in (c) eastwards and (d) westwards directions of travel. Here we see both types of misoperation occurring in both directions depending on the orientation of the electric field.

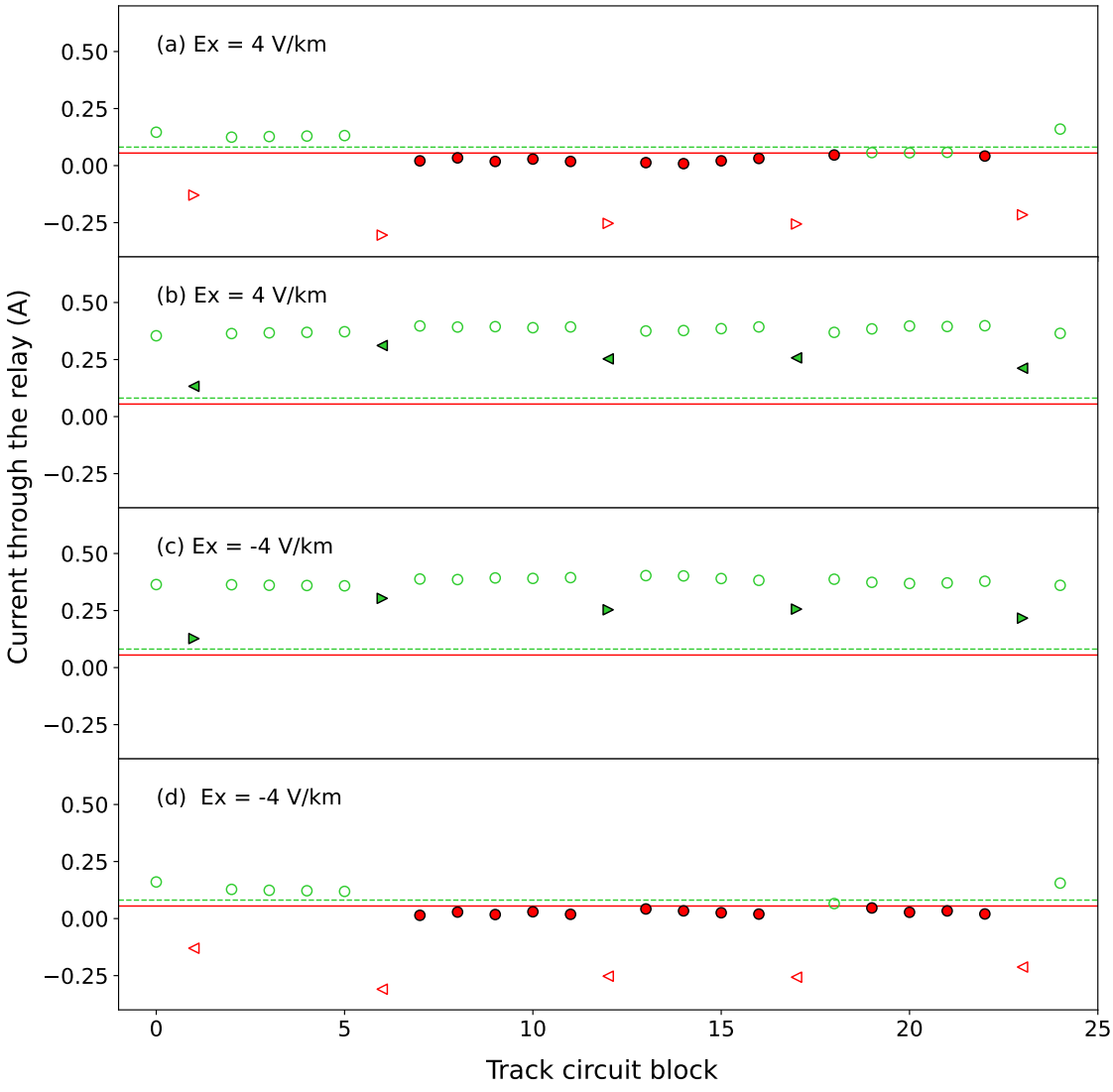

Figure 5.16: Preston to Lancaster: The current through each relay at $E_x = 4\,\mathrm{V\,km^{-1}}$ in the (a) northwards and (b) southwards directions of travel, and at $E_x = -4\,\mathrm{V\,km^{-1}}$ in (c) northwards and (d) southwards directions of travel. Here we see both types of misoperation occurring in both directions depending on the orientation of the electric field.

shown in Figure 5.17. According to Figure 5.10, the number of track circuits that could potentially experience a "wrong side" failure increases slightly from the from $\pm 4\,\mathrm{V\,km^{-1}}$ value to 56 blocks for eastwards at $E_y = -5\,\mathrm{V\,km^{-1}}$ and 57 blocks for westwards at $E_y = 5\,\mathrm{V\,km^{-1}}$. This is due to the relays towards the ends of the line having much higher thresholds and most relays having already misoperated between ± 1 to $3\,\mathrm{V\,km^{-1}}$. We do see an increase in the number of "right side" failures, with over a third of unoccupied blocks misoperating in both directions of travel. For the examples of Preston to Lancaster in Figure 5.18, the number of track circuits that could potentially experience a "wrong side" failure cannot increase any further, as the threshold misoperation value for each track circuit had already been reached for both directions of travel at $\pm 4\,\mathrm{V\,km^{-1}}$. However, we do see an increase in the number of "right side" failures occurring in both directions of travel, with nearly all relays experiencing misoperation. The results for "right side" failures agree with Chapter 4. It is apparent that a 1-in-100 year extreme event could result in a significant number of signal misoperations.

5.5 Discussion

The model used in this study builds upon the work set out in Chapter 4. With the addition of cross bonds linking together both directions of travel in the line, and train axles to allow the study of "wrong side" failures, we further improve the realism of the model, and the scope of the investigation into the impacts of space weather on railway signalling systems in the UK. The continued usage of Network Rail standards documents ensures we are using appropriate parameters for the UK case, but even the UK network is not homogeneous, so the model is designed to be easily adapted to different rail and track circuit parameters. The model could therefore be used to study railway networks in other countries also with minimal effort provided the data is easily accessible, which is not always the case.

The statistics of electric field and horizontal magnetic field changes reported by

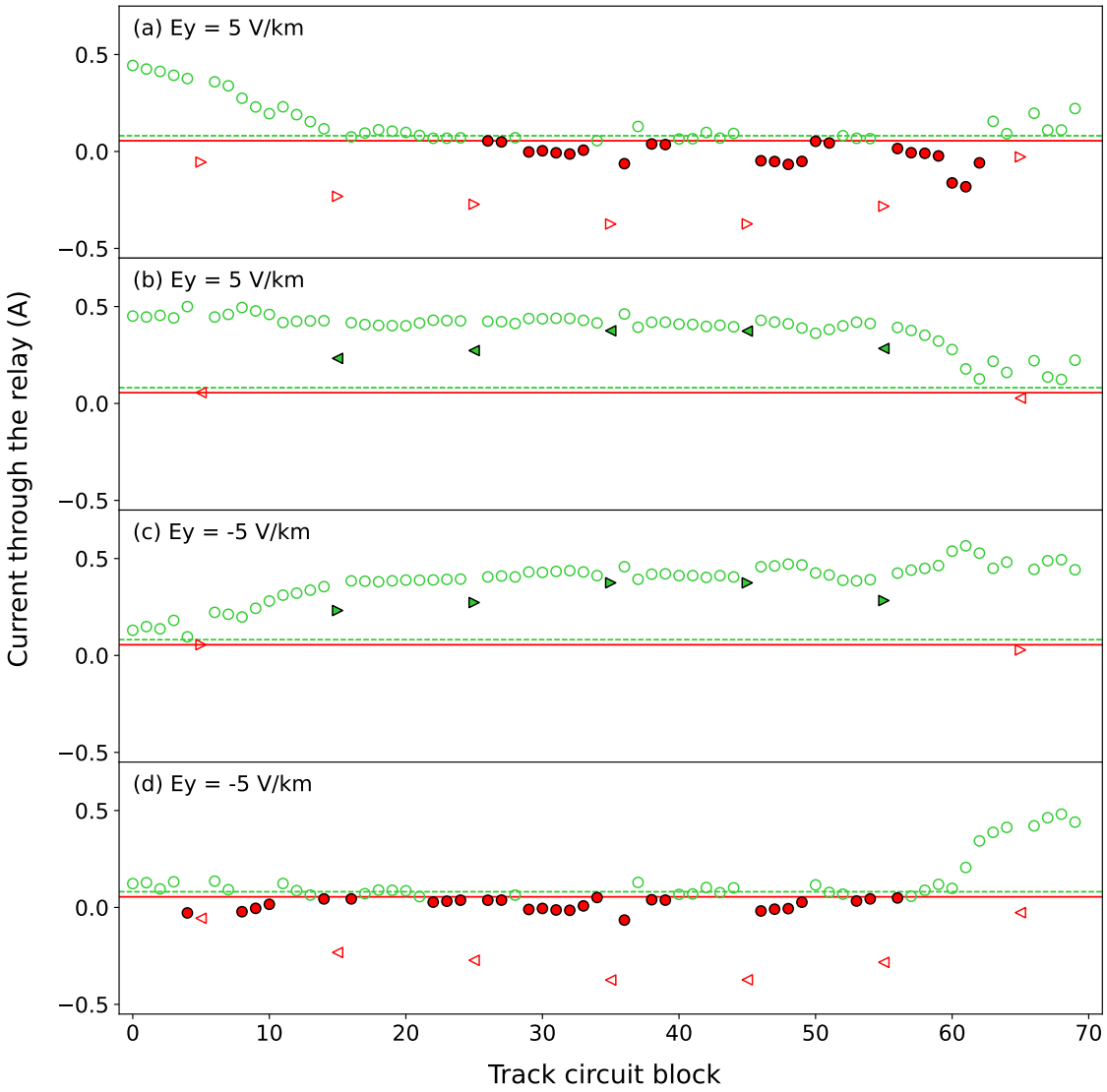

Figure 5.17: Glasgow to Edinburgh: The current through each relay at the 1-in-100 year extreme geoelectric field estimate of $E_y = 5\,\mathrm{V\,km^{-1}}$ in the (a) eastwards and (b) westwards directions of travel, and $E_y = -5\,\mathrm{V\,km^{-1}}$ in (c) eastwards and (d) westwards directions of travel. Here we see both types of misoperation occurring in both directions depending on the orientation of the electric field.

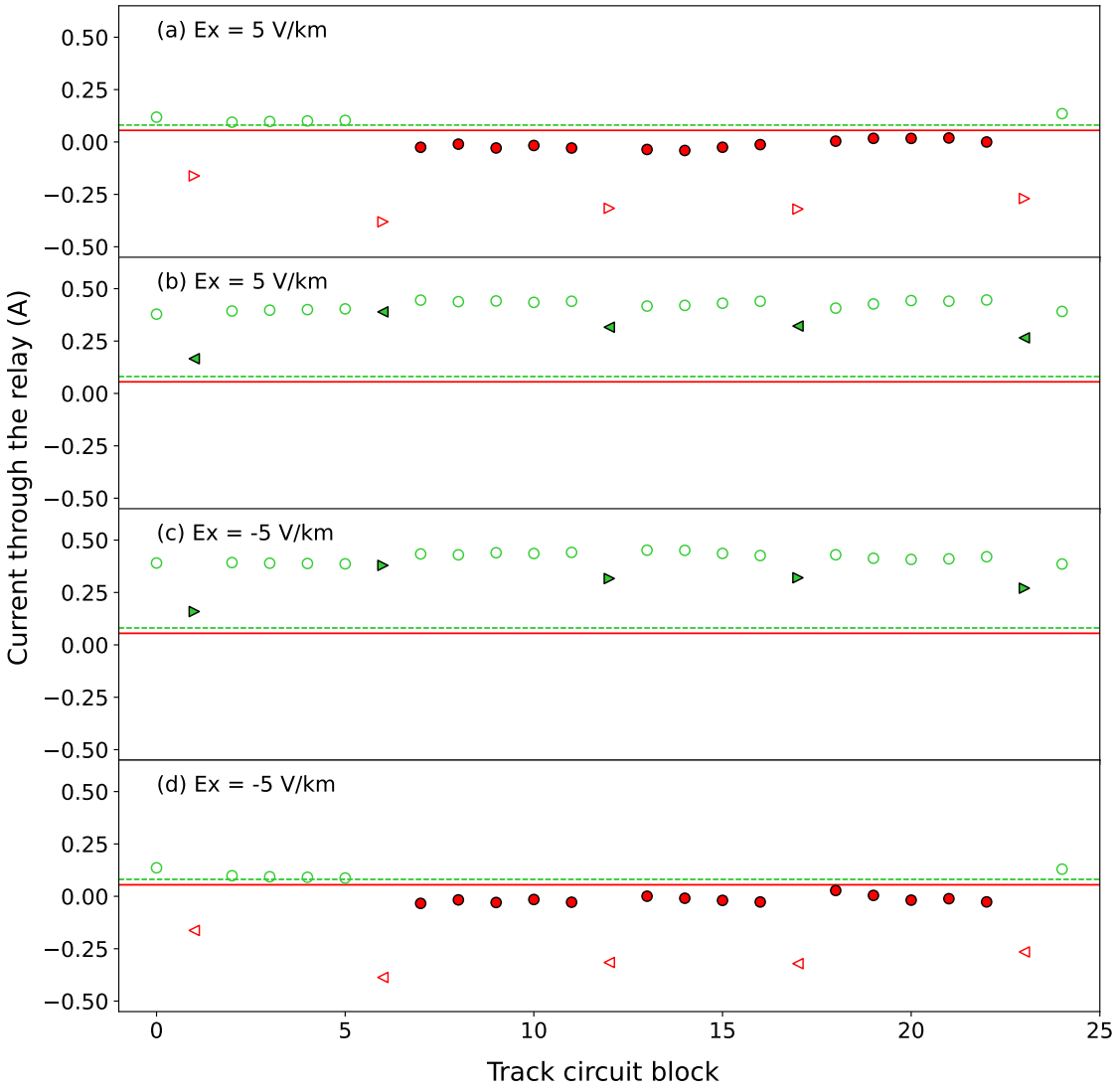

Figure 5.18: Preston to Lancaster: The current through each relay at the 1-in-100 year extreme geoelectric field estimate of $E_x = 5\,\mathrm{V\,km^{-1}}$ in the (a) northwards and (b) southwards directions of travel, and $E_x = -5\,\mathrm{V\,km^{-1}}$ in (c) northwards and (d) southwards directions of travel. Here we see both types of misoperation occurring in both directions depending on the orientation of the electric field.

Beggan et al. (2013) and Rogers et al. (2020) suggest that the threshold at which "wrong side failures would occur (around $\pm 1\,\mathrm{V\,km^{-1}}$) is exceeded in events that arise once every 10-20 years. Comparing the threshold electric field to cause "wrong side" failures in this study to the threshold for "right side" failures in Chapter 4, it is apparent that the strength of the electric field needed to cause a "wrong side" failure is lower than is needed to cause a "right side" failure provided the assumptions given in previous sections are met. To cause a "wrong side" failure, due to the train axles cutting off the power supply, the current flowing through the relay is almost entirely the induced current from the electric field. However, in the case of "right side" failure, for the induced current to de-energise the relay, it must overcome the current already present in the circuit from the power supply. It is this difference in current that is responsible for the different threshold values for misoperation.

While it is important to consider the electric field strength threshold for "wrong side" failures, at the same time we need to consider the conditions that need to be met for these misoperations to occur and consider their likelihood. Firstly, a train must occupy the block in question, this might not always be the case, as peak electric fields generated during a geomagnetic storm may occur overnight when traffic is less dense. Secondly, the train must be sufficiently far along the line, such that the distance between the rear axle of the train and the relay is sufficient to build up the required amount of current to cause a "wrong side" failure.

It is challenging to determine which type of misoperation is dominant. The thresholds for "wrong side" failures are lower, but they depend on the multiple factors described above happening simultaneously for misoperation to take place. In contrast, the conditions for right-side failures to occur are simpler, but a higher electric field strength is needed for misoperation to occur.

The study has centered on geoelectric fields that have a fixed direction and magnitude, although in actuality, they tend to fluctuate in intensity and direction over time. The effects of time-varying fields requires further investigation. Firstly, changes in electric field direction will have significant impact on the component

of the electric field that is parallel to the rails at each track circuit block, either increasing or reducing the level of induced currents in each over time. Secondly, the duration that geoelectric fields maintain a particular strength and/or orientation will determine whether a misoperation is a single event or a series of events. It would also be necessary to analyse the response times of different track circuit types to changes in current to determine whether the relay could respond quickly enough to rapid changes in current, though most track circuit relays are designed to react to changes in current on the millisecond scale, far faster than the resolution of electric field data would allow to be studied (NR/BR/939A, 1971). A detailed study of the impacts of time-varying electric fields on UK railway signalling is presented in Chapter 5.

5.6 Conclusion

This chapter details the results of a realistic model of geomagnetic interference in DC signalling systems on AC-electrified railway lines. Built upon the model detailed in Chapter 4, it has now been improved to study both directions of travel simultaneously, electrically bonded with cross bonds, and to consider "wrong side" failures - when train axles bypass the relays, de-energising them, but geomagnetically induced currents cause the relays to re-energise and display the wrong signal. It is assumed that in blocks that are occupied by trains, the trains are positioned near the end of each block such that GICs would have the maximum impact. This chapter also discusses the total number of blocks that could potentially experience "wrong side" failure, this indicates the total number of susceptible blocks rather than the number of "wrong side" failures that would actually be observed, as not all blocks would be occupied by trains.

We have shown that the susceptibility of a track circuit to experience a "wrong side" failure is strongly dependent on the location of the train within the track circuit block, where the risk of misoperation increases as the distance between the

train and the relay increases.

It was found that the threshold electric field strength for "wrong side" failure along the Glasgow to Edinburgh line was $E_y = -1.0\,\mathrm{V\,km^{-1}}$ for the eastwards direction of travel and $E_y = 1.0\,\mathrm{V\,km^{-1}}$ for the westwards direction of travel. For the Preston to Lancaster section of the WCML, the threshold electric field strength for "wrong side" failure was $E_x = -1.1\,\mathrm{V\,km^{-1}}$ for the northwards direction of travel and $E_x = 1.1\,\mathrm{V\,km^{-1}}$ for the southwards direction of travel. These correspond to estimates for the electric field strength of events that occur once in a decade or two. The "wrong side" failure threshold electric field strength is lower than the threshold for "right side" failure along the same line.

A uniform electric field with a magnitude of $4\,\mathrm{V\,km^{-1}}$, a value that is known to have caused misoperations on Swedish railways in the past, was applied to both routes studied, with 55 of the 70 track circuits on the Glasgow to Edinburgh line, and all of the track circuits on the Preston to Lancaster section of the WCML having the potential to experience "wrong side" failures if occupied by a train. It was also shown that there would be both "wrong side" and "right side" failures in opposite directions of travel.

Applying an electric field with a magnitude of $5\,\mathrm{V\,km^{-1}}$, which is the estimate for a 1-in-100 year extreme event in the UK, the model showed that, for the Glasgow to Edinburgh line, the total number of track circuits with the potential to experience "wrong side" failures increased very slightly from the $4\,\mathrm{V\,km^{-1}}$ value, while the number of "right side" failures increased a greater extent. For the Preston to Lancaster section of the WCML, the number of potential "wrong side" failures has already peaked at the $4\,\mathrm{V\,km^{-1}}$ value, with the number of "right side" failures increasing slightly.

Chapter 6

Extreme Storm Analysis

The following chapter contains published work from the article:
Patterson, C. J., Wild, J. A., Beggan, C. D., Richardson, G. S., & Boteler, D. H. (2024). Modelling electrified railway signalling misoperations during extreme space weather events in the UK. *Scientific Reports*, *14*(1583). https://doi.org/10.1038/s41598-024-51390-3

Space weather has the potential to impact ground-based technologies on Earth, affecting many systems including railway signalling. This chapter describes the use of the model detailed in the previous two chapters to analyse the impact of geomagnetically induced currents on railway signalling systems in the United Kingdom during the March 1989 and October 2003 geomagnetic storms. The March 1989 storm is also scaled to estimate a 1-in-100 year and a 1-in-200 year extreme storm. Both the Glasgow to Edinburgh line, and the Preston to Lancaster section of the West Coast Main Line are modelled. No "right side" failures (when unoccupied sections appear occupied) are suggested to have occurred during either storm, and the total number of potential "wrong side" failures (when occupied sections appear clear) is low. However, the modelling indicates "right side" and "wrong side" failures are possible on both routes during the 1-in-100 year and 1-in-200 year extreme storms, with the Glasgow to Edinburgh line showing more total misoperations than the Preston to Lancaster section of the West Coast Main Line. A 1-in-100 year or

1-in-200 year extreme storm would result in misoperations over an extended period of time, with most occurring over a duration of 2-3 hours either side of the peak of the storm.

6.1 Introduction

In this chapter, we use the model detailed in Chapters 4 and 5, based on earlier theoretical work (Boteler, 2021) and adapted for the UK, to analyse the impacts of GICs on two UK railway network routes: the generally east-west orientated Glasgow to Edinburgh via Falkirk line and the north-south orientated Preston to Lancaster section of the WCML, both shown in Figure 4.1 and Figure 6.1 showing the surrounding electric fields during a snapshot of the March 1989 storm. Firstly the model is used to estimate misoperations that could have occurred during the March 1989 and October 2003 storms, using electric field data generated from a thin-sheet conductivity model covering the UK (Beamish, 2013; Beamish and White, 2012). The strength of the electric field parallel to the rails for both storms near the middle of the Glasgow to Edinburgh line and the Preston to Lancaster section of the WCML are shown in Figure 6.2. The component of the electric field parallel to the blocks was extracted from these values. Secondly, the March 1989 storm is scaled by a factor of 2 to estimate a 1-in-100 year extreme storm and by 4 for a 1-in-200 year extreme storm. This scaling was based on initial extreme value analysis of the magnetotelluric transfer functions for LER, ESK and HAD, and from results derived in Kelly et al. (2017) and Thomson et al. (2011). The same analysis is then performed for these extreme storm estimates. Finally, the timing of the misoperations is examined to determine the duration in which misoperations might occur during the extreme storm estimates.

The results presented here are a first version of the analysis of the impacts of geomagnetically induced currents on railway signalling systems using more realistic variations of the geoelectric field rather than the simple uniform field in Chapters

4 and 5. This will be refined as the measurement and modelling of the geoelectric field and the rail network are improved over the next few years.

6.2 Methods

6.2.1 Electric Field Data

The modelled electric field data used in this study consist of a series of snapshot maps of the north and east components of geoelectric field computed on a 131×179 grid, each cell being approximately 10 by 10 km, covering the UK, Ireland and North Atlantic. Using the Spherical Elementary Current Systems (SECS) method (Beggan, Ciarán D. et al., 2021; McLay and Beggan, 2010), minute-mean magnetic data from multiple observatories and variometers were used to extrapolate the field across each cell. For the March 1989 storm, four observatories and one variometer were used (Lerwick [LER], Eskdalemuir [ESK], Hartland [HAD], Wingst and Glenmore Lodge). For October and November 2003, there were nine observatories and variometers available (Valentia, Faroes, Crooktree, York, and previous). A thin-sheet modelling code was used to compute the geoelectric field from rate of change of the X and Y components of the magnetic field ($\mathrm{dB}_x/\mathrm{dt}$ and $\mathrm{dB}_y/\mathrm{dt}$). The thin-sheet model consists of a 1D resistivity model at depth (down to 1000 km) on top of which lies a 2D model of the surface conductance, which redistributes the induced geoelectric field along lateral contrasts in conductance, particularly coastlines or resistive geological regions. The thin-sheet code uses a single frequency (or period) so provides a strongly band-passed version of the true geoelectric field (Beggan, 2015). To match the Nyquist frequency of the magnetic field data (2 minutes), the geoelectric field was computed every 2 minutes (720 samples per day) which ensures the more rapid variations are captured while meeting the numerical limits of the modelling code, and also allowing a geomagnetic storm to run in a reasonable amount of time. The output of the thin-sheet code has been compared against geoelectric field measurements at HAD observatory. The magnitude and phase

match reasonably well, though the model tends to underestimate the geoelectric measurements at ESK. HAD was chosen as the best site to match the geoelectric field to, as ESK, while being geographically closer to the lines being studied, is locally affected by a known mid-crustal anomaly, so is not representative of the region as a whole. For both the Glasgow to Edinburgh line and the Preston to Lancaster section of the WCML, the electric field strength for the cell that each track circuit block occupies was extracted to allow spatial variability in the track circuit model. The orientation of the rail in each block was then used alongside the north and east components of the geoelectric field to compute the parallel component along the rail. The extreme storms studied in this paper were scaled from the March 1989 storm by a factor of 2 for the 1-in-100 year storm and a factor of 4 for the 1-in-200 year storm, as noted above. However, there is no clear definition of what an extreme storm return period is, so these scaling factors are only meant to loosely reflect the range of what a 1-in-100 and 1-in-200 year event could experience. In future, the geoelectric field will be estimated from MT transfer functions measured at over 75 sites in the UK which will help improve estimates of the hazard posed and to provide better local modelling of the geoelectric field.

6.3 Results

6.3.1 Historic Storms

Two of the largest geomagnetic storms in the past 40 years were analysed in this study: 13-14 March 1989 and 29-31 October 2003. These storms were responsible for large impacts to power grids across the world (Bolduc, 2002; Boteler, 2019; Pulkkinen et al., 2005). Storms on 24 November 2003 and 7-8 September 2017 were also modelled but showed no misoperations, so they are not examined further. These storms were chosen due to them being the largest and most notable in terms of impacts in recent decades.

The total numbers of “right side” and “wrong side” failures in all of the 70 track

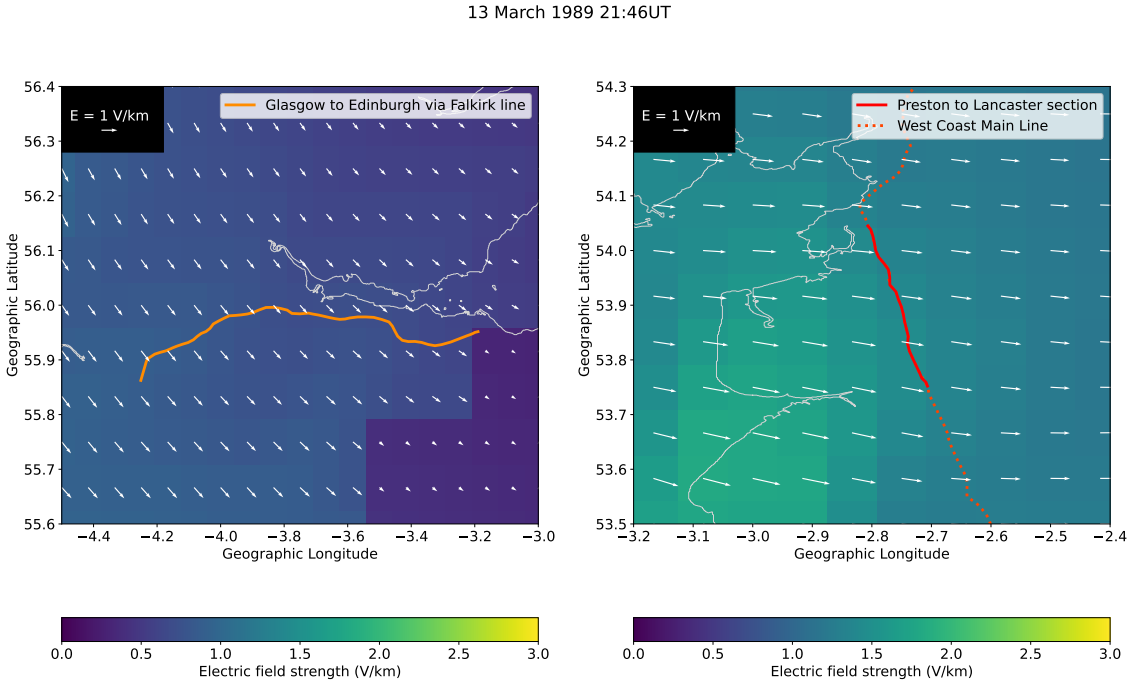

Figure 6.1: Geographic maps of sections of the UK surrounding the Glasgow to Edinburgh via Falkirk line (left) and the Preston to Lancaster section of the West Coast Main Line (right). The underlying colours give the magnitude of the geoelectric field in each grid cell for a peak value of the March 1989 storm on 13 March 1989 at 21:46UT, while the white vectors give the direction of the geoelectric field. The lengths of the white vectors also indicate the magnitude of the geoelectric field, with a scale given in the top left of both panels.

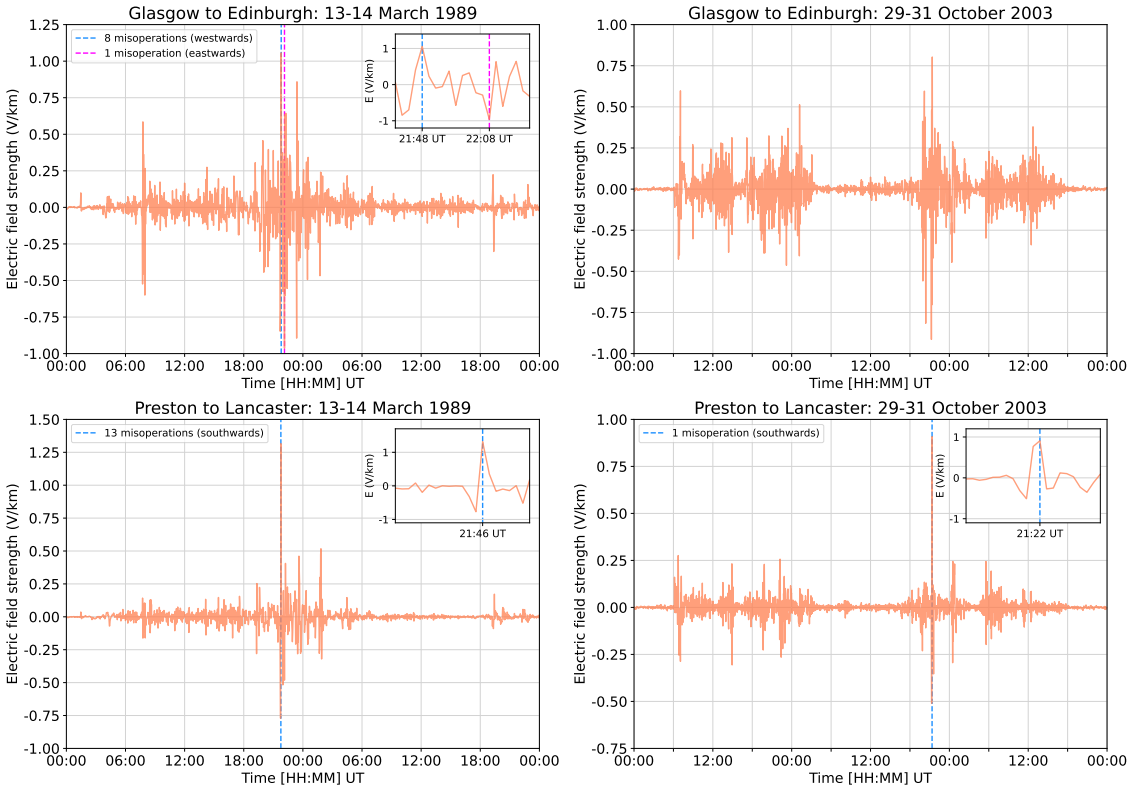

Figure 6.2: The electric field parallel to the rails near the centre of the Glasgow to Edinburgh line and the Preston to Lancaster section of the West Coast Main Line during the March 1989 and October 2003 storms. The Glasgow to Edinburgh line is generally east-west orientated, and the Preston to Lancaster section of the West Coast Main Line is generally north-south orientated. The dashed blue and red lines show the times that misoperations occurred on those lines, with the total number of misoperations and the direction of travel they occurred in shown in the top left. The smaller panels in the top right show the same data but for a shorter time period, allowing for closer examination of the features within that region.

circuit blocks in the Glasgow to Edinburgh line for the duration of each storm were modelled. The results suggest that no "right side" failures would have occurred in either direction of travel during either storm. Figure 6.3 shows that for the March 1989 storm, there would have been the potential for 1 "wrong side" failure in the eastwards direction of travel (Figure 6.3a), occurring at 13 March 1989 22:08UT, and 8 in the westwards direction of travel (Figure 6.3b), occurring at 13 March 1989 21:48UT. For the October 2003 storm, the model indicates that no "wrong side" failures would have occurred in either direction of travel.

This analysis was repeated for the Preston to Lancaster section of the WCML. Similar to the Glasgow to Edinburgh line, the model suggests that no "right side" failures would have occurred in any of the 25 track circuit blocks in either direction of travel during both storms. For the March 1989 storm, there would have been no "wrong side" failures in the northwards direction of travel and 13 "wrong side" failures in the southwards direction of travel (Figure 6.3c), occurring at 13 March 1989 21:46UT. For the October 2003 storm, the model suggests that no "wrong side" failures would have occurred in the northwards direction of travel and a single "wrong side" failure in the southwards direction of travel (Figure 6.3d), occurring at 30 October 2003 21:22UT.

6.3.2 Extreme Storms

The geoelectric field values estimated for the March 1989 storm were scaled up by a factor of 2 to provide a time-varying example of the electric fields during a 1-in-100 year extreme geomagnetic storm and a factor of 4 for a 1-in-200 year extreme geomagnetic storm. These values were then input into the model to provide an estimate for the number of "right side" and "wrong side" failures we might expect to see during storms of these magnitudes. Figure 6.4 shows the total number of both misoperation types for the Glasgow to Edinburgh line. Throughout the 1-in-100 year extreme storm, the model suggests there would be 4 "right side" failures and 232 "wrong side" failures in the eastwards direction of travel, and no "right

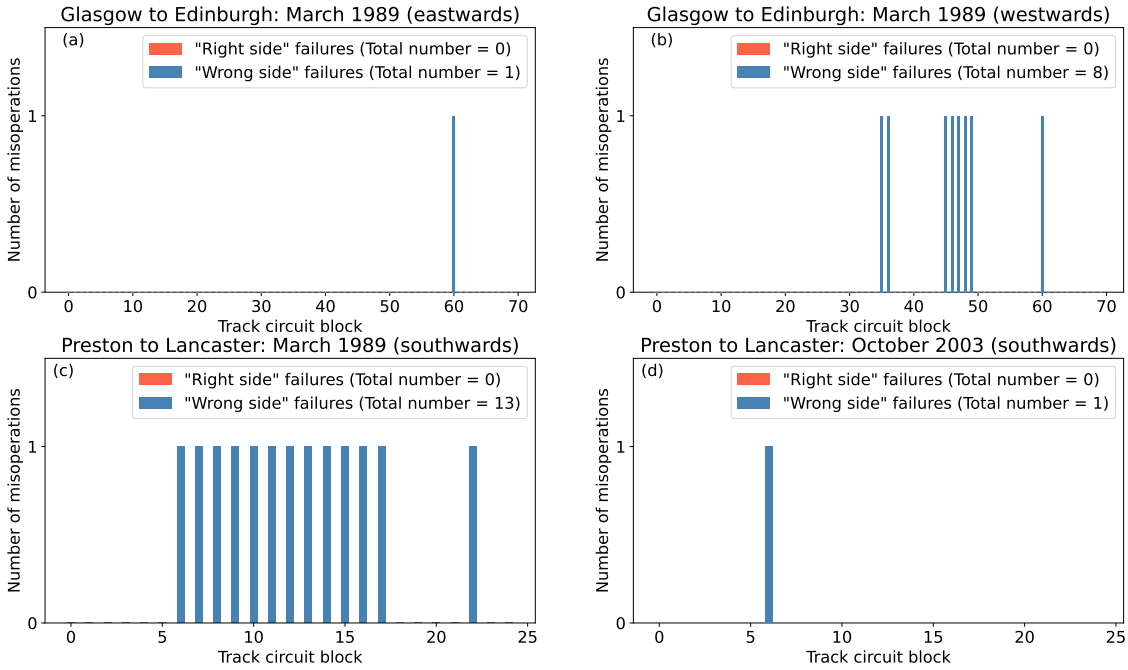

Figure 6.3: The total number of signal misoperations along the Glasgow to Edinburgh line during (a) the March 1989 storm in the eastwards direction of travel, and (b) the March 1989 storm in the westwards direction of travel. Glasgow is at block 0 for both directions of travel. The results for the Preston to Lancaster section of the WCML are also shown for during (c) the March 1989 storm in the southwards direction of travel, and (d) the October 2003 storm in the southwards direction of travel. Preston is at block 0 for both directions of travel.

side" failures and 149 "wrong side" failures in the westwards direction of travel. For the 1-in-200 year extreme storm, the number of misoperations increases to 52 "right side" failures and 963 "wrong side" failures in the eastwards direction of travel, and 39 "right side" failures and 775 "wrong side" failures in the westwards direction of travel.

Figure 6.5 shows the total number of both misoperation types for the Preston to Lancaster section of the WCML. For the 1-in-100 year extreme storm, the model suggests there would be no "right side" failures in either direction of travel, however there is the potential for 18 "wrong side" failures in the northwards direction of travel, and 25 "wrong side" failures in the southwards direction of travel. For the 1-in-200 year extreme storm, the model suggests there would be 18 "right side" failures and 82 "wrong side" failures in the northwards direction of travel, and 3 "right side" failures and 140 "wrong side" failures in the southwards direction of travel.

6.3.3 Time Series Analysis

Considering the number of misoperations by when they occurred rather than in which block (as in Figure 6.3), the temporal spread of misoperations throughout the storm can be analysed. Note that UT is close to magnetic local time in the UK. Focusing on the extreme storm estimates, Figure 6.6 shows the total number of "right side" and "wrong side" failures for each 2-minute time period that the data covers for the Glasgow to Edinburgh line. For the 1-in-100 year extreme storm, "right side" failures are expected to occur just before 22:00UT and shortly after 23:00UT in the eastwards direction of travel (Figure 6.6a), with only a couple of occurrences at each time, while no "right side" failures occur in the westwards direction of travel (Figure 6.6b). "Wrong side" failures are shown to occur in smaller numbers around 08:00UT and more frequently 21:00UT and 02:00UT in both the eastwards and westwards directions of travel. For the 1-in-200 year extreme storm, there are now instances of "right side" failures occurring in both the eastwards direction of travel (Figure

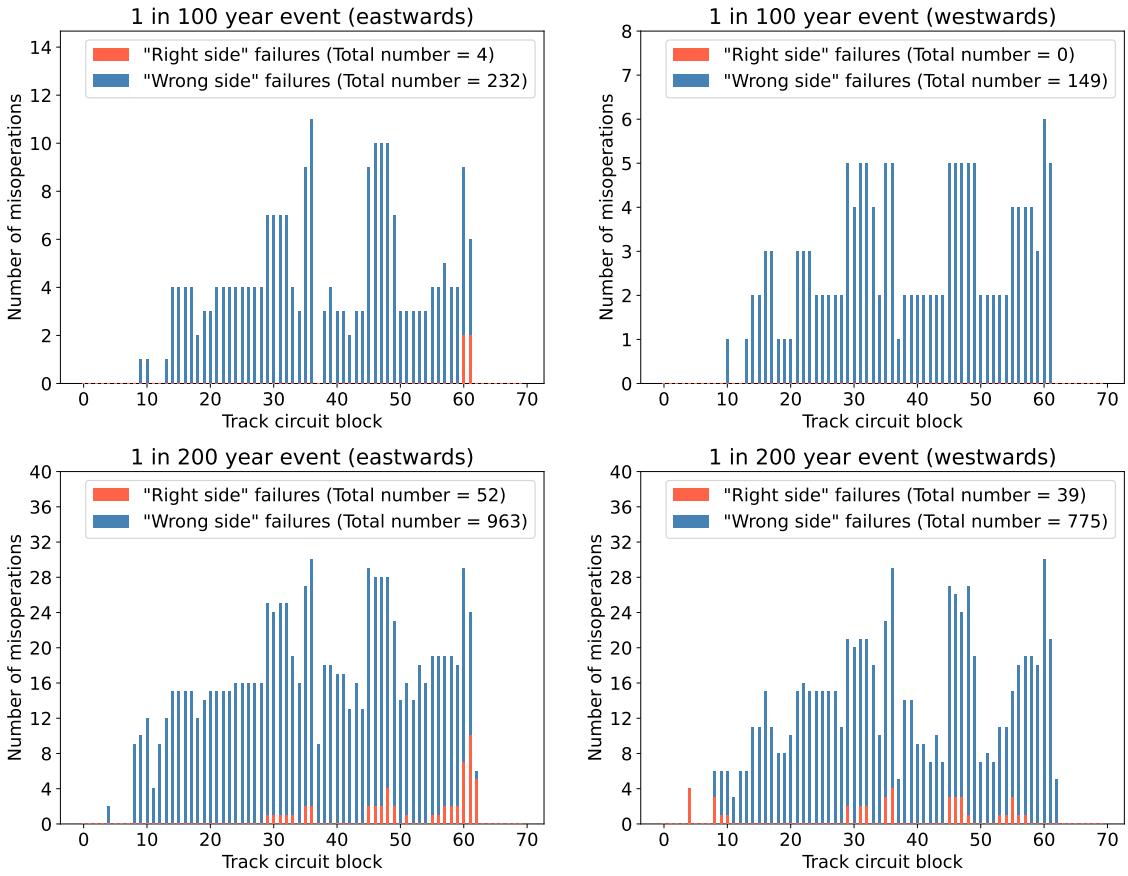

Figure 6.4: Glasgow to Edinburgh: the total number of signal misoperations in each track circuit block in the eastwards direction of travel and the westwards direction of travel during a 1-in-100 year extreme event and a 1-in-200 year extreme event.

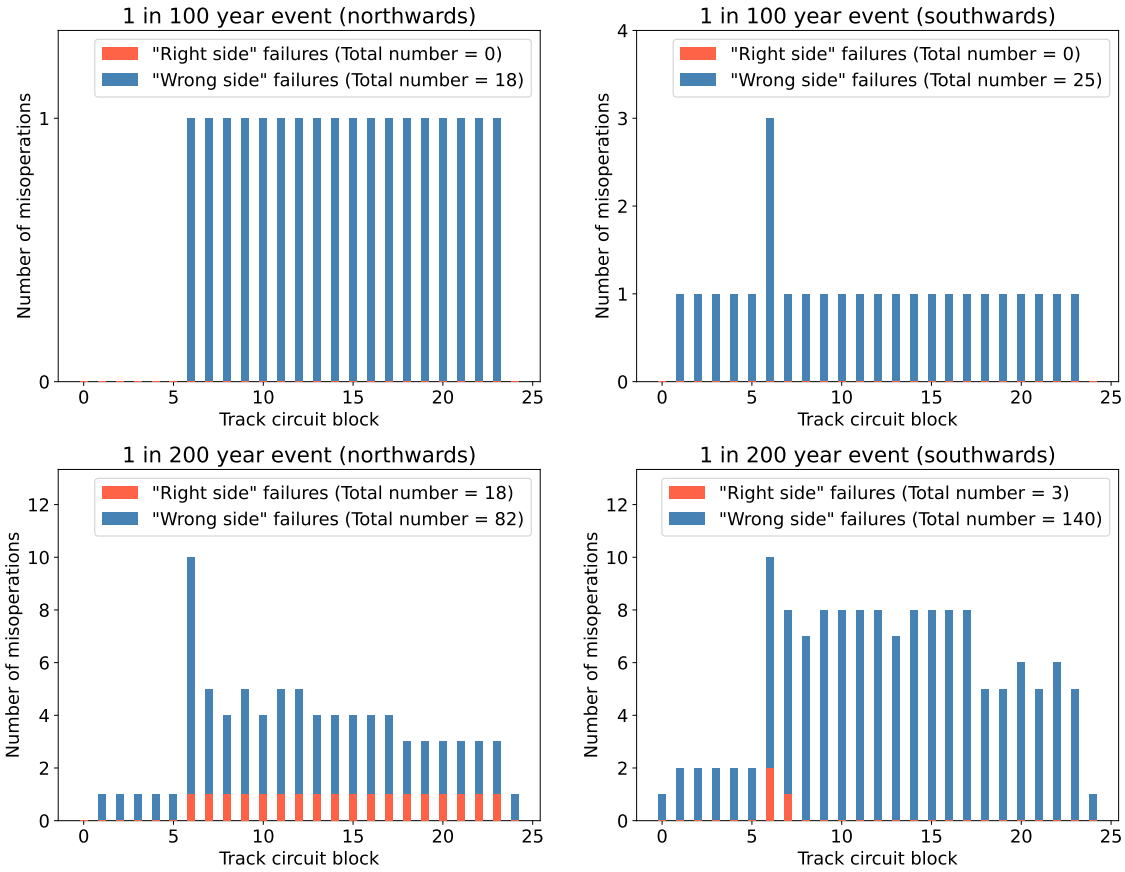

Figure 6.5: Preston to Lancaster: the total number of signal misoperations in each track circuit block in the northwards direction of travel and the southwards direction of travel during a 1-in-100 year extreme event and a 1-in-200 year extreme event.

6.6c) and westwards direction of travel (Figure 6.6d). In the eastwards direction of travel, there are now "right side" failures at 08:00UT and an increased number of "right side" failures between 20:00UT and 00:00UT. "Wrong side" failures have the potential to occur far more often during the 1-in-200 year extreme storm than the 1-in-100 year extreme storm, and the period they occur in has expanded to between 19:00UT and 02:00UT, with new occurrences around 14:00UT in the westwards direction of travel. The misoperations around 08:00UT correspond to the signature of a substorm.

The results for the Preston to Lancaster section of the WCML are shown in Figure 6.7. For the 1-in-100 year extreme storm, there are no "right side" failures northwards or southwards directions of travel. There are "wrong side" failures just prior to 22:00UT in both directions of travel, and some around 23:30UT and 02:00UT in the southwards direction of travel. For the 1-in-200 year extreme storm, there are "right side" failures in both directions of travel at around 22:00UT. "Wrong side" failures generally occur just after 19:00UT, around 22:00UT, between 23:00UT and 00:00UT, and just before 02:00UT.

6.4 Discussion

The model suggests that for the March 1989 storm, there was the possibility for a number of "wrong side" failures to have occurred, mostly in the westwards and southwards directions of travel for each line respectively, as shown in Figure 6.3. This is due to the peak strength of the electric field parallel to the rails being larger in the positive direction than the negative direction, as shown in Figure 6.2, and a positive electric field drives "wrong side" failures in the westwards and southwards directions of travel (Patterson et al., 2023b). For the October 2003 storm, the model suggests that there were no misoperations on the Glasgow to Edinburgh line, and only the potential for a single "wrong side" failure on the Preston to Lancaster section of the WCML, occurring in block 6. This block is the longest in the Preston

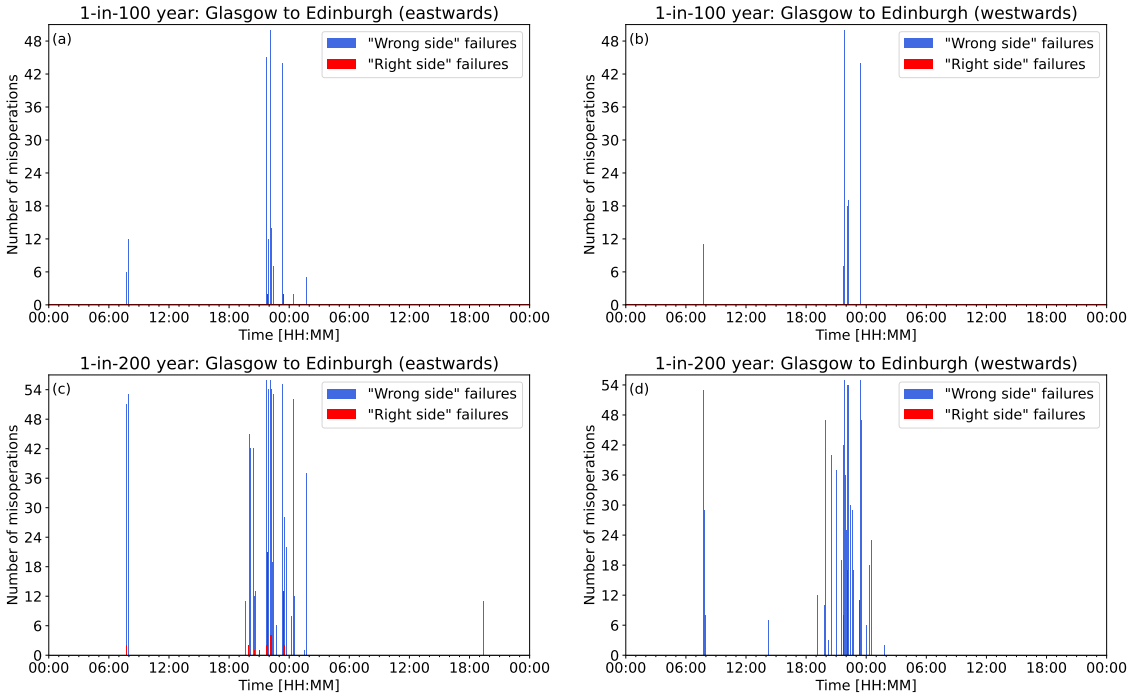

Figure 6.6: Glasgow to Edinburgh: the total number of signal misoperations at each 2-minute interval in (a) the eastwards direction of travel and (b) the westwards direction of travel during a 1-in-100 year extreme event, and in (c) the eastwards direction of travel and (d) the westwards direction of travel during a 1-in-200 year extreme event.

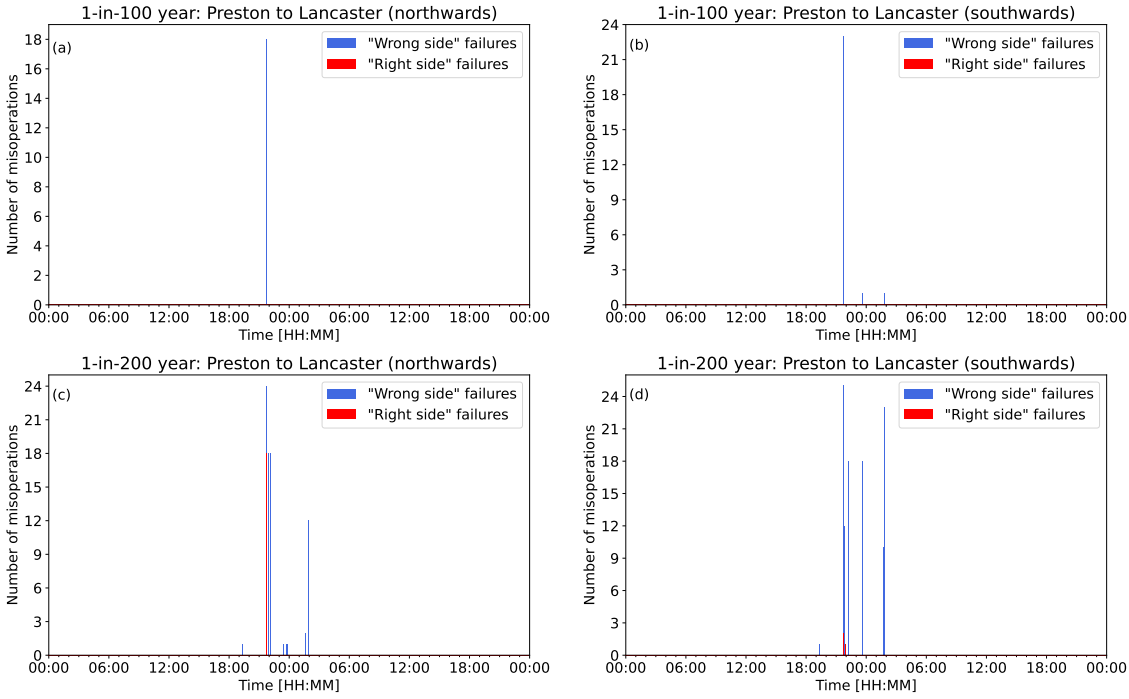

Figure 6.7: Preston to Lancaster: the total number of signal misoperations at each 2-minute interval in (a) the northwards direction of travel and (b) the southwards direction of travel during a 1-in-100 year extreme event, and in (c) the northwards direction of travel and (d) the southwards direction of travel during a 1-in-200 year extreme event.

to Lancaster section of the WCML, and thus is the most susceptible to misoperation (Patterson et al., 2023a). Also, the positive peak of the northwards electric fields of the October 2003 storm was larger than the negative, which is why the "wrong side" failures occur in the southwards direction of travel but not the northwards direction of travel. The model suggests that for both sections, no "right side" failures would have occurred during either of the storms analysed in the study. It is not unexpected for no "right side" failures to occur even though there is the potential for "wrong side" failures, as the electric field strength required for "right side" failures to occur is higher than for "wrong side" failures (Patterson et al., 2023b). It is important to note that "wrong side" failures can only occur when a train is occupying a block, and the strength of the geoelectric field needed to cause a misoperation is dependent on the distance the train has travelled through said block (Patterson et al., 2023b). Therefore, even though there is the potential for a "wrong side" failure, it does not equate to a definite misoperation. It is difficult to validate whether misoperations actually occurred, as records of railway anomalies are often not digitised and since misoperations caused by space weather do not damage equipment, events may go undocumented. This highlights the importance for railway operators and engineers to log all anomalies, even those that seem to have no obvious cause.

During a 1-in-100 year and 1-in-200 year extreme storm, the Glasgow to Edinburgh line could experience both misoperation types, as shown in Figure 6.4. The number of "right side" failures falls short of the number of potential "wrong side" failures, which indicates that storms of this magnitude have the potential to both cause disruption and lead to a hazardous situation. Figure 6.5 shows the results for the Preston to Lancaster section of the WCML, with the total number of misoperations being far fewer than for the Glasgow to Edinburgh line. This is not only due to the respective length of each line and corresponding number of blocks, but also because the electric field is on average weaker in more southern locations. This is demonstrated in Figure 6.2, where even though the peak positive electric field during the March 1989 storm is larger at the Preston to Lancaster section of

the WCML than at the Glasgow to Edinburgh line, the other fluctuations on either side of the peak are larger overall at the Glasgow to Edinburgh line. It can be seen that for the Glasgow to Edinburgh line, the misoperations seem to not impact blocks at the start and end of the line, but within the Preston to Lancaster section of the WCML there are misoperations throughout. This difference is due to the Glasgow to Edinburgh line being a complete line and blocks at the end of the line are more resilient to the impacts of GICs (Patterson et al., 2023a), whereas Preston to Lancaster is only a section of the longer WCML, and so the start and end of that section are not truly the ends of the line. It should be acknowledged that differences in the geomagnetic storm signal can lead to significant differences in the number of misoperations observed. A future study could examine the impact of this, perhaps by means of superposed epoch analysis.

One source of variability in these results is the rails' leakage, which can change depending on environmental conditions, increasing with wetter weather and decreasing with drier weather. These changes impact how susceptible the track circuits are to GICs, with the potential for misoperation being higher in wetter conditions and vice-versa. While in this study we have assumed moderate leakage, the analysis was repeated for both wet and dry conditions (given in Table 1). As expected, the model suggested a higher number of misoperations could occur during wetter conditions, including cases where it was previously suggested there would be no misoperations. In drier conditions, the total number of misoperations that could occur decreased. For example, no "right side" failures were suggested to occur on either route during both the March 1989 and October 2003 storms under moderate leakage conditions. However, under maximum leakage conditions, the total number of "right side" failures suggested to occur during both storms on both routes increased to 90. For the 1-in-100 year extreme storm, at maximum leakage conditions, the total number of "right side" failures across both routes increased from 4 to 503; for the 1-in-200 year extreme storm, there was an increase from 112 to 2194. As the threshold for "wrong side failure" is not as impacted by changes to

leakage, it is expected that while there would be some increase, it would not be as significant as the "right side" failures results (Patterson et al., 2023b).

The number of misoperations over the course of a 1-in-100 year and 1-in-200 year extreme storm for both the Glasgow to Edinburgh line and the Preston to Lancaster section of the WCML are shown in Figures 6.6 and 6.7. Most misoperations in the extreme events considered here occur within a few hours before and after local midnight. This is because the main phase of the 1989 storm (on which the extreme storms are based) peaked just prior to midnight of 13/14 March, with the Dst index approaching -600 nT at that time and magnetic disturbances in the UK peaking in the hours that followed due to the southward expansion of the auroral oval and associated electrojets to mid-latitudes (Boteler, 2019). In this scenario, most misoperations would occur outside of peak railway operating hours. Also, since there are fewer trains on the line during those periods, the probability of a "wrong side" failure arising is lower. However, geomagnetic disturbances at any particular place will vary with local time as the Earth's rotation carries that location through the disturbed region on the night side of the Earth. This means storms can occur at any time, and could last for multiple days. Thus, greater consideration should be given to the total duration of the spread of the misoperations, rather than the specific time itself. The model suggests that for both the Glasgow to Edinburgh line and the Preston to Lancaster section of the WCML, there are short periods where multiple misoperations could occur, separated by periods of no misoperations. Misoperations could potentially impact signalling systems over a period of 2-3 hours on either side of the peak of the storm. This prolonged disruption to the network could cause delays and increases the potential for a hazardous situation to occur. Though no storm has the same profile as another, our modelling suggests that an extreme geomagnetic storm has the potential to impact UK railway signalling systems.

Chapter 7

Summary and Future Work

In this thesis, a realistic model of geomagnetic interference on DC track circuit railway signalling systems on AC electrified lines in the UK is presented. Two routes were considered - the Preston to Lancaster section of the West Coast Main Line and the Glasgow to Edinburgh via Falkirk line. For each route, misoperation modes were studied with constant uniform electric fields applied and time-varying electric fields during historic storms and extreme storm estimates.

In Chapter 4, the focus is on "right side" failures, the misoperation mode that occurs when a green signal for a block that is not occupied by a train is turned red due to the energised relay being de-energised. A range of uniform electric fields (northwards for the Preston to Lancaster section of the WCML and eastwards for the Glasgow to Edinburgh via Falkirk line) were applied to the model of both routes to find the minimum required electric field strength to cause "right side" failures. These values were found to be $E_y = 1.9\,\mathrm{V\,km^{-1}}$ for the eastwards direction of travel, and $E_y = -2.8\,\mathrm{V\,km^{-1}}$ for the westwards direction of travel of the Glasgow to Edinburgh via Falkirk line, and $E_x = 2.7\,\mathrm{V\,km^{-1}}$ for the the northwards direction of travel, and $E_x = -2.5\,\mathrm{V\,km^{-1}}$ for the southwards direction of travel of the Preston to Lancaster section of the WCML. A storm that could generate electric fields of this magnitude are estimated to occur once every 30 years.

The electric field was then increased to $\pm 4\,\mathrm{V\,km^{-1}}$, a value known to have

impacted railway signalling systems in Sweden during storm in July 1982, and $\pm 5\,\mathrm{V\,km^{-1}}$, an estimate of a 1-in-100 year extreme storm. The model suggested that at electric fields of this magnitude, many misoperations would occur across both routes.

It was also found that when modelling a section of a line versus a line in its entirety, it is important to correctly handle how ends of the section are modelled due to how the voltage profile changes at those termination points. If the model covers the entire line, no extra steps need to be taken. However, if only a section of a line is modelled, equivalent components need to be added to end to represent the external parts. The length of the track circuit blocks was shown to be a first-order indicator of the magnitude of GICs when considering blocks at the centre of the line, with the magnitude of the component of the electric field parallel to the rails of each block also having a significant effect.

Chapter 5 focuses on "wrong side" failures, the misoperation mode that could lead to human harm, when a red signal indicating that a block is occupied by a train is turned green due to GICs re-energising the de-energised relay, potentially causing a train collision. In this case, we are considering blocks that are occupied by trains, and it was found that the position of the train within the block (the distance between the rearmost axle and the relay) has an effect on the magnitude of GICs able to interfere with relay operation. As such, it is assumed that trains are always positioned at the ends of the blocks to model the largest impact. It is also important to note that not every block will be occupied by a train simultaneously, and traffic density varies over time. Collectively, this means that when discussing the total number of "wrong side" failures, this refers to the total number of relays that have the potential to misoperate, rather than the total number that would be observed.

A range of uniform electric fields (northwards for the Preston to Lancaster section of the WCML and eastwards for the Glasgow to Edinburgh via Falkirk line) were applied to the model of both routes to find the minimum required electric field strength to cause "wrong side" failures. These values were found to be $E_y =$

$-1.0\,\mathrm{V\,km^{-1}}$ for the eastwards direction of travel, and $E_y = 1.0\,\mathrm{V\,km^{-1}}$ for the westwards direction of travel of the Glasgow to Edinburgh via Falkirk line, and $E_x = -1.1\,\mathrm{V\,km^{-1}}$ for the the northwards direction of travel, and $E_x = 1.1\,\mathrm{V\,km^{-1}}$ for the southwards direction of travel of the Preston to Lancaster section of the WCML. A storm that could generate electric fields of this magnitude are estimated to occur once every 10 to 20 years. Also examined was how these threshold values vary with changes to leakage due to weather conditions. For "right side" failures, the thresholds can vary quick significantly near the ends of the line, but for "wrong side" failures, the thresholds do not significantly change.

When an electric field of $\pm 4\,\mathrm{V\,km^{-1}}$ was applied to both sections, the relays in 55 out of the 70 blocks on the Glasgow to Edinburgh line and all of the blocks along the Preston to Lancaster section of the WCML had the potential to experience "wrong side" failure. At the 1-in-100 year extreme electric field estimate of $\pm 5\,\mathrm{V\,km^{-1}}$, along the Glasgow to Edinburgh line, 56 blocks in the eastwards direction and 57 blocks in the westwards direction could potentially experience "wrong side" failure. It was also shown that where "wrong side" failures would occur in one direction of travel, "right side" failures would occur in the opposite direction. This would then reverse when the orientation of the electric field was reversed.

In Chapter 6, both misoperation modes were modelled for two of the largest geomagnetic storms of the past several decades, March 1989 and October 2003, and for 1-in-100 year and 1-in-200 year extreme storm estimates based on a 2-times and 4-times scaling of the March 1989 storm respectively.

For the historic storms, the model suggested that, for both storms, no "right side" failures would have occurred on either route. For the March 1989 storm, there was the potential for 1 "wrong side" failure in the eastwards direction of travel and 8 in the westwards direction of travel for the Glasgow to Edinburgh line, and no "wrong side" failures in the northwards direction of travel and 13 in the southwards direction of travel for the Preston to Lancaster section of the WCML. For the October 2003 storm, no "wrong side" failures were suggested to have occurred along the Glasgow

to Edinburgh line, however there was the potential for 1 "wrong side" failure along the southwards direction of travel of the Preston to Lancaster section of the WCML.

For the extreme storms estimates, these values are significantly higher. The model suggested that the estimate of the 1-in-100 year extreme storm would have the potential to cause 4 "right side" failures and 232 "wrong side" failures in the eastwards direction of travel and no "right side" failures and 149 "wrong side" failures in the westwards direction of travel of the Glasgow to Edinburgh line. For the Preston to Lancaster section of the WCML, no "right side" failures were suggested to occur. However, there would be the potential for 18 and 25 "wrong side" failures in the northwards and southwards directions of travel respectively. For the 1-in-200 year extreme storm estimate, the number of misoperations for the Glasgow to Edinburgh line increases to 52 "right side" failures and 963 "wrong side" failures in the eastwards direction of travel, and 39 "right side" failures and 775 "wrong side" failures in the westwards direction of travel. The total misoperations along the Preston to Lancaster section of the WCML increases to 18 "right side" failures and 82 "right side" failures in the northwards direction of travel, and 3 "right side" failures and 140 "wrong side" failures in the southwards direction of travel. It was also shown that the total number of misoperations can vary significantly with different leakage values due to weather conditions.

The spread of misoperations with time was also analysed, and it was shown that most misoperations occur within 2 to 3 hours either side of the peak of the storm, with a small number of other clusters outside that range for the Glasgow to Edinburgh line.

7.1 Future Work

The next logical step would be to expand this model to cover other AC electrified lines that use DC track circuits in the UK to establish whether the results for the two routes studied are typical across the wider network and whether there are parts of

the network that are particularly resilient/vulnerable to geomagnetic disturbances due to local network configuration or underlying geology. Over time, this could be combined with real-time electric field data or forecasts to provide railway network operators with a warning of potential geomagnetic disturbances to specific sections. As such, to obtain better local modelling of the geoelectric field, the number of magnetotelluric transfer functions should be expanded.

When considering the effects that changes to leakage due to weather conditions have on the susceptibility of signalling systems to geomagnetic disturbances, with climate change expected to lead to a warmer and wetter weather in the UK and elsewhere, track circuit susceptibility to space weather could change over time. It would be worth considering in future work just how much wetter would a typical UK winter be and what impact will that have on leakage/threshold electric field values required for misoperations.

As this thesis is focused on modelling, it is also crucial that we move towards validating it by practical means. This could be achieved by placing equipment within the track circuit system to monitor and record current levels. As the ability to forecast space weather events is limited, the equipment would likely have to remain in place for an extended period of time to capture moderate to strong events. The feasibility of placing additional equipment into a mainline railway's systems also depends on whether authorisation from the relevant rail operators and regulators could be obtained. Assuming that it is impractical for monitoring equipment to be installed in all track circuits, then the modelling techniques we have demonstrated in this study could be used to identify the optimal deployment of monitoring instruments. There is also the potential to utilise a heritage or test railway line to perform these studies, provided configurations are comparable to lines modelled. An alternative could be to perform a statistical survey similar to the aforementioned Eroshenko et al. (2010), Kasinskii et al. (2007), and Ptitsyna et al. (2008), where a comparison is made between geomagnetic activity and signalling misoperations. One of the challenges with this is that it is assumed that space weather related

signalling misoperations would not be recorded as such, as space weather is not a generally well-known cause of signalling issues among railway engineers. This means the study would likely need to be based on whether the total number of misoperations increases during space weather events, rather than relying on the reporting personnel correctly identifying space weather as the specific issue.

The modelling work in this thesis has focused on geomagnetic disturbances to DC track circuits on AC electrified lines. While there are still a large number of these being used across the UK railway network, as routes are being modernised, DC track circuits are being replaced with newer, modern systems. These systems may not necessarily be susceptible to geomagnetically induced currents, however, as radio communications and GNSS become more integrated into the system, they become prone to other aspects of space weather. Further work should go into investigating the impacts to these systems. It is also important to point out that in the event of severe space weather, railway signalling will not be the only system affected. Power supply networks, communications, GNSS are all susceptible, many of which will also impact the safe and smooth operation of the railway network. Further study needs to focus on the connectivity of these systems, and the railway sector could be affected by the loss of interdependent systems (Darch et al., 2014; Hapgood et al., 2021).

Appendix A

Mathematical Proofs

A.1 DSTL Voltage and Current Solutions

The proof for the solutions to equations 3.29 and 3.28 is as follows. Starting with the voltage V, since $f(x) = 0$, this is a homogeneous second order partial differential equation. To solve this equation, the following substitutions are made

$$V = e^{rx}$$

$$\frac{\partial}{\partial x}V = re^{rx}$$

$$\frac{\partial^2}{\partial x^2}V = r^2e^{rx}$$

Substituting these values into equation 3.29 gives the characteristic equation

$$r^2e^{rx} - \gamma^2e^{rx} = 0$$

This can then be solved for r

$$e^{rx}(r^2 - \gamma^2) = 0$$

$$r^2 = \gamma^2$$

$$r_1 = \gamma$$

$$r_2 = -\gamma$$

Since the roots r_1 and r_2 are real and distinct, the general solutions of the equation are given by

$$V = Ae^{r_1 x} + Be^{r_2 x}$$

where A and B are determined by the conditions at the ends of the line. Substituting the values for r_1 and r_2 into the general solutions gives the expression for V

$$V = Ae^{\gamma x} + Be^{-\gamma x}$$

which is equation 3.30. Differentiating this equation gives

$$\frac{\partial}{\partial x}V = \gamma Ae^{\gamma x} - \gamma Be^{-\gamma x}$$

Substituting in equation 3.26 gives

$$E - ZI = \gamma Ae^{\gamma x} - \gamma Be^{-\gamma x}$$

Finally, rearranging for I and simplifying using the relationships in equations 3.8 and 3.9, we get

$$I = \frac{E}{\gamma Z_0} - \frac{A}{Z_0}e^{\gamma x} + \frac{B}{Z_0}e^{-\gamma x}$$

which is equation 3.31.

A.2 DSTL Parameters A and B

The proof for determining the parameters A and B, which depend on the conditions at the ends of the line, is given here. Starting by multiplying equation 3.32 by $e^{-\gamma L}$, we get

$$V_i e^{-\gamma L} = Ae^{-\gamma L} + Be^{-\gamma L}$$

Rearranging to

$$Be^{-\gamma L} = V_i e^{-\gamma L} - Ae^{-\gamma L}$$

and substituting into equation 3.34 gives

$$V_k = Ae^{\gamma L} + V_i e^{-\gamma L} - Ae^{-\gamma L}$$

Rearranging to

$$-A(e^{\gamma L} - e^{-\gamma L}) = -V_k + V_i e^{-\gamma L}$$
$$A = \frac{V_k - V_i e^{-\gamma L}}{e^{\gamma L} - e^{-\gamma L}}$$

which is equation 3.36.

Similarly, multiplying equation 3.32 by $e^{\gamma L}$, we get

$$V_i e^{\gamma L} = A e^{\gamma L} + B e^{\gamma L}$$

Rearranging to

$$A e^{\gamma L} = V_i e^{\gamma L} - B e^{\gamma L}$$

and substituting into equation 3.34 gives

$$V_k = V_i e^{\gamma L} - B e^{\gamma L} + B e^{-\gamma L}$$

Rearranging to

$$B(e^{\gamma L} - e^{-\gamma L}) = V_i e^{\gamma L} - V_k$$
$$B = \frac{V_i e^{\gamma L} - V_k}{e^{\gamma L} - e^{-\gamma L}}$$

which is equation 3.37.

A.3 DSTL Voltage and Current at the End of the Line

The proof for determining the voltage and current at the end of the line, V_k and I_k, in terms of the voltage and current at the start of the line, V_i and I_i, is given here. Starting with equation 3.34 and substituting the expressions for A and B given in equations 3.40 and 3.41, we get

$$V_k = \left[\frac{V_i}{2} - \frac{1}{2}(Z_0 I_i - \frac{E}{\gamma})\right] e^{\gamma L} + \left[\frac{V_i}{2} + \frac{1}{2}(Z_0 I_i - \frac{E}{\gamma})\right] e^{-\gamma L}$$

Rearranging to

$$V_k = \frac{1}{2}(V_i e^{\gamma L} - Z_0 I_i e^{\gamma L} + \frac{E}{\gamma} e^{\gamma L} + V_i e^{-\gamma L} + Z_0 I_i e^{-\gamma L} - \frac{E}{\gamma} e^{-\gamma L})$$

$$V_k = V_i(\frac{e^{\gamma L} + e^{-\gamma L}}{2}) - Z_0 I_i(\frac{e^{\gamma L} - e^{-\gamma L}}{2}) + \frac{E}{\gamma}(\frac{e^{\gamma L} - e^{-\gamma L}}{2})$$

and since $\cosh(x) = \frac{e^x + e^{-x}}{2}$ and $\sinh(x) = \frac{e^x - e^{-x}}{2}$, we can simplify to

$$V_k = V_i \cosh(\gamma L) - Z_0 I_i \sinh(\gamma L) + \frac{E}{\gamma} \sinh(\gamma L)$$

which is equation 3.42. For I_i, we similarly start by substituting the expressions for A and B given in equations 3.40 and 3.41 into equation 3.35, giving

$$I_k = -\frac{1}{Z_0}\left[\frac{V_i}{2} - \frac{1}{2}(Z_0 I_i - \frac{E}{\gamma})\right]e^{\gamma L} + \frac{1}{Z_0}\left[\frac{V_i}{2} + \frac{1}{2}(Z_0 I_i - \frac{E}{\gamma})\right]e^{-\gamma L} + \frac{E}{\gamma Z_0}$$

Rearranging to

$$I_k = \frac{1}{2}(-\frac{V_i}{Z_0}e^{\gamma L} + I_i e^{\gamma L} - \frac{E}{\gamma Z_0}e^{\gamma L} + \frac{V_i}{Z_0}e^{-\gamma L} + I_i e^{-\gamma L} - \frac{E}{\gamma Z_0}e^{-\gamma L} + \frac{2E}{\gamma Z_0})$$

$$I_k = -\frac{V_i}{Z_0}(\frac{e^{\gamma L} - e^{-\gamma L}}{2}) + I_i(\frac{e^{\gamma L} + e^{-\gamma L}}{2}) - \frac{E}{\gamma Z_0}(\frac{e^{\gamma L} + e^{-\gamma L}}{2} - 1)$$

and again since $\cosh(x) = \frac{e^x + e^{-x}}{2}$ and $\sinh(x) = \frac{e^x - e^{-x}}{2}$, we can simplify to

$$I_k = -\frac{V_i}{Z_0}\sinh(\gamma L) + I_i \cosh(\gamma L) - \frac{E}{\gamma Z_0}(\cosh(\gamma L) - 1)$$

which is equation 3.43.

A.4 Equivalent Pi-Circuit Voltage at the End of the Line

The proof for the expression of the voltage at the end of the line V_k in the equivalent pi-circuit representation in terms of the voltage and current at the start of the line, V_i and I_i, is given here. Using KCL at node A, shown in Figure A.1, gives

$$I_i = I_{AB} + I_A$$

$$I_{AB} = I_i - I_A$$

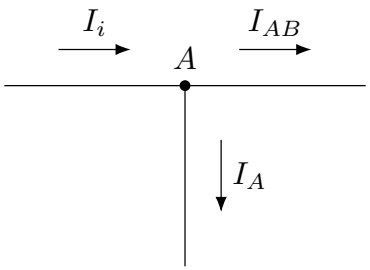

Figure A.1: The currents at node A of the equivalent pi-circuit representation of the transmission line of a rail shown in Figure 3.10.

Since we are considering DC track circuits, impedance Z is assumed to be equal to R, and since admittance Y is equal to the inverse of Z, these can be substituted into OL (equation 3.5) to give

$$V = \frac{I}{Y}$$

Using this relationship and KVL around the clockwise loop between $i(x = 0)$ and the left hand parallel admittance, shown in Figure A.2, we get

$$V_i - \frac{2I_A}{Y'} = 0$$

$$V_i = \frac{2I_A}{Y'}$$

Repeating this for the clockwise loop between $k(x = L)$ and the right hand parallel admittance, shown in Figure A.3, we get

$$\frac{2I_B}{Y'} - V_k = 0$$

$$V_k = \frac{2I_B}{Y'}$$

Again this for the clockwise loop between both parallel admittances, shown in Figure A.4, we get

$$\frac{2I_A}{Y'} - Z'I_{AB} + E' - \frac{2I_B}{Y'} = 0$$

Substituting in the expression for I_{AB} above, we get

$$\frac{2I_A}{Y'} - Z'(I_i - I_A) + E' - \frac{2I_B}{Y'} = 0$$

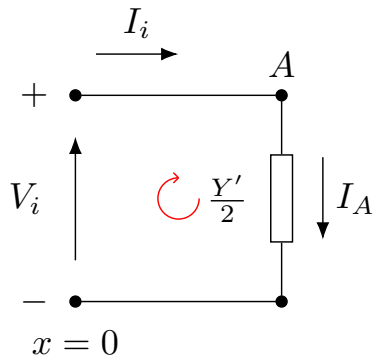

Figure A.2: KVL clockwise loop between $i(x = 0)$ and the left hand parallel admittance of the equivalent pi-circuit representation of the transmission line of a rail shown in Figure 3.10.

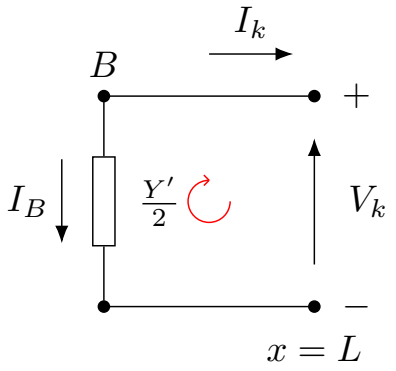

Figure A.3: KVL clockwise loop between $K(x = L)$ and the right hand parallel admittance of the equivalent pi-circuit representation of the transmission line of a rail shown in Figure 3.10.

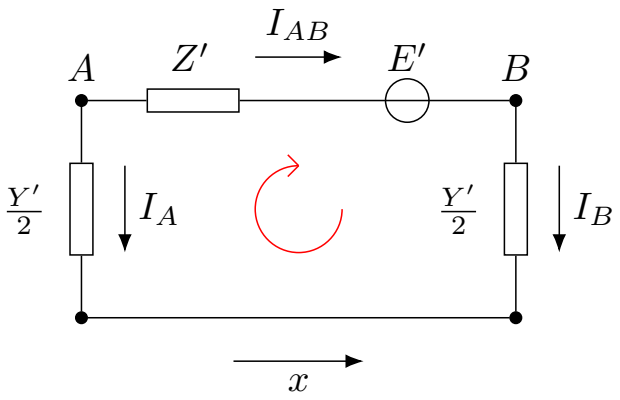

Figure A.4: KVL clockwise loop between both parallel admittances of the equivalent pi-circuit representation of the transmission line of a rail shown in Figure 3.10.

$$\frac{2I_A}{Y'} - Z'I_i - Z'I_A + E' - \frac{2I_B}{Y'} = 0$$

and since $I_A = \frac{Y'V_i}{2}$

$$\frac{2I_A}{Y'} - Z'I_i - \frac{Y'V_iZ'}{2} + E' - \frac{2I_B}{Y'} = 0$$

Substituting in the expressions for V_i and V_k gives

$$V_i - Z'I_i - \frac{Y'V_iZ'}{2} + E' - V_k$$

$$V_k = (1 + \frac{Y'Z'}{2})V_i - Z'I_i + E'$$

which is equation 3.44.

Appendix B

Misc

B.1 Nodal Admittance Matrix

The full nodal admittance matrix of the network shown in Figure 3.12, which is used in equation 3.62.

$$
\begin{bmatrix}
y_0 + y_{04} + y_{01} & -y_{01} & 0 & 0 & -y_{04} & 0 & 0 & 0 & 0 & 0 \\
-y_{01} & y_1 + y_{01} + y_{15} + y_{16} + y_{12} & -y_{12} & 0 & 0 & -y_{15} & 0 & 0 & 0 & 0 \\
0 & -y_{12} & y_2 + y_{12} + y_{27} + y_{28} + y_{23} & -y_{23} & 0 & 0 & 0 & -y_{27} & -y_{28} & 0 \\
0 & 0 & -y_{23} & y_3 + y_{23} + y_{39} & 0 & 0 & 0 & 0 & 0 & -y_{39} \\
-y_{04} & 0 & 0 & 0 & y_4 + y_{04} + y_{45} & -y_{45} & 0 & 0 & 0 & 0 \\
0 & -y_{15} & 0 & 0 & -y_{45} & y_5 + y_{45} + y_{15} & 0 & 0 & 0 & 0 \\
0 & -y_{16} & 0 & 0 & 0 & 0 & y_6 + y_{16} + y_{67} & -y_{67} & 0 & 0 \\
0 & 0 & -y_{27} & 0 & 0 & 0 & -y_{67} & y_7 + y_{67} + y_{27} & 0 & 0 \\
0 & 0 & -y_{28} & 0 & 0 & 0 & 0 & 0 & y_8 + y_{28} + y_{89} & -y_{89} \\
0 & 0 & 0 & -y_{39} & 0 & 0 & 0 & 0 & -y_{89} & y_9 + y_{89} + y_{39}
\end{bmatrix}
$$

References

Alfvén, H. (1942). Existence of electromagnetic-hydrodynamic waves. *Nature*, *150*(3805), 405–406. https://doi.org/10.1038/150405d0

Alm, E. (2020). Measures against geomagnetic disturbances in the entire DC track circuit for automatic signalling systems, original publication (in Swedish) appendix 5f, betänkande: Angående det tekniska utförandet av signalanläggningar vid statens järnvägar, 1956. Translation (in English). *Infrastructure Resilience Risk Reporter*, *1*, 10–27. https://carleton.ca/irrg/journal/

Baker, D. N., Pulkkinen, T. I., Angelopoulos, V., Baumjohann, W., & McPherron, R. L. (1996). Neutral line model of substorms: Past results and present view. *Journal of Geophysical Research: Space Physics*, *101*(A6), 12975–13010. https://doi.org/https://doi.org/10.1029/95JA03753

Barlow, W. H. (1849). On the spontaneous electrical currents observed in the wires of the electric telegraph. *Philosophical Transactions of the Royal Society of London*, *139*(1849), 61–72. https://www.jstor.org/stable/108470

Baumjohann, W., & Nakamura, R. (2007). 5.03 - magnetospheric contributions to the terrestrial magnetic field. In G. Schubert (Ed.), *Treatise on geophysics (second edition)* (Second Edition, pp. 79–90). Elsevier. https://doi.org/https://doi.org/10.1016/B978-0-444-53802-4.00097-X

Baumjohann, W., & Treumann, R. (1996). *Basic space plasma physics* (Vol. 15-22). https://doi.org/10.1142/p015

Baxter, A. (2015). *Network rail guide to overhead electrification* (tech. rep. No. 132787-ALB-GUN-EOH-000001). Alan Baxter and Associates LLP. 75 Cowcross Street, London, EC1M 6EL.

Beamish, D. (2013). The bedrock electrical conductivity map of the UK. *Journal of Applied Geophysics*, *96*, 87–97. https://doi.org/10.1016/j.jappgeo.2013.06.001

Beamish, D., & White, J. C. (2012). Mapping and predicting electrical conductivity variations across southern England using airborne electromagnetic data. *Quarterly Journal of Engineering Geology and Hydrogeology*, *45*(1), 99–110. https://doi.org/10.1144/1470-9236/11-026

Beggan, C. D. (2015). Sensitivity of geomagnetically induced currents to varying auroral electrojet and conductivity models. *Earth, Planets and Space*, *67*. https://doi.org/10.1186/s40623-014-0168-9

Beggan, C. D., Beamish, D., Richards, A., Kelly, G. S., & Alan, A. W. (2013). Prediction of extreme geomagnetically induced currents in the UK high-voltage network. *Space Weather*, *11*, 407–419. https://doi.org/10.1002/swe.20065

Beggan, Ciarán D., Richardson, Gemma S., Baillie, Orsi, Hübert, Juliane, & Thomson, Alan W. P. (2021). Geolectric field measurement, modelling and validation during geomagnetic storms in the UK. *J. Space Weather Space Clim.*, *11*, 37. https://doi.org/10.1051/swsc/2021022

Belcher, J. W., & Davis Jr., L. (1971). Large-amplitude alfvén waves in the interplanetary medium, 2. *Journal of Geophysical Research (1896-1977)*, *76*(16), 3534–3563. https://doi.org/https://doi.org/10.1029/JA076i016p03534

Bolduc, L. (2002). GIC observations and studies in the Hydro-Québec power system [Space Weather Effects on Technological Systems]. *Journal of Atmospheric and Solar-Terrestrial Physics*, *64*(16), 1793–1802. https://doi.org/10.1016/S1364-6826(02)00128-1

Boteler, D. H. (1994). Geomagnetically induced currents: Present knowledge and future research. *IEEE Transactions on Power Delivery (Institute of Electrical and Electronics Engineers); (United States)*, *9*. https://doi.org/10.1109/61.277679

Boteler, D. H. (2013). A new versatile method for modelling geomagnetic induction in pipelines. *Geophysical Journal International*, *193*, 98–109. https://doi.org/10.1093/gji/ggs113

Boteler, D. H. (2019). A 21st century view of the March 1989 magnetic storm. *Space Weather*, *17*(10), 1427–1441. https://doi.org/10.1029/2019SW002278

Boteler, D. H. (2021). Modeling geomagnetic interference on railway signaling track circuits. *Space Weather*, *19*. https://doi.org/10.1029/2020SW002609

Boteler, D. H., & Pirjola, R. J. (2017). Modeling geomagnetically induced currents. *Space Weather*, *15*, 258–276. https://doi.org/10.1002/2016SW001499

Boteler, D. H. (1997). Distributed-source transmission line theory for electromagnetic induction studies. *Proceedings of the 1997 Zurich EMC Symposium*, 401–408.

Boteler, D. H. (2014). Methodology for simulation of geomagnetically induced currents in power systems. *Journal of Space Weather and Space Climate*, *4*. https://doi.org/10.1051/swsc/2014018

Boteler, D. H., & Trichtchenko, L. (2015). Telluric influence on pipelines. In *Oil and gas pipelines* (pp. 275–288). John Wiley; Sons, Ltd. https://doi.org/https://doi.org/10.1002/9781119019213.ch21

British steel: Rail product range (tech. rep.). (2020). British Steel. PO Box 1, Brigg Road, Scunthorpe, North Lincolnshire, DN16 1BP, United Kingdom.

Cabinet Office. (2012). National risk register of civil emergencies.

Cabinet Office. (2023). National risk register of civil emergencies.

Cade III, W. B. (2013). The first recorded space weather impact? *Space Weather*, *11*(9), 489–489. https://doi.org/10.1002/swe.20091

Cagniard, L. (1953). Basic theory of the magneto-telluric method of geophysical prospecting. *GEOPHYSICS*, *18*(3), 605–635. https://doi.org/10.1190/1.1437915

Constable, S. (2015). 5.07 - geomagnetic induction studies. In G. Schubert (Ed.), *Treatise on geophysics (second edition)* (Second Edition, pp. 219–254). Elsevier. https://doi.org/https://doi.org/10.1016/B978-0-444-53802-4.00101-9

Cravens, T. E. (1997). *Physics of solar system plasmas*. Cambridge University Press. https://doi.org/10.1017/CBO9780511529467

Darch, G., McCormack, L., Hayes, D., Tomlinson, J., Hooper, P., Williams, R., Hapgood, M., Bisi, M., Marvin, A., & Tyndall, M. (2014). *Rail resilience to space weather final phase 1 report Department for Transport* (tech. rep.). Atkins Limited. Western House (Block B), Peterborough Business Park, Lynch Wood, Peterborough, PE2 6FZ.

Davis, T. N., & Sugiura, M. (1966). Auroral electrojet activity index ae and its universal time variations. *Journal of Geophysical Research (1896-1977)*, *71*(3), 785–801. https://doi.org/https://doi.org/10.1029/JZ071i003p00785

Department for Transport. (2015). Supplement to the october 2013 strategic case for hs2 technical annex: Demand and capacity pressures on the west coast main line.

Dungey, J. W. (1961). Interplanetary magnetic field and the auroral zones. *Phys. Rev. Lett.*, *6*, 47–48. https://doi.org/10.1103/PhysRevLett.6.47

Eroshenko, E. A., Belov, A. V., Boteler, D., Gaidash, S. P., Lobkov, S. L., Pirjola, R., & Trichtchenko, L. (2010). Effects of strong geomagnetic storms on Northern railways in Russia. *Advances in Space Research*, *46*, 1102–1110. https://doi.org/10.1016/j.asr.2010.05.017

Ganushkina, N. Y., Liemohn, M. W., & Dubyagin, S. (2018). Current systems in the earth's magnetosphere. *Reviews of Geophysics*, *56*(2), 309–332. https://doi.org/https://doi.org/10.1002/2017RG000590

Hale, G. E., & Nicholson, S. B. (1925). The law of sun-spot polarity. *Astrophysical Journal*, *62*, 270. https://doi.org/10.1086/142933

Hapgood, M., Angling, M. J., Attrill, G., Bisi, M., Cannon, P. S., Dyer, C., Eastwood, J. P., Elvidge, S., Gibbs, M., Harrison, R. A., Hord, C., Horne, R. B., Jackson, D. R., Jones, B., Machin, S., Mitchell, C. N., Preston, J., Rees, J., Rogers, N. C., ... Willis, M. (2021). Development of space weather reasonable worst-case scenarios for the uk national risk assessment. *Space Weather*, *19*. https://doi.org/10.1029/2020SW002593

Heaviside, O. (1892). Electrical papers (2 volumes, collected works). *The Electrician Printing and Publishing Co.*

Heaviside, O. (1876). Xix. on the extra current. *Philosophical Magazine Series 1*, *2*, 135–145.

Iwasaki, M., Furukawa, K., Okamoto, K., Koreishi, K., Kaneyasu, T., Kota, Y., Kawase, K., & Radford, A. (2017). Development of class 385 semi-customised/standard commuter rolling stock for global markets. *Hitachi Review*, *66*.

Kappenman, J., Albertson, V., Damsk, B., & Dale, S. (1990). Solar wind monitor satellite. *IEEE Power Engineering Review*, *10*(5), 4–8. https://doi.org/10.1109/39.54415

Kasinskii, V. V., Ptitsyna, N. G., Lyahov, N. N., Tyasto, M. I., Villoresi, G., & Iucci, N. (2007). Effect of geomagnetic disturbances on the operation of railroad automated mechanisms and telemechanics. *Geomagnetism and Aeronomy*, *47*, 676–680. https://doi.org/10.1134/S0016793207050179

Kataoka, R., & Ngwira, C. (2016). Extreme geomagnetically induced currents. *Progress in Earth and Planetary Science*, *3*(1), Article 23, 23. https://doi.org/10.1186/s40645-016-0101-x

Keenor, G. (2021). *Overhead line electrification for railways - 6th-edition*. Keenor. https://ocs4rail.com/downloads/

Kelly, G. S., Viljanen, A., Beggan, C. D., & Thomson, A. W. P. (2017). Understanding GIC in the UK and French high-voltage transmission systems during severe magnetic storms. *Space Weather*, *15*(1), 99–114. https://doi.org/10.1002/2016SW001469

Kivelson, M. G., & Russell, C. T. (1995). *Introduction to space physics*. Cambridge University Press.

Knight-Percival, A., Johnson, C., Richards, B., Palmer, S., & Bowring, N. (2020). Mapping of the electromagnetic environment on the railway: Condition monitoring of signalling assets. *Proceedings of the Institution of Mechanical Engineers, Part F: Journal of Rail and Rapid Transit*, *234*, 246–256. https://doi.org/10.1177/0954409718802998

Krausmann, E., Andersson, E., Russell, T., & Murtagh, W. (2015). *Space weather and rail: Findings and outlook* (tech. rep.). European Commission. Joint Research Centre, Via E. Fermi 2749, 21027 Ispra (VA), Italy. https://doi.org/10.2788/211456

Le, G., Russell, C. T., & Takahashi, K. (2004). Morphology of the ring current derived from magnetic field observations. *Annales Geophysicae*, *22*(4), 1267–1295. https://doi.org/10.5194/angeo-22-1267-2004

Le, G., Slavin, J. A., & Strangeway, R. J. (2010). Space technology 5 observations of the imbalance of regions 1 and 2 field-aligned currents and its implication to the cross-polar cap Pederson currents. *Journal of Geophysical Research: Space Physics*, *115*(A7). https://doi.org/https://doi.org/10.1029/2009JA014979

Lejdström, B., & Svensson, S. (2020). Calculation of geomagnetic interference voltages in track circuits, original publication (in Swedish) appendix 6, betänkande: Angående det tekniska utförandet av signalanläggningar vid statens järnvägar, 1956. Translation (in English). *Infrastructure Resilience Risk Reporter*, *1*, 28–51. https://carleton.ca/irrg/journal/

Lewis, Z. M., Wild, J. A., Allcock, M., & Walach, M. T. (2022). Assessing the impact of weak and moderate geomagnetic storms on UK power station transformers. *Space Weather*, *20*. https://doi.org/10.1029/2021SW003021

Liu, L., Ge, X., Zong, W., Zhou, Y., & Liu, M. (2016). Analysis of the monitoring data of geomagnetic storm interference in the electrification system of a high-speed railway. *Space Weather*, *14*, 754–763. https://doi.org/10.1002/2016SW001411

MacDermot, E. T., & Clinker, C. R. (1972). *History of the great western railway volume one 1833-1863*. Ian Allan Publishing.

Mariscotti, A. (2020). Impact of rail impedance intrinsic variability on railway system operation, emc and safety. *International Journal of Electrical and Computer Engineering*, *9*. https://doi.org/10.11591/ijece.v9i4.ppxx-xx

Maunder, E. W. (1897a). Greenwich observatory: Longitude nought. *The Leisure Hour*, *1897/8*(3), 228–238.

Maunder, E. W. (1897b). Greenwich observatory: Storm and sun. *The Leisure Hour*, *1897/8*(3), 293–297, 375–379.

Mayaud, P. N. (1980). The au, al and ae indices. In *Derivation, meaning, and use of geomagnetic indices* (pp. 96–115). American Geophysical Union (AGU). https://doi.org/https://doi.org/10.1002/9781118663837.ch7

Mckay, A. J. (2003). Geoelectric fields and geomagnetically induced currents in the United Kingdom. http://hdl.handle.net/1842/639

McLay, S. A., & Beggan, C. D. (2010). Interpolation of externally-caused magnetic fields over large sparse arrays using Spherical Elementary Current Systems. *Annales Geophysicae*, *28*(9), 1795–1805. https://doi.org/10.5194/angeo-28-1795-2010

Milan, S. E., Lester, M., Cowley, S. W. H., Oksavik, K., Brittnacher, M., Greenwald, R. A., Sofko, G., & Villain, J.-P. (2003). Variations in the polar cap area during two substorm cycles. *Annales Geophysicae*, *21*(5), 1121–1140. https://doi.org/10.5194/angeo-21-1121-2003

Moldwin, M. (2022). *An introduction to space weather* (2nd ed.). Cambridge University Press.

Nature. (1871). Observations upon magnetic storms at higher latitudes. *Nature*, *4*(101), 441–442.

NR/BR/867. (1990). *Specification for ac immune dc track feed units* (tech. rep.). Network Rail. 40 Melton Street, London, NW1 2EE.

NR/BR/939A. (1971). *Specification for miniature tractive armature ac immune dc neutral track relay, plug-in type for railway signalling purposes* (tech. rep.). Network Rail. 40 Melton Street, London, NW1 2EE.

NR/GN/ELP/27312. (2006). *Impedances of 25 kv a.c. overhead lines for classic system* (tech. rep.). Network Rail. 40 Melton Street, London, NW1 2EE.

NR/PS/SIG/11755. (2000). *Dc track circuits (formerly rt/e/ps/11755)* (tech. rep.). Network Rail. 40 Melton Street, London, NW1 2EE.

NR/SP/ELP/21085. (2007). *Specification for the design of earthing and bonding systems for the 25 kv a.c. electrified lines* (tech. rep.). Network Rail. 40 Melton Street, London, NW1 2EE.

NR/SP/SIG/50004. (2006). *Methodology for the demonstration of electrical compatibility with dc (ac immune) track circuits* (tech. rep.). Network Rail. 40 Melton Street, London, NW1 2EE.

Oyedokun, D., Heyns, M., Cilliers, P., & Gaunt, C. (2020). Frequency components of geomagnetically induced currents for power system modelling. *2020 International SAUPEC/RobMech/PRASA Conference*, 1–6. https://doi.org/10.1109/SAUPEC/RobMech/PRASA48453.2020.9041021

Parker, E. (1958). Dynamics of the interplanetary gas and magnetic fields. *Astrophysical Journal*, *128*, 664. https://doi.org/10.1086/146579

Patterson, C. J., Wild, J. A., Beggan, C. D., Richardson, G. S., & Boteler, D. H. (2024). Modelling electrified railway signalling misoperations during extreme space weather events in the UK. *Scientific Reports*, *14*(1583). https://doi.org/10.1038/s41598-024-51390-3

Patterson, C. J., Wild, J. A., & Boteler, D. H. (2023a). Modeling the impact of geomagnetically induced currents on electrified railway signaling systems in the United Kingdom. *Space Weather*, *21*(3), e2022SW003385. https://doi.org/10.1029/2022SW003385

Patterson, C. J., Wild, J. A., & Boteler, D. H. (2023b). Modeling "wrong side" failures caused by geomagnetically induced currents in electrified railway signaling systems in the UK. *Space Weather*, *21*(12), e2023SW003625. https://doi.org/10.1029/2023SW003625

Pirjola, R. (1985). On currents induced in power transmission systems during geomagnetic variations. *IEEE Transactions on Power Apparatus and Systems*, *PAS-104*, 2825–2831. https://doi.org/10.1109/TPAS.1985.319126

Ptitsyna, N. G., Kasinskii, V. V., Villoresi, G., Lyahov, N. N., Dorman, L. I., & Iucci, N. (2008). Geomagnetic effects on mid-latitude railways: A statistical study of anomalies in the operation of signaling and train control equipment on the East-Siberian Railway. *Advances in Space Research*, *42*, 1510–1514. https://doi.org/10.1016/j.asr.2007.10.015

Pulkkinen, A., Viljanen, A., Pajunpää, K., & Pirjola, R. (2002). Recordings and occurrence of geomagnetically induced currents in the Finnish natural gas pipeline network. *Applied Geophysics*, *48*.

Pulkkinen, A., Lindahl, S., Viljanen, A., & Pirjola, R. (2005). Geomagnetic storm of 29–31 October 2003: Geomagnetically induced currents and their relation to problems in the Swedish high-voltage power transmission system. *Space Weather*, *3*(8). https://doi.org/10.1029/2004SW000123

Pulkkinen, A., Viljanen, A., & Pirjola, R. (2006). Estimation of geomagnetically induced current levels from different input data. *Space Weather*, *4*(8). https://doi.org/https://doi.org/10.1029/2006SW000229

Rogers, N. C., Wild, J. A., Eastoe, E. F., Gjerloev, J. W., & Thomson, A. W. (2020). A global climatological model of extreme geomagnetic field fluctuations.

Journal of Space Weather and Space Climate, *10*. https://doi.org/10.1051/swsc/2020008

Russell, C. T., Luhmann, J. G., & Strangeway, R. J. (2016). *Space physics: An introduction*. Cambridge University Press.

Schelkunoff, S. A. (1938). The impedance concept and its application to problems of reflection, refraction, shielding and power absorption. *Bell System Technical Journal*, *17*(1), 17–48. https://doi.org/https://doi.org/10.1002/j.1538-7305.1938.tb00774.x

Sugiura, M. (1964). Hourly values of equatorial dst for the igy. *Ann. Int. Geophys. Yr.*, *35*. https://www.osti.gov/biblio/4554034

The system of electrification for british railways (tech. rep.). (1955). Britsh Transport Commission. 222 Marylebone Road, London, NW1.

Thelander, T., Alm, E., Edenius, R., Ekberg, F., Helmer, O., Karsberg, A., T., L. L., & Ulf, B. (1956). *Det tekniska utförandet av signalanläggningar vid statens järnvägar, del i: Spårledningsteknik, avgivet den 20 augusti 1956* (tech. rep.). Statens Järnvägars Publikationer. Stockholm.

Thomson, A. W. P., Dawson, E. B., & Reay, S. J. (2011). Quantifying extreme behavior in geomagnetic activity. *Space Weather*, *9*(10). https://doi.org/10.1029/2011SW000696

Trichtchenko, L. (2021). Frequency considerations in gic applications. *Space Weather*, *19*(8), e2020SW002694. https://doi.org/https://doi.org/10.1029/2020SW002694

Viljanen, Ari, Myllys, Minna, & Nevanlinna, Heikki. (2014). Russian geomagnetic recordings in 1850–1862 compared to modern observations. *J. Space Weather Space Clim.*, *4*, A11. https://doi.org/10.1051/swsc/2014008

Weaver, J. T. (1994). *Mathematical methods for geo-electromagnetic induction*. John Wiley; Sons Inc.

Weaver, J. (1973). Induction in a layered plane earth by uniform and non-uniform source fields. *Physics of the Earth and Planetary Interiors*, *7*(3), 266–281. https://doi.org/https://doi.org/10.1016/0031-9201(73)90053-8

Wik, M., Pirjola, R., Lundstedt, H., Viljanen, A., Wintoft, P., & Pulkkinen, A. (2009). Space weather events in July 1982 and October 2003 and the effects of geomagnetically induced currents on Swedish technical systems. *Annales Geophysicae*, *27*, 1775–1787.